Loughborough University

Loughborough University
Institutional Repository

Mathematical modeling of soil erosion by rainfall and shallow overland flow

This item was submitted to Loughborough University's Institutional Repository by the/an author.

Additional Information:

- A Doctoral Thesis. Submitted in partial fulfillment of the requirements for the award of Doctor of Philosophy of Loughborough University.

Metadata Record: https://dspace.lboro.ac.uk/2134/9144

Publisher: © Tingting Zheng

Please cite the published version.

Loughborough University

This item was submitted to Loughborough's Institutional Repository (https://dspace.lboro.ac.uk/) by the author and is made available under the following Creative Commons Licence conditions.

creative commons

COMMONS DEED

Attribution-NonCommercial-NoDerivs 2.5

You are free:

- to copy, distribute, display, and perform the work

Under the following conditions:

Attribution. You must attribute the work in the manner specified by the author or licensor.

Noncommercial. You may not use this work for commercial purposes.

No Derivative Works. You may not alter, transform, or build upon this work.

- For any reuse or distribution, you must make clear to others the license terms of this work.
- Any of these conditions can be waived if you get permission from the copyright holder.

Your fair use and other rights are in no way affected by the above.

This is a human-readable summary of the Legal Code (the full license).

Disclaimer

For the full text of this licence, please go to:
http://creativecommons.org/licenses/by-nc-nd/2.5/

Mathematical Modeling of Soil Erosion by Rainfall and Shallow Overland Flow

Tingting Zheng

Department of Civil and Building Engineering

Loughborough University

A Doctoral Thesis Submitted for the Degree of

Doctor of Philosophy

August 2011

© by Tingting Zheng (2011)

Acknowledgements

I would like to extend my heartfelt thanks to a host of people, without whose assistance the accomplishment of this thesis would have been impossible.

First of all, I would like to express my deepest gratitude to my supervisor, Prof. Graham Sander, for his patient guidance, generous assistance, invaluable advice and continual encouragement during my PhD study. His profound knowledge and strict attitude on research gave me great impression as well as great help. He has walked me through all the stages of the writing of this thesis. Without his instructive suggestions and necessary corrections, this thesis could not have reached its present form.

I would also like to thank my director of research, Dr Cecil Scott for ensuring this research went smooth and providing me an opportunity to be a lab demonstrator to undergraduate students.

My thanks would also go to my department for offering me full scholarship during this study. It is a fundamental and essential support of this research.

Besides, I feel grateful to Dr Peter Heng who was the research associate of my supervisor. He spent a few hours of his time to discuss questions with me, which helped solve out many problems.

An honorable mention goes to my family for their constant supports. My mum is always the strongest support during my study since ever. My father, parents-in-law and sister-in-law gave their great help to take care of my baby when he was very young and away from me. Their helps let me concentrate on this research and finally accomplish it. My deep thanks also give to my husband for his forever understanding and support. His generousness and consideration relieved me a lot from my anxiety and made me finally finish the thesis.

Finally, I would like to thank all my friends in Loughborough. I cherish the friendships with them.

Abstract

Key words: soil erosion, sediment transport, one-dimensional, Hairsine-Rose model, time-dependent, method of characteristics, method of lines, bedload transport, hysteresis in SSC

New analytical and numerical solutions are developed to both the kinematic approximation to the St Venant equations and the Hairsine-Rose (HR) soil erosion model in order to gain a better physical understanding of soil erosion and sediment transport in shallow overland flow. The HR model is unique amongst physically based erosion models in that it is the only one that: considers the entire distribution of the soil's sediment size classes, considers the development of a layer of deposited non-cohesive sediment having different characteristics to the original underlying cohesive soil and considers separately the erosion processes of rainfall detachment, runoff entrainment and gravitational deposition.

The method of characteristics and the method of lines were used to develop both the analytical and numerical solutions respectively. These solutions were obtained for boundary and initial conditions typical of those used in laboratory flume experiments along with physically realistic constant and time dependent excess rainfall rates. Depending on the boundary and initial conditions, interesting new solutions of the kinematic wave equation containing expansion waves, travelling shocks as well as solutions which split into an upslope and downslope drying profiles were found.

Numerical solutions of the HR model were applied to the experimental flume data of Polyakov and Nearing (2003) obtained under flow conditions which periodically cycled between net erosion and net deposition conditions. While excellent agreement was found with suspended sediment data, the analysis suggested that an additional transport mechanisms, traditionally not included in soil erosion models, was occurring. While the inclusion of bed-load transport improved the

overall model prediction, it was still not sufficient. Subsequent asymptotic analysis then showed that the interaction of the flow with an evolving bed morphology was in fact far more important than bed load transport. A very interesting finding from this work showed that the traditional criterion of validating sediment transport model based solely on suspended sediment data was not sufficient as reliable predictions could be obtained even when important transport mechanisms were neglected.

Experimental plots of sediment discharge or suspended sediment concentration against water discharge in overland flow have been shown to contain significant hysteresis between the falling and rising limbs of the discharge hydrograph. In the final Chapter, the numerical solution developed for the complete system of soil erosion and kinematic flow was used to show that it was possible for the HR model to simulate three of the four hysteresis loops identified in the literature. Counter clock-wise loops, clock-wise loops and figure 8 loops could all be produced as a result of starting with different initial conditions, being $m_i(x,0) = 0$, $m_i(x,0) = p_i m_t$ and $mi(x,0) = 0.5 p_i m_t$ respectively. This is the first time that these types of hysteresis loops have been produced by any erosion model. The generation of these hysteresis loops are physically explainable in terms of sediment availability and is consistent with data obtained on the field scale.

Contents

List of Figures

List of Tables

Nomenclature

Greek Symbols

α_i	Ratio of the concentration adjacent to the bed to the mean concentration over the entire depth
α_z	Flow detachment efficiency coefficient
β	Bed-load factor
δ	Raindrop induced turbulence coefficient
ϵ	$= 1 + (\alpha v)/R$
ϵ_0	Dimensionless coefficient depending on the soil and fluid properties
η	Efficiency of entrainment
γ	$= \frac{F}{gh}\frac{\rho_s}{\rho_s - \rho}(\Omega - \Omega_{cr})$
γ^*	An arbitrary constant
γ_0	$= \frac{\alpha F \rho_s \rho S_0 K^{\frac{1}{m}}}{\rho_s - \rho}$
γ_i	$= 1 + v_i/R_1$
κ	Experimentally derived particle size coefficient
κ_0	Von Kármán's constant

λ_1 An arbitrary constant

Ω Stream power – the rate of working of the mutual shear stress between the soil surface and overland flow ($W \;\; m^{-2}$)

ω Unit stream power ($= 10uS_0$)

Ω_{cr} Threshold stream power – minimum stream power required to entrain soil ($W \;\; m^{-2}$)

$\overline{\Omega}$ Modified stream power ($g^{1.5} \;\; cm^{-2/3} \;\; s^{-4.5}$)

$\overline{\Omega}_{cr}$ Critical value of $\overline{\Omega}_{cr}$ ($W \;\; m^{-2}$)

ω_{cr} Critical unit stream power ($= 0.4m \;\; s^{-1}$)

ϕ The bed porosity

ρ Water density ($kg \;\; m^{-3}$)

ρ_s Sediment density ($kg \;\; m^{-3}$)

τ An arbitrary constant

τ_b Bed shear stress (Pa)

τ_{ci} Critical shear stress for each size class (Pa)

τ_c Critical shear stress (Pa)

τ_e Average shear stress ($N \;\; m^{-2}$)

τ_f Flow shear stress acting on the soil (Pa)

τ_{ij} viscous stress component acts in the j-direction on a surface normal to the i-direction

τ_{ri} Bed shear stress for each size class (Pa)

ϱ Soil texture exponent, varying between 0.9 and 3.1

Other Symbols

$1D$ One dimensional

$2D$ Two dimensional

$3D$ Three dimensional

A Average annual soil loss term

a Rainfall detachability of original soil ($kg\ \ m^{-3}$)

a_0 Maximum rainfall detachability of original soil at breakpoint depth ($kg\ m^{-3}$)

a_d Rainfall detachability of soil in deposited layer ($kg\ \ m^{-3}$)

a_{d0} Maximum rainfall detachability of deposited soil at breakpoint depth ($kg\ m^{-3}$)

AG Soil aggregate stability (median number of drops)

A_I Area increment

B Transport capacity coefficient ($kg\ \ s\ \ m^{2.5}$)

b An arbitrary constant

B_0 $= (\frac{\rho_s}{\rho_s - \rho})\frac{\eta}{0.6g}$

b_1 An exponent in the range of 1.0 to 2.0

$\overline{c}$ The local mean sediment concentration ($kg\ \ m^{-3}$)

C $= c + \frac{q_b}{q}$

c Total concentration of suspended sediment $c = \sum_{i=1}^{I} c_i$ ($kg\ \ m^{-3}$)

CC Volumetric sediment concentration ($m^3\ \ m^{-3}$)

C_{cr} Cropping and management factor

C_d Fraction of the soil surface exposed to rainfall

C_e Effect of canopy on interrill erosion

c_f A constant in rainfall erosion rate

c_g Transfer rate coefficient

c_h Camping coefficient for splash erosion

CH Cohesion of the soil at saturation (KPa)

c_i Concentration of suspended sediment in size class i ($kg\ \ m^{-3}$)

c_{i0} Boundary value of c_i, i.e. c_i at $x = 0$ ($kg\ \ m^{-3}$)

c_i^j Expansion coefficients for c_i

CP Plant cover factor

C_r Fraction of the soil surface exposed to overland flow

C_s Current local sediment concentration

d Rate of sediment deposition ($kg\ \ m^{-2}\ \ s^{-1}$)

d_{50} Median particle size of the soil (μm)

D_F Soil erosion by runoff ($kg\ \ m^{-2}\ \ s^{-1}$)

D_i Rate of erosion between rills ($kg\ \ m^{-2}\ \ s^{-1}$)

d_i Rate of sediment deposition for size class i ($kg\ \ m^{-2}\ \ s^{-1}$)

D_R Soil erosion by rainfall ($kg\ \ m^{-2}\ \ s^{-1}$)

D_r Rate of erosion within a rill ($kg\ \ m^{-2}\ \ s^{-1}$)

e_i Rate of rainfall detachment of original soil ($kg\ \ m^{-2}\ \ s^{-1}$)

e_b Efficiency of flow transporting the bed-load

e_{di} Rate of rainfall re-detachment of deposited sediment ($kg\ \ m^{-2}\ \ s^{-1}$)

EUROSEM European Soil Erosion model

F Fraction of excess stream power effective for entrainment and re-entrainment (0.1-0.2 Proffitt *et al.* (1993))

f Darcy-Weisbach friction factor

F_1 A function of ϕ

F_r Frounde number ($= u/\sqrt{gh}$)

G Soil infiltration rate ($kg\ \ m^{-2}\ \ s^{-1}$)

g Gravitational acceleration $g = 9.8$ ($m\ \ s^{-2}$)

G_e Effect of ground cover on interrill erosion

GIS Geographical Information System

G_v Soil infiltration rate component in vertical direction ($kg\ \ m^{-2}\ \ s^{-1}$)

H Shielding fraction of original soil due to deposited layer

h Depth of water flow (m)

h Depth of water flow (m)

h_0 Critical flow depth (m)

h_b An arbitrary constant

h_c A constant varying between h_i and h_s

h_i Initial water depth $h(x, 0)$ (m)

h_L Normal flow depth at $x = L \quad (m)$

h_n $h_n = -\int_0^t R dt$ for $t_2 \leq t < t_d$

HR Abbreviation of Hairsine-Rose model

HR Hairsine-Rose model

h_s Boundary condition for the water depth $h(0,t)$ (m)

I Total number of sediment size classes

I_e Effective rainfall intensity

I_R Interception (mm)

J Specific energy per unit mass of soil required to entrain it $(J \;\; kg^{-1})$

j Arbitrary integer

K Phenomenological constant which is related to the slope and roughness of the plane

k Kinematic wave number

KE Total kinetic energy of the soil $(J \;\; m^{-2})$

$k(h)$ A reduction factor representing the reduction in rainfall erosion caused by increasing depth of water

K_I Soil detachability factor by rainfall $(kg \;\; s \;\; m^{-4})$

K_i Interrill erodibility parameter

KINEROS Kinematic Erosion Simulation model

K_R Soil detachability factor by runoff $(kg \;\; m \;\; N^{-1.5} s^{-1})$

K_r Soil erodibility factor$(tons/acre)$

K_{rr} Rill soil erodibility parameter ($s \;\; m^{-1}$)

$Ksat$ Saturated hydraulic conductivity ($mm\, hr^{-1}$)

k_t Transport coefficient

K_x x component of K

K_y y component of K

L Length of flow domain (m)

l A non-dimensional exponent in the range 1.3 to 2

LISEM Limburg Soil Erosion model

LS Topographical factor

m Manning $m = \frac{5}{3}$, Dary-Weisbach $m = \frac{2}{3}$

M_x Effect of rainfall and infiltration in x direction

M_y Effect of rainfall and infiltration in y direction

m_i Mass of sediment in size class i in deposited layer ($kg \;\; m^{-2}$)

m_{i0} Initial value for m_i ($kg \;\; m^{-2}$)

m_i^j Expansion coefficients for m_i

MOC The method of characteristics

MOL The method of lines

m_t Total mass of deposited sediment $m_t = \sum_{i=1}^{I}$ ($kg \;\; m^{-2}$)

m_t^j Expansion coefficients for m_t

m_{tp}^* Mass of deposited sediment required to cover original soil at ponding time ($kg \;\; m^{-2}$)

m_t^* Mass of deposited sediment required to stop erosion of original soil ($kg\ \ m^{-2}$)

n Manning's friction coefficient

ODE Ordinary Differential Equations

P Rainfall rate ($m\ \ s^{-1}$)

p_i Proportion of sediment in size class i of the original soil, $0 < p_i < 1$ and $\sum_{i=1}^{I} p_i = 1$

PP Support practice fact

p_w water pressure ($N\ \ m^{-2}$)

Q Volumetric water flux per unit width ($m^3\ \ s^{-1}$)

q Water flux per unit width ($m^2\ \ s^{-1}$)

q_0 Water flux per unit width at $x = 0$ ($m^2\ \ s^{-1}$)

q_b $= \sum q_{bi}$

q_{bi} $= \beta h r_{ri}$

q_s $= qc$

q_x x component of water flux q

q_y y component of water flux q

R Excess rainfall rate $= P - G$ ($m\ \ s^{-1}$)

r Parameter related to the degree of convergence

R_0 An arbitrary constant

R_1 Runoff rate per unit of plane area ($m\ \ s^{-1}$)

r_i Rate of entrainment of original soil ($kg\ \ m^{-2}\ \ s^{-1}$)

RR Rainfall erosivity factor (cm/hr)

$\widehat{r}_{ri}$ $= (1-\beta)r_{ri}$

r_{ri} Rate of re-entrainment of deposited sediment $(kg\ \ m^{-2}\ \ s^{-1})$

R_s Spacing of rills

S An arbitrary constant

S_0 Slope of the plane

S_f Bed friction

S_{fx} Bed friction component in x direction

S_{fy} Bed friction component in y direction

S_{ox} Bed slope component in x direction

S_{oy} Bed slope component in y direction

SSC Suspended Sediment Concentration $(kg\ \ m^{-3})$

Δt Time increment (s)

$\tan(\mu)$ Dynamic coefficient of internal friction

t Time (s)

t_0 An arbitrary constant

t_2 $\int_{t^*}^{t_2} = -h_s$

t_3 $\int_{t_3}^{t} = -h_s$ and $t^* < t_3 < t$

t_4 $\int_{t_4}^{t} Rdt' = -h_s$ and $0 < t_4 < t^*$

T_c Transport capacity $(kg\ \ m^{-1}\ \ s^{-1})$

TC Volumetric transport capacity ($m^3 \ m^{-3}$)

t_d $\int_0^{t_d} R dt' = -h_b$

t_{di} $\int_0^{t_{di}} R dt' = -h_i$

t_{ds} $\int_0^{t_{ds}} R dt' = -h_s$

t_L Upper limit of t (s)

t_p The commence of runoff (s)

t_R The duration of the runoff event (s)

t^* The time when the rainfall rate equals to the infiltration rate ($R = 0$) (s)

μ Viscosity

u Flow velocity in x direction ($m \ s^{-1}$)

U^* Shear velocity ($m \ s^{-1}$)

U_c^* $= \sqrt{y_c(\rho_s - 1)gd_{50}}$

USLE Universal Soil Loss Equation model

v Flow velocity in y direction ($m \ s^{-1}$)

v_i Settling velocity of sediment in size class i ($m \ s^{-1}$), it varies from 10^{-5} to 0.1

v_s Settling velocity of the sediment for single size class ($m \ s^{-1}$)

W Flow width (m)

w Flow velocity in z direction ($m \ s^{-1}$)

WEPP Water Erosion Prediction Project model

Δx Size of an element (m)

x Distance in downslope direction (m)

x^* $= mK \int_{t^*}^{t} h^{m-1} dt'$

x_* $= \Omega_{cr}/(\rho g S R_1)$

x_2 $= mK \int_{t^*}^{t_2} h^{m-1} dt'$

x_4 $= mK \int_{t_4}^{t} h^{m-1} dt'$

x_0 An arbitrary constant

x_a, x_b, x_c Charateristic curves emanating from original

x_f $= \frac{K h_b^m}{K sat}$

x_L Upper limit of x (m)

x_s Kinematic wave shock position

y_c Modified Shields' critical shear velocity based on particle Reynolds number $(m \;\; s^{-1})$

CHAPTER 1

Introduction

Soil Erosion is a phrase to describe the natural geologic phenomenon of the displacement of soil from the place of its formation by causative agents like raindrops, runoff, wind, gravity, chemical reactions and anthropogenic perturbation such as tillage (Govers *et al.*, 1999) and its deposition at a depressional and/or protected site (Lal, 2001, 2003). However, in the modern usage it has nearly equivalent meaning with **soil loss** or **soil degradation**, as accelerated soil erosion is the predominant reason causing soil loss and it can be a manifestation of soil degradation (Lal, 2001). There is about 2 billion hectares, about 13.42 per cent of total land on the earth affected by human-induced soil degradation. Amongst this, the land area affected by land degradation due to soil or water erosion amounts to 82.5 per cent (GLASOD, 1990; Oldeman *et al.*, 1991).

Erosion processes effect the physical, chemical and biological properties of the soil. Physically, erosion removes soil. In general, if the erosion rate is roughly the same as the rate that soil is formed then the total mass of soil keeps a dynamic balance, otherwise there is a soil loss or gain occurring. Unfortunately, recent research has revealed that the observed erosion rates exceed the natural soil generation rate in developed countries like the UK, USA and Australia (Brazier, 2004) and developing countries like China and India (Barton *et al.*, 2004; Jin-Jun *et al.*, 2007).The desertification processes in the world's dry rangelands

is considered to be mainly caused by the loss of soil stability and the subsequent soil erosion (Pierson, 2000). Nearly one-third of the world's arable land has been lost by erosion and continues to be lost at a rate of more than 10 million hectares per year. With the increase of 250 thousand people each day, the ability to provide food to meet the demands of the world population will become increasingly strained. (Pimentel *et al.*, 1995).

Soil Erosion is a size selective process. The finer soil particles are preferentially removed or transported by runoff and leave coarser particles on the eroded area (Asadi *et al.*, 2007; Foster *et al.*, 1985). As chemical fertilizers like Nitrogen and Phosphorus tend to sorb to finer particles of soil, these nutrients are easily carried away by eroded sediments and runoff. The over-accumulated nutrients can result in degrading the quality of surface water bodies through eutrophication and the eventual contamination of groundwater through infiltration (Kee Kwong *et al.*, 2002). This non-point/diffuse source pollution is much more difficult to control than point source pollution. It has also been shown that CO_2 and other greenhouse gases emissions from terrestrial ecosystem are exacerbated by soil degradation, of which accelerated soil erosion is the most predominant and widespread form (Lal, 2003).

Many key factors related to the development of soil functionality are underpinned by soil biological processes and the rearrangement of soil particles into stable aggregates (Moreno-de las Heras, 2009). However, accelerated soil erosion can prevent the accumulation of soil organic matter and thus limit the growth of vegetation which then causes the development and spatial organization of both soil physical structure and soil biological functionality to be drastically constrained.

Soil erosion and its subsequent problems have greatly effected the environmental and economic base that human beings rely on for survival. It is extremely important to adopt means to better understand and analyze soil erosion processes to reduce the impact of soil erosion and to minimize anthropogenic perturbations. Mathematical modeling of soil erosion and sediment transport has been found to be an effective and cost-saving way to predict the consequences of both natural

and human-induced environmental changes and impacts on the sediment dynamics.

This thesis is concentrated on the study of surface soil erosion modeling which can be divided into two parts: water flow dynamics and erosion dynamics. Water flow is the transport agent of soil sediments. By solving the flow dynamics we obtain the flow depth and velocity fields across the land surface and the flow discharge from the land surface. The computed flow depth and velocity fields are, in turn, used for the erosion dynamics to predict the sediment concentration field across the land surface and the sediment discharge from the land surface. The linkage between hydrological processes and sediment transport forms the basis of all erosion models, for example USLE, RUSLE, ANSWERS, LISEM, WEPP, EUROSEM, KINEROS, WEPP and Hairsine-Rose (HR). Some of these are empirically based models like USLE and RUSLE, while the others are based on detailed mathematical descriptions of physical process like ANSWERS, WEPP, EUROSEM, Hairsine-Rose etc (Krysanova *et al.*, 1998). Because of the advantages of the HR model (as can be read in Section 2.2), it will be adopted in this research.

1.1 Aims

The aims of this thesis are to find effective, accurate and robust methods to analyze and compute solutions of the shallow water and soil erosion equations, and develop a better physical understanding of sediment transport in shallow overland flows. These aims are accomplished by working through the following four research objectives.

1. Carry out a literature review of the physical and mathematical background knowledge about shallow water flow and soil erosion modeling;

2. Develop analytical and numerical solutions for the water and sediment transport equations;

3. Programme both the analytical and numerical solutions by using MATLAB to achieve the visualization of solutions;

4. Compare against experimental results in literature for model validation and refinement;

1.2 Contribution of this Research to Knowledge

The contributions of my PhD research to existing knowledge are (i) the development of new analytical solutions for kinematic wave equation, (ii) the development of numerical solutions using method of lines to give fully time and space dependent solutions to both the water and sediment flow field; (iii) extension of the HR model to include a bedload transport term; (iv) Application of the extended model to independent experimental data for net erosion and net depositional flows. Lastly this study also reveals that the standard test for a erosion model equation is not sufficient. It is shown that accurate estimates of space dependent suspended sediment concentrations can be obtained by a model that can lack key physical attributes. Consequently much more stringent and extensive test are required, such as determining the evolution of the soil surface, if a reliable verification of an erosion model is to be made.

1.3 Thesis Structure

This thesis has six chapters, three appendices and a CD, with the content of each being as follow:

- *Chapter 1* is introduction. It introduces the influence of soil erosion on society and the importance of soil erosion research. The aims of my PhD study are presented here as well as the main contributions of this study.

- *Chapter 2* contains the literature review and is divided into two parts. The first part of literature review covers the hydrology of shallow overland water flow, and in particular the kinematic flow. The derivation of Saint Venant equations, the kinematic and diffusive wave approximations and analytical solutions to the kinematic wave equation are reviewed. The second part of the literature review focuses on soil erosion. The typical soil erosion mechanisms contained in erosion models and the commonly used soil erosion models are reviewed, especially, the HR model.

- *Chapter 3* presents new analytical solutions to kinematic wave equation for a number of different boundary conditions and for various time dependent excess rainfall rates. The new solutions are shown to be posses both shocks and expansion waves.

- *Chapter 4* develops a numerical solution to the time-dependent HR model for a constant water depth h. Steady state analytical solutions under both net deposition and net erosion conditions are presented, and are used to verify the numerical solution to the HR model. Validation of the time-dependent HR model is obtained through comparison to experimental data presented in Fig. (1) of Polyakov and Nearing (2003). An extended HR model is developed by introducing a bedload term, then steady state analytical solutions are obtained as well as a full numerical solution of the extended model.

- *Chapter 5* considers the case where the water depth h is both space and time dependent. Due to the impact of raindrops on the soil surface prior to rainfall, soil particles are detached resulting in a change of the soils surface structure during this period. At the time of runoff commencement there is also a singularity in the sediment transport equation. Consequently this chapter develops analytical solutions of the evolution of soil surface properties prior to runoff and an analytic expansion of the suspended sediment

concentration at the time of runoff generation, and a numerical solution for later times. Within this chapter it is also shown that the HR model is able to reproduce known hysteretic behavior in sediment discharge versus water discharge graphs. Clockwise, counter-clockwise and figure eight hysteresis curves are reproduced by the HR model along with a clear physical explanation for their existence.

- *Chapter 6* presents the conclusion and suggests research area for the future.
- *Appendix A* includes a published journal paper.
- *Appendix B* includes a conference paper.
- *Appendix C* includes two conference posters.
- The attached CD includes the pdf files of the two posters (for better view) and all the MATLAB codes developed for this thesis.

CHAPTER 2

Literature Review

Soil erosion by water is the result of the combination of rain detaching and overland flow transporting and entraining soil.

Rainsplash Erosion– If rain falls with sufficient intensity and raindrops hit the bare soil (Fig. (2.1)), their kinetic energy is able to detach and move soil particles for a short distance, usually of the order of only a few centimeters distance. While it is mostly a soil redistribution process, soil particles do move slowly downslope.

Runoff Erosion– Rainfall may also move soil indirectly by means of overland water flow, like sheet flow Fig. (2.2) (with the resulting erosion called sheet erosion or interrill erosion) or in confined flows such as rills Fig. (2.3) or gullies Fig. (2.4) (called respectively rill erosion or gully erosion), or the combination of these forms of flow Fig. (2.5). Various forms of erosion and sediment transports are presented in Fig. (2.6). There are two reasons that overland flow occurs. Firstly, if the rainfall intensity is higher than the soil infiltration rate, the excess rainfall results in overland flow and is called `infiltration excess runoff`. Secondly, if the bare soil has already absorbed all the water it can hold or it is frozen, runoff will be produced through a process known as `saturation excess runoff`.

As the main transfer method of eroded soil occurs primarily through the overland flow of water, understanding and predicting soil erosion and transport,

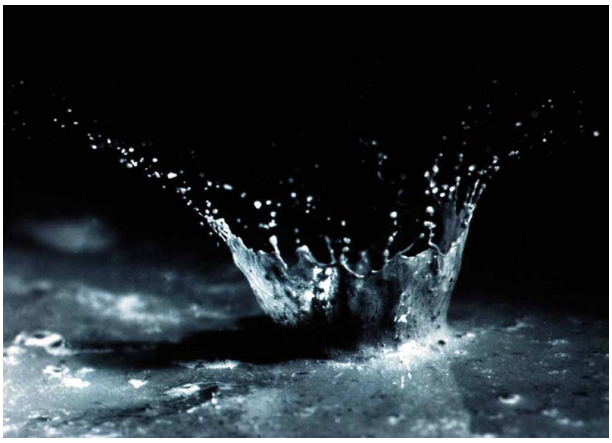

Figure 2.1: Soil detachment by raindrops (from www.uwsp.edu)

Figure 2.2: Soil erosion by sheet flow (from www.soilerosion.net)

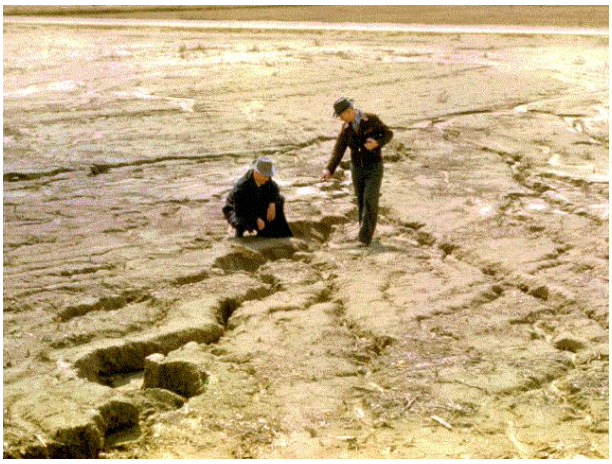

Figure 2.3: Soil erosion by rill flow (from www.google.com.hk)

first requires a solid understanding of the water flow field.

2.1 Shallow Overland Water Flow

Water flow plays an important role in causing soil erosion and the transportation of sediments. The water on the earth can be essentially divided into two main categories: surface water and ground water. This study is focused on soil erosion causing by surface water which includes thin sheet flow over plane, rough or irregular surfaces such as wetlands, and flow in rills, streams, rivers, lakes and oceans (Proffitt *et al.*, 1993). Amongst these, soil erosion by shallow overland water flow is the key role that will be studied here.

The formulation of suitable mathematical models for overland flow is not difficult, however, computationally, such models are very challenging due to the presence of a free surface. The free surface is the water-air boundary, and therefore, boundary conditions need to be satisfied. However the position of this boundary is unknown and so the domain on which the equations are to be solved is also not known a priori. In order to derive computationally more tractable models,

Figure 2.4: Soil erosion by Gully flow (from www.indianetzone.com)

Figure 2.5: Erosion by sheet flow and rills (from http://soer.justice.tas.gov.au)

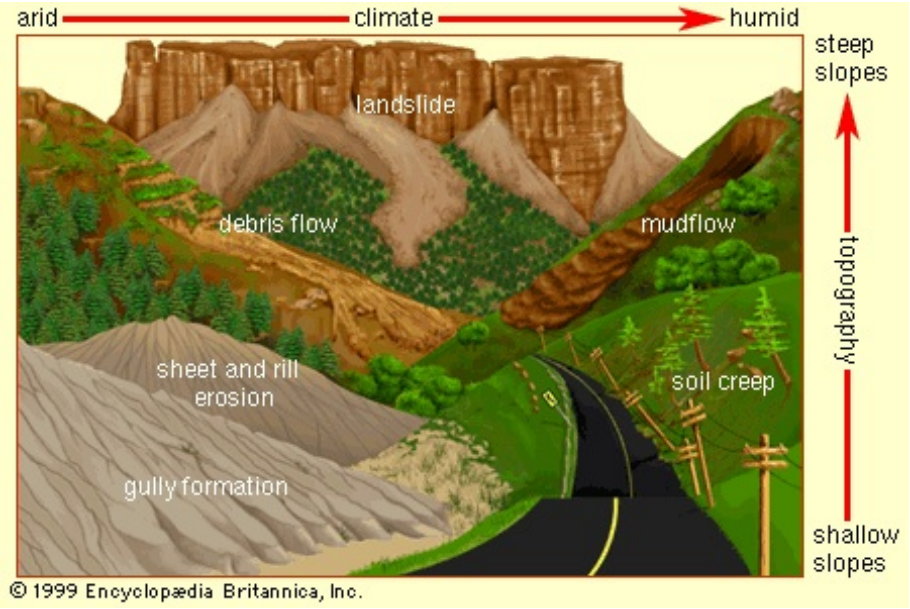

Figure 2.6: Various types of erosion (from www.britannica.com)

one must make some assumptions. One of the most widely used assumptions is that the depth of water is much smaller than its flow length, which gives rise to non-linear shallow water theory (Toro, 2001).

2.1.1 Derivation of St Venant Equations

Under the assumption that the flow depth is very "shallow" compared to the flow length, free-surface overland flow can mathematically be described by the Shallow Water Equations (SWEs) (Toro, 2001). The main variant of the SWEs that we are using in this thesis are the St Venant equations which can be derived from Navier-Stokes Equations.

The unsteady, 3D Navier-Stokes equations for an incompressible, viscous flow are expressed as (Toro, 2001)

$$\frac{\partial U}{\partial x} + \frac{\partial V}{\partial y} + \frac{\partial W}{\partial z} = 0, \tag{2.1}$$

$$\frac{\partial U}{\partial t} + U\frac{\partial U}{\partial x} + V\frac{\partial U}{\partial y} + W\frac{\partial U}{\partial z} = -\frac{1}{\rho}\frac{\partial p_w}{\partial x} + \nabla \cdot (\frac{\mu}{\rho}\nabla U) \tag{2.2a}$$

$$\frac{\partial V}{\partial t} + U\frac{\partial V}{\partial x} + V\frac{\partial V}{\partial y} + W\frac{\partial V}{\partial z} = -\frac{1}{\rho}\frac{\partial p_w}{\partial y} + \nabla \cdot (\frac{\mu}{\rho}\nabla V) \tag{2.2b}$$

$$\frac{\partial W}{\partial t} + U\frac{\partial W}{\partial x} + V\frac{\partial W}{\partial y} + W\frac{\partial W}{\partial z} = -\frac{1}{\rho}\frac{\partial p_w}{\partial z} + \nabla \cdot (\frac{\mu}{\rho}\nabla W) - g, \tag{2.2c}$$

where U, V, W are flow velocity components in x, y, z direction respectively; ρ is flow density; p_w is the water pressure, μ is the viscosity, and g is the acceleration due to gravity. The coordinate axis is designed such that x and z are in the horizontal and vertical directions.

The Reynolds decomposition is given by $\Phi = \phi + \phi'$, where ϕ is the mean value of a flow property Φ and it is defined as

$$\phi = \frac{1}{\Delta t}\int_0^{\Delta t} \Phi dt, \tag{2.3}$$

and ϕ' is the fluctuation component.

Replacing U, V and W by the sum of their mean values (u, v, w) and fluctuating components (u', v', w') and applying (2.3) to (2.1) and (2.2) results in the time-averaged 3D Reynolds equations as

$$\frac{\partial u}{\partial x} + \frac{\partial v}{\partial y} + \frac{\partial w}{\partial z} = 0, \tag{2.4}$$

$$\frac{\partial u}{\partial t} + u\frac{\partial u}{\partial x} + v\frac{\partial u}{\partial y} + w\frac{\partial u}{\partial z} = -\frac{1}{\rho}\frac{\partial p_w}{\partial x} + \nabla \cdot (\frac{\mu}{\rho}\nabla u) - [\frac{\partial \overline{u'^2}}{\partial x} + \frac{\partial \overline{u'v'}}{\partial y} + \frac{\partial \overline{u'w'}}{\partial z}] \tag{2.5a}$$

$$\frac{\partial v}{\partial t} + u\frac{\partial v}{\partial x} + v\frac{\partial v}{\partial y} + w\frac{\partial v}{\partial z} = -\frac{1}{\rho}\frac{\partial p_w}{\partial y} + \nabla \cdot (\frac{\mu}{\rho}\nabla v) - [\frac{\partial \overline{u'v'}}{\partial x} + \frac{\partial \overline{v'^2}}{\partial y} + \frac{\partial \overline{v'w'}}{\partial z}] \tag{2.5b}$$

$$\frac{\partial w}{\partial t} + u\frac{\partial w}{\partial x} + v\frac{\partial w}{\partial y} + w\frac{\partial w}{\partial z} = -\frac{1}{\rho}\frac{\partial p_w}{\partial z} + \nabla \cdot (\frac{\mu}{\rho}\nabla w) - [\frac{\partial \overline{w'u'}}{\partial x} + \frac{\partial \overline{w'v'}}{\partial y} + \frac{\partial \overline{w'^2}}{\partial z}] - g. \tag{2.5c}$$

Here we used an implicit condition which can be obtained from (2.4) which is

$$\begin{aligned} u'\frac{\partial u'}{\partial x} + u'\frac{\partial v'}{\partial y} + u'\frac{\partial w'}{\partial z} &= 0, \\ v'\frac{\partial u'}{\partial x} + v'\frac{\partial v'}{\partial y} + v'\frac{\partial w'}{\partial z} &= 0, \\ w'\frac{\partial u'}{\partial x} + w'\frac{\partial v'}{\partial y} + w'\frac{\partial w'}{\partial z} &= 0. \end{aligned} \tag{2.6}$$

Theoretically, (2.4) can be solved with a given initial condition at $t = 0$ and boundary conditions on the bottom and free surface. But as mentioned before, the difficulty is the free surface. The "shallow depth" assumption gives rise to the non-linear shallow water theory (non-linear initial problem) (Toro, 2001) which can be seen from the following derivation of 1D Saint Venant Equations.

We define the bottom water flow boundary (or soil bed) by a function

$$z = z_b(x, t), \tag{2.7}$$

and the free surface by a function

$$z = z_s(x, t). \tag{2.8}$$

The description function of the bottom and the free surface can be written into the form

$$F(x, z, t) = 0, \tag{2.9}$$

where for the free surface we have

$$F_s(x, z, t) = z_s(x, t) - z = 0, \tag{2.10}$$

and for the bottom boundary we have

$$F_b(x, z, t) = z_b(x, t) - z = 0. \tag{2.11}$$

According to Lamb (1932), any fluid particle on a fluid free surface, remains there and therefore any displacement of the fluid particles should leave the function unchanged, thus $\frac{DF_s}{Dt} = 0$ i.e.

$$\frac{\partial z_s}{\partial t} + u_s\frac{\partial z_s}{\partial x} - w_s = 0, \tag{2.12}$$

where u_s and w_s represent the values of corresponding flow velocity components at free surface.

For no slip bottom boundary $u_b = w_b = 0$ and if we assume the bed is non erodible, we have

$$\frac{DF_b}{Dt} = \frac{\partial z_b}{\partial t} = 0. \tag{2.13}$$

The water pressure p_w is assumed to be hydrostatic and defined as

$$p_w = \rho g(z_s - z) = \rho g(h + z_b - z), \tag{2.14}$$

where $h = z_s - z_b$, thus

$$\frac{\partial p_w}{\partial x} = \rho g(\frac{\partial h}{\partial x} + \frac{\partial z_b}{\partial x}). \tag{2.15}$$

Integrating the mass conservation equation (2.4) from the bed to the free surface, we have

$$\int_{z_b}^{z_s} \frac{\partial u}{\partial x} dz + w|_{z_b}^{z_s} = 0, \tag{2.16}$$

and define a vertically depth average velocity u^* as

$$u^* = \frac{1}{h} \int_{z_b}^{z_s} u dz. \tag{2.17}$$

Applying Leibniz's rule to (2.16) and using (2.17) and (2.12) along with the no slip bottom boundary, we get

$$\frac{\partial (hu^*)}{\partial x} + \frac{\partial z_s}{\partial t} = 0. \tag{2.18}$$

Substituting $z_s = z_b + h$ into (2.18) and using the assumption that the soil bed is assumed to be non-erodible $\frac{\partial z_b}{\partial t} = 0$, (2.18) simplifies to

$$\frac{\partial h}{\partial t} + \frac{\partial hu^*}{\partial x} = 0. \tag{2.19}$$

Consider now the momentum equation (2.5). Multiplying (2.4) by u and adding to (2.5a) gives

$$\frac{\partial u}{\partial t} + \frac{\partial u^2}{\partial x} + \frac{\partial (uw)}{\partial z} = -\frac{1}{\rho} \frac{\partial p_w}{\partial x} + R_x, \tag{2.20}$$

in which R_x accounts for all the stress terms. Integrating (2.20) and using (2.15) for $\frac{\partial p_w}{\partial x}$, results in

$$\int_{z_b}^{z_s} \frac{\partial u}{\partial t} dz + \int_{z_b}^{z_s} \frac{\partial u^2}{\partial x} dz + (uw)|_{z_b}^{z_s} = -g \int_{z_b}^{z_s} [\frac{\partial h}{\partial x} + \frac{\partial z_b}{\partial x}] dz - ghS_f, \tag{2.21}$$

where

$$-ghS_f = \frac{\mu}{\rho} \int_{z_b}^{z_s} (\frac{\partial^2 u}{\partial x^2} + \frac{\partial^2 u}{\partial z^2}) dz - \int_{z_b}^{z_s} (\frac{\partial \overline{u'^2}}{\partial x} + \frac{\partial \overline{u'w'}}{\partial z}) dz. \tag{2.22}$$

Applying Leibniz's rule and (2.17) to (2.21) and taking the approximation that

$$u^{*2} = \frac{1}{h} \int_{z_b}^{z_s} u^2 dz, \tag{2.23}$$

then (2.21) becomes

$$\begin{aligned} &[\frac{\partial (u^* h)}{\partial t} - u_s \frac{\partial z_s}{\partial t}] + [\frac{\partial (hu^{*2})}{\partial x} - u_s^2 \frac{\partial z_s}{\partial x}] + [u_s \frac{\partial z_s}{\partial t} + u_s^2 \frac{\partial z_s}{\partial x}] \\ &= -gh \frac{\partial h}{\partial x} - gh \frac{\partial z_b}{\partial x} - ghS_f, \end{aligned} \tag{2.24}$$

or

$$\frac{\partial (hu^*)}{\partial t} + \frac{\partial (hu^{*2})}{\partial x} + g \frac{\partial (h^2/2)}{\partial x} = gh(\frac{-\partial z_b}{\partial x} - S_f). \tag{2.25}$$

If the bed is erodible, any movement of fluid particles on the bed is due to the change in the bed position through time, thus $\frac{DF_b}{Dt} = \partial z_b / \partial t$. Assuming the bed is still no slip, i.e. there is no fluid flow through the bed and $u_b = w_b = 0$. Then the mass conservation equation becomes

$$\frac{\partial h}{\partial t} + \frac{\partial (hu^*)}{\partial x} = \frac{-\partial z_b}{\partial t}, \tag{2.26}$$

since $z_s = h + z_b$. The momentum conservation equation (2.25) still holds for erodible bed.

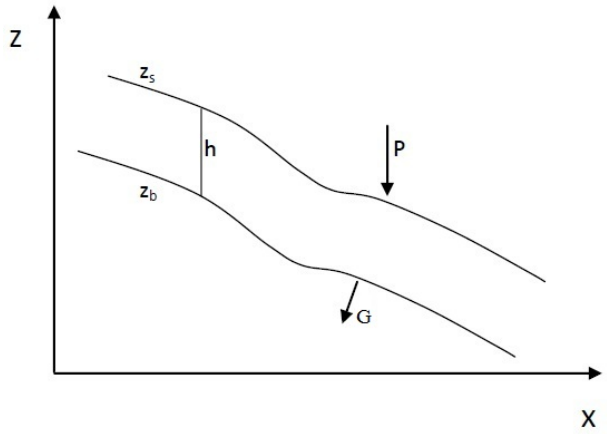

Figure 2.7: Geometry of free surface water flow on vertical and horizontal $z - x$ plane

2.1.2 St Venant Equations with Rainfall and Infiltration Over an Evolving Bed

In the following section, the St Venant equations with rainfall and infiltration conditions are going to be derived for two commonly used but different coordinate systems.

(a) First a vertical and horizontal coordinate system is used to depict the geometry of free surface water flow as presented in Fig. (2.7).

With rainfall input, the displacement of the fluid particles on the free surface is directly affected by the rainfall rate, thus $DF_s/Dt - P(t) = 0$ i.e.

$$\frac{\partial z_s}{\partial t} + u_s \frac{\partial z_s}{\partial x} - w_s = P(t). \tag{2.27}$$

If water flows through the bottom of an evolving bed due to infiltration, then the water crosses the boundary in a direction normal to it and given by infiltration rate G, thus bottom kinematic boundary condition becomes $DF_b/Dt - G_v = \frac{\partial z_b}{\partial t}$ i.e.

$$\frac{\partial z_b}{\partial t} + u_b \frac{\partial z_b}{\partial x} - w_b = G_v(t) + \frac{\partial z_b}{\partial t}, \tag{2.28}$$

where G_v is the vertical component of G given by

$$G_v = G\cos\theta, \qquad \theta = \tan^{-1}(\frac{-\partial z_b}{\partial x}). \tag{2.29}$$

Integrating (2.4) and using (2.27) and (2.28) gives

$$\frac{\partial(hu^*)}{\partial x} + u_b\frac{\partial z_b}{\partial x} - u_s\frac{\partial z_s}{\partial x} + (\frac{\partial z_s}{\partial t} + u_s\frac{\partial z_s}{\partial x} - P) - (u_b\frac{\partial z_b}{\partial x} - G_v) = 0, \tag{2.30}$$

which after canceling the terms in u_s and u_b, and substituting for $h = z_s - z_b$, gives

$$\frac{\partial h}{\partial t} + \frac{\partial(hu^*)}{\partial x} = P - G_v - \frac{\partial z_b}{\partial t}. \tag{2.31}$$

Equation (2.21) still holds here and we apply Leibniz's rule along with (2.23), (2.27) and (2.28) to get

$$\begin{aligned}&[\frac{\partial(u^*h)}{\partial t} - u_s\frac{\partial z_s}{\partial t} + u_b\frac{\partial z_b}{\partial t}] + [\frac{\partial(hu^{*2})}{\partial x} - u_s^2\frac{\partial z_s}{\partial x} + u_b^2\frac{\partial z_b}{\partial x}] + u_s[\frac{\partial z_s}{\partial t} + u_s\frac{\partial z_s}{\partial x} - P]\\ &- u_b[u_b\frac{\partial z_b}{\partial x} - G_v] = -gh\frac{\partial h}{\partial x} - gh\frac{\partial z_b}{\partial x} - ghS_f,\end{aligned} \tag{2.32}$$

or

$$\frac{\partial(hu^*)}{\partial t} + \frac{\partial(hu^{*2})}{\partial x} + g\frac{\partial(h^2/2)}{\partial x} = gh(\frac{-\partial z_b}{\partial x} - S_f) + u_sP - u_b(G_v + \frac{\partial z_b}{\partial t}). \tag{2.33}$$

Combining (2.31) and (2.33) results in

$$\frac{\partial u^*}{\partial t} + u^*\frac{\partial u^*}{\partial x} + g\frac{\partial h}{\partial x} = g(\frac{-\partial z_b}{\partial x} - S_f) + \frac{1}{h}(u_sP - u_bG_v - u_b\frac{\partial z_b}{\partial t}) - \frac{u^*}{h}(P - G_v). \tag{2.34}$$

While the terms involving P, G_v and $\frac{\partial z_b}{\partial t}$ are important components in the mass conservation equation of (2.31), their contributions to the momentum equation (2.34) are small and therefore generally neglected.

(b) Secondly a coordinate system aligned with the flow is used to depict the geometry of free surface water flow as presented in Fig. (2.8).

Here h is no longer the vertical height from the water surface to the bed but is normal to the average slope of the bed surface. The velocity u and flux q are now in the downstream direction also. We define α is the angle of the average

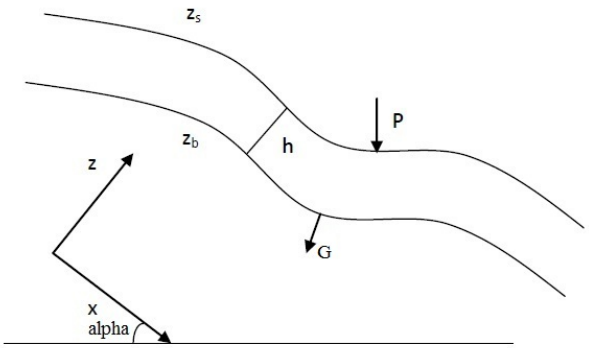

Figure 2.8: Geometry of free surface water flow on $z - x$ plane aligned with free surface

bed slope to the horizontal and therefore the bed gradient $\partial z_b/\partial x$ is now with respect to the average bedslope. Thus $\partial z_b/\partial x = 0$ corresponds to flow down a surface of constant slope.

At any point on the bed surface, the angle it makes to the horizontal is given by

$$\theta = \alpha + tan^{-1}(\frac{-\partial z_b}{\partial x}). \tag{2.35}$$

For small changes in gradient, then we can show

$$\sin\theta = \sin\alpha + \frac{-\partial z_b}{\partial x} = S_o + \frac{-\partial z_b}{\partial x}. \tag{2.36}$$

where S_o is the average slope of plane.

For this coordinate system the kinematic surface and bed condition become

$$\frac{\partial z_s}{\partial t} + u_s\frac{\partial z_s}{\partial x} - w_s = P(t)\cos\alpha, \tag{2.37}$$

and

$$\frac{\partial z_b}{\partial t} + u_b\frac{\partial z_b}{\partial x} - w_b = G_\alpha(t) + \frac{\partial z_b}{\partial t}, \tag{2.38}$$

where G_α is the component of G which is normal to plane at angle α.

Doing the similar derivation as in case (a), we can obtain the mass conservation equation as

$$\frac{\partial h}{\partial t} + \frac{\partial (hu^*)}{\partial x} = P\cos\alpha - G_\alpha - \frac{\partial z_b}{\partial t}. \tag{2.39}$$

In the rotated coordinate system, (2.5a) will have a gravity component, thus it should be replaced with

$$\begin{aligned} &\frac{\partial u}{\partial t} + u\frac{\partial u}{\partial x} + v\frac{\partial u}{\partial y} + w\frac{\partial u}{\partial z} \\ =&g\sin\alpha - \frac{1}{\rho}\frac{\partial p_w}{\partial x} + \nabla\cdot(\frac{\mu}{\rho}\nabla u) - [\frac{\partial \overline{u'^2}}{\partial x} - \frac{\partial \overline{u'v'}}{\partial y} - \frac{\partial \overline{u'w'}}{\partial z}], \end{aligned} \tag{2.40}$$

and the hydrostatic pressure term is now

$$p_w = \rho g\cos\alpha(h + z_b - z). \tag{2.41}$$

Following the same steps as before and integrating over the depth gives

$$\int_{z_b}^{z_s}\frac{\partial u}{\partial t}dz + \int_{z_b}^{z_s}\frac{\partial u^2}{\partial x}dz + u_s w_s - u_b w_b = gh\sin\alpha - g\cos\alpha\int_{z_b}^{z_s}[\frac{\partial h}{\partial x} + \frac{\partial z_b}{\partial x}]dz - ghS_f. \tag{2.42}$$

Applying Leibniz's rule along with (2.37) and (2.38) to the above equation results in

$$\begin{aligned} &[\frac{\partial (u^*h)}{\partial t} - u_s\frac{\partial z_s}{\partial t} + u_b\frac{\partial z_b}{\partial t}] + [\frac{\partial (hu^{*2})}{\partial x} - u_s^2\frac{\partial z_s}{\partial x} + u_b^2\frac{\partial z_b}{\partial x}] + \\ &u_s[\frac{\partial z_s}{\partial t} + u_s\frac{\partial z_s}{\partial x} - P\cos\alpha] - u_b[u_b\frac{\partial z_b}{\partial x} - G_\alpha] \\ =&gh\sin\alpha - gh\cos\alpha(\frac{\partial h}{\partial x} + \frac{\partial z_b}{\partial x}) - ghS_f, \end{aligned} \tag{2.43}$$

or

$$\frac{\partial (hu^*)}{\partial t} + \frac{\partial (hu^{*2})}{\partial x} + g\cos\alpha\frac{\partial (h^2/2)}{\partial x} = gh(S_o + \cos\alpha\frac{-\partial z_b}{\partial x} - S_f) + u_s P\cos\alpha - u_b(G_\alpha + \frac{\partial z_b}{\partial t}). \tag{2.44}$$

Combining it with mass conservation equation gives

$$\begin{aligned} &\frac{\partial u^*}{\partial t} + u^*\frac{\partial u^*}{\partial x} + g\cos\alpha\frac{\partial h}{\partial x} \\ =&g(S_o + \cos\alpha\frac{-z_b}{\partial x} - S_f) + \frac{1}{h}(u_s P\cos\alpha - u_b G_\alpha - u_b\frac{\partial z_b}{\partial t}) - \frac{u^*}{h}(P\cos\alpha - G_\alpha). \end{aligned} \tag{2.45}$$

Choosing coordinate system (a) or (b) is determined by the measured value of h and u^*. For horizontal and vertical coordinate system, h is the vertical height from the water surface to the bed and u^* is the flow velocity in x direction. However, for coordinate system aligned with flow, h is normal to the average slope of the bed surface and u^* is in the downstream direction.

2.1.3 Kinematic and Diffusive Wave Approximation

For the rest of the thesis, we will only consider the St Venant equations on a coordinate system aligned with the downstream direction as in (2.39) and (2.44). Additionally flows over a non-erodible bed are considered along with small slope angles such that $\cos\alpha \simeq 1$. Finally the "stars" are dropped for u and v and from now on, u and v implicitly refer to u^* and v^*. The 2D St Venant equations on this system can be derived similarly as 1D equations and expressed as

$$\frac{\partial h}{\partial t} + \frac{\partial (hu)}{\partial x} + \frac{\partial (hv)}{\partial y} = P(x,y,t) - G(x,y,t) = R(x,y,t), \tag{2.46}$$

$$\frac{\partial (hu)}{\partial t} + \frac{\partial (hu^2 + 0.5gh^2)}{\partial x} + \frac{\partial (huv)}{\partial y} = gh(S_{ox} - S_{fx}), \tag{2.47}$$

$$\frac{\partial (hv)}{\partial t} + \frac{\partial (huv)}{\partial x} + \frac{\partial (hv^2 + 0.5gh^2)}{\partial y} = gh(S_{oy} - S_{fy}), \tag{2.48}$$

where S_{fx} and S_{fy} are the bed friction terms given by Manning's equation as

$$S_{fx} = \frac{n^2 u\sqrt{u^2+v^2}}{h^{4/3}}, \quad S_{fy} = \frac{n^2 v\sqrt{u^2+v^2}}{h^{4/3}}, \tag{2.49}$$

or given by Darcy-Weisbach equation as

$$S_{fx} = \frac{C_D u\sqrt{u^2+v^2}}{gh}, \quad S_{fy} = \frac{C_D v\sqrt{u^2+v^2}}{gh}, \tag{2.50}$$

where n is Manning's friction coefficient and $C_D = f/8$ with f is the Darcy-Weisbach friction factor. The direct effects of rainfall and infiltration on the x and y momentum equations are assumed to be negligible.

In general, the St Venant equations can't be solved analytically and can be quite demanding computationally to obtain numerical solutions. Consequently it

has been usual to consider simplifications based on specialized flow conditions. The kinematic and diffusion wave approximations are two such widely used simplifications (refer to Fig. (2.9) to see the differences between these two waves). For the kinematic wave approximation, the weight component of fluid in the direction of the channel is assumed to be equal to the resistive forces due to channel bed friction, i.e.

$$S_{ox} = S_{fx},\ S_{oy} = S_{fy}. \tag{2.51}$$

Using Manning's equation in (2.51) gives the solutions for u and v velocity components as

$$u = \frac{\sqrt{S_{ox}}}{n(1 + S_{oy}^2/S_{ox}^2)^{1/4}} h^{2/3} = K_x h^{2/3}, \tag{2.52}$$

$$v = \frac{\sqrt{S_{oy}}}{n(1 + S_{oy}^2/S_{ox}^2)^{1/4}} h^{2/3} = K_y h^{2/3}. \tag{2.53}$$

If Darcy-Weisbach equation is used in (2.51), the u and v would be given by

$$u = \frac{\sqrt{gS_{ox}/C_D}}{(1 + S_{oy}^2/S_{ox}^2)^{1/4}} h^{1/2} = K_x h^{1/2}, \tag{2.54}$$

$$v = \frac{\sqrt{gS_{oy}/C_D}}{(1 + S_{oy}^2/S_{ox}^2)^{1/4}} h^{1/2} = K_y h^{1/2}. \tag{2.55}$$

Since we have explicit expressions for u and v in terms of the height h, (2.46) reduces to a single partial differential equation

$$\frac{\partial h}{\partial t} + \frac{\partial q_x}{\partial x} + \frac{\partial q_y}{\partial y} = R, \tag{2.56}$$

where $q_x = K_x h^m$, $q_y = K_y h^m$ with $m = 5/3$ (Manning) or $3/2$ (Dary-Weisbach). Equation (2.56) is known as the 2D kinematic wave model for shallow overland flow.

When the inertial forces are still neglected but the pressure forces are not, the Saint Venant Eqautions can be approximated by the diffusion or non-inertia wave equations. This is given by combining (2.46) with the following equations

$$\frac{\partial h}{\partial x} = S_{ox} - S_{fx},\ \ \frac{\partial h}{\partial y} = S_{oy} - S_{fy}. \tag{2.57}$$

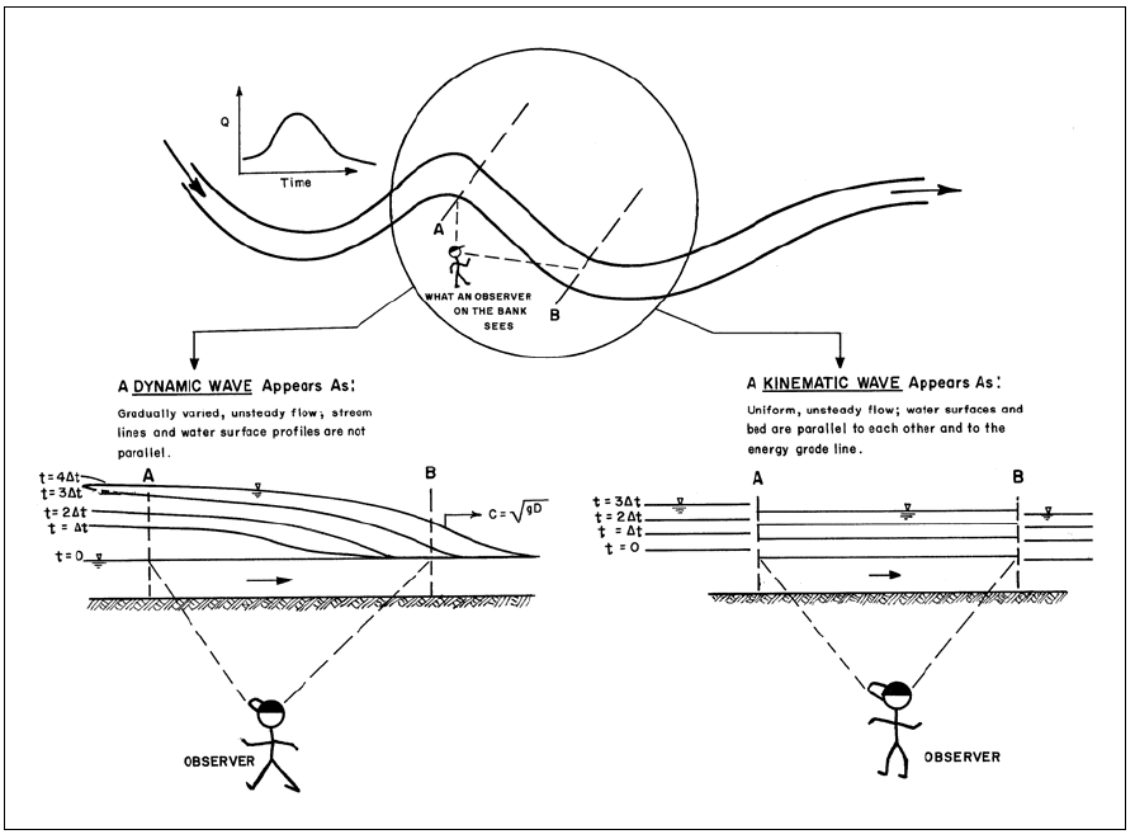

Figure 2.9: Comparison of Kinematic Wave and Dynamic Wave (from MacArthur and J.Devries (1993))

Viera (1983), Govindaraju and Kavvs (1991) have shown that the diffusion wave equations may be used under conditions of steep rough slopes. The applicability of the 1D diffusion wave approximation to reproduce experimental data has been shown by Govindaraju and Kavvs (1991).

The criteria for using the kinematic wave or diffusive wave approximations to the St Venant Equations have been proposed by Woolhiser and Liggett (1967), Ponce *et al.* (1978) and Morris and Woolhiser (1980). In Woolhiser and Liggett (1967), they gave the dimensionless solutions for the rising hydrograph for unsteady 1D flow over a plane. Through comparing to a nondimensional numerical solution of the St Venant equations, they found that for a kinematic wave number $k = \frac{S_0 L}{h(L)F_r^2(L)} > 20$, the kinematic wave equation was a good approximation to the Saint Venant equations. Ponce *et al.* (1978) examined the applicability of the kinematic and diffusive wave models for open channel flow by utilizing a linear stability analysis of Saint Venant equations. They concluded that most overland flow can be approximated by kinematic flow. However as mentioned in Morris and Woolhiser (1980), Ponce *et al.* (1978) did not consider the lateral inflow and flow boundary conditions in their discussion. Morris and Woolhiser (1980) adopted the approach of Woolhiser and Liggett (1967) and included the effect of lateral inflow along with upstream and downstream boundary conditions. They demonstrated that at low Frounde number $F_r = \frac{u}{\sqrt{gh}}$ and high k, the diffusive wave equation was a good approximation to Saint Venant equations; the kinematic wave approximation can be used if $k > 20$, but for low values of F_r ($F_r < 0.5$), an additional condition needs to be satisfied, i.e. $F_r^2 k \geq 5$ (Morris and Woolhiser, 1980). In practice, a wide range of shallow overland flows can be solved by using the simpler kinematic wave approximation, including the flows considered in this thesis. Consequently, only the kinematic wave equation will be considered from now on.

The assumptions behind the overland flow equations are therefore give as below.

St Venant equations

- The depth averaged flow velocity is appropriate
- It will not apply when flow separation is significant or there is vertical circulation in the flow
- It applies for Froude number $F_r < 1$ or $F_r > 1$

Kinematic flow equation

- The flow acceleration and hydrostatic pressure forces are not important
- The bed slope and bed friction are in balance
- The Froude number $F_r \ll 1$, kinematic number $k > 20$ and $F_r^2 k \geq 5$
- There is no interaction between bed evolution and the flow of water

Diffusive flow equation

- The flow acceleration is not important but hydrostatic pressure force is
- Froude number $F_r < 1$

2.1.4 Solutions to the 1D Kinematic Wave Equation

In this section, the analytical solutions which have been obtained for the 1D kinematic wave equation

$$\frac{\partial h}{\partial t} + \frac{\partial (K h^m)}{\partial x} = P - G = R, \tag{2.58}$$

will be briefly introduced.

Henderson and Wooding (1964) was the first paper to give an explicit analytical solution to (2.58) with $R = P =$ constant > 0. They ignored infiltration and

considered a constant rainfall rate and used the method of characteristics (earlier introduced in Lighthill and Whitham (1955)) to obtain the solution

$$h = (\frac{Rx}{K})^{\frac{1}{m}}, \quad x \leq KR^{m-1}t^m, \tag{2.59}$$

$$h = Rt, \quad x \geq KR^{m-1}t^m, \tag{2.60}$$

for the initial and boundary conditions

$$\begin{aligned} h(x,0) &= 0, \;\; x > 0; \\ h(0,t) &= 0, \;\; t > 0. \end{aligned} \tag{2.61}$$

Sherman and Singh (1976a) developed analytical solutions for the kinematic wave flow on a converging surface (Fig. (2.10)) with $R = P =$ constant > 0. The kinematic wave equation is written as

$$\frac{\partial h}{\partial t} + \frac{\partial (Kh^m)}{\partial x} = R + \frac{uh}{L_0 - x}, \tag{2.62}$$

with the boundary and initial conditions

$$\begin{aligned} h(x,0) &= 0, \;\; 0 \leq x \leq L_0(1-r), \\ h(0,t) &= 0, \;\; 0 \leq t, \end{aligned} \tag{2.63}$$

where u is the flow velocity, L_0 is the length of the converging section and $L_0(1-r)$ is the length of flow as shown in Fig. (2.10).

The analytical solution is expressed in terms of the beta and incomplete beta functions as

$$\begin{aligned} h(x,t_0) &= (P/2)^{\frac{1}{m}}[\frac{L_0^2 - (L_0 - x)^2}{K(L_0 - x)}]^{\frac{1}{m}}, \;\; x \leq \int_0^t mKh^{m-1}dt; \\ h(x,x_0) &= (P/2)^{\frac{1}{m}} K^{-\frac{1}{m}}[\frac{(L_0 - x_0)^2 - (L_0 - x)^2}{L_0 - x}]^{\frac{1}{m}}, \;\; x \geq \int_0^t mKh^{m-1}dt \end{aligned} \tag{2.64}$$

where t_0 and x_0 can be calculated from

$$t_0 = t - (\frac{\xi}{2})(L_0/K)^{1/m}[\beta(a_1,a_2) - \beta_\phi(a_1,a_2)], \tag{2.65}$$

$$a_1 = 1 - \frac{2}{m}, \quad a_2 = \frac{1}{m}, \quad \phi = [(L_0 - x)/L_0]^2, \tag{2.66}$$

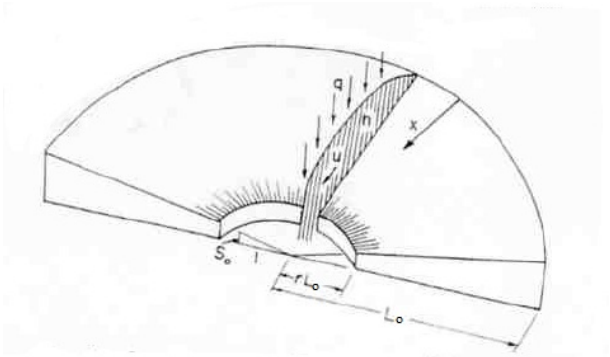

Figure 2.10: Geometry of converging overland flow model (from Sherman and Singh (1976a))

and

$$x_0 = L_0 - K(\frac{2}{\xi}\frac{t}{\beta(a_2,b_2) - \beta_\varphi(a_2,b_2)})^m, \tag{2.67}$$

$$a_2 = 1 - \frac{1}{2m}, \quad b_2 = \frac{1}{m}, \quad \varphi = (\frac{L_0 - x}{L_0 - x_0})^2. \tag{2.68}$$

where

$$\xi = m^{-1}(2/P)^{(m-1)/m}, \quad \beta(a_n,a_m) = \frac{\Gamma(a_n)\Gamma(a_m)}{\Gamma(a_n+a_m)}, \tag{2.69}$$

$$\beta_\eta(a_n,a_m) = \frac{\eta^{a_n}(1-\eta)^{a_m}}{a_n}[1 + \sum_{j=0}^{\infty}\frac{\beta(a_n+1,j+1)}{\beta(a_n+a_m,j+1)}\eta^{j+1}]. \tag{2.70}$$

Sherman and Singh (1976b) extended the solution in Sherman and Singh (1976a) for the case when the infiltration is taken into account on the converging surface. The solution is presented as in (2.64) to (2.70) with P being replaced by R and ξ being replaced by ξ^* where

$$R = P - G, \quad \xi^* = m^{-1}(2/R)^{(m-1)/m}. \tag{2.71}$$

A similarity solution is presented in Campbell *et al.* (1984) for (2.62) and (2.63) when R is proportional to any power of time (i.e. $R = St^{\lambda_1 - 1}$). The similarity solution reduced (2.62) to only one ordinary differential equation by

applying similarity variable $\phi = (L_0 - x)t^{\gamma^*}$ to (2.62). The ODE is then written as

$$\frac{dF_1}{d\phi} = \frac{S - \lambda_1 F_1 - (K/\phi)F_1^m}{mKF_1^{m-1} + \gamma^*\phi}, \tag{2.72}$$

where F_1 is a function of ϕ and λ_1, m and γ^* satisfy

$$\lambda_1(m-1) + 1 + \gamma^* = 0. \tag{2.73}$$

An analytical solution to $F_1(\phi)$ can be found when R is taken constant, $\lambda_1 = 1$, $\gamma^* = -m$ and is given by

$$\phi = (2K/R)F_1^m. \tag{2.74}$$

Sherman (1976) shows that (2.58) and (2.62) under the initial and boundary conditions of (2.61), can be converted to each other. Hence the solution for (2.62) can be obtained from the solution of (2.58) by replacing of h, P and K with $\overline{h}$, $\overline{P}$ and $\overline{K}$ which are

$$\overline{h} = (L_0 - x)h, \quad \overline{P} = (L_0 - x)P, \quad \overline{K} = \frac{k}{(L_0 - x)^{m-1}}. \tag{2.75}$$

Comparing to Henderson and Wooding (1964), Sherman (1976) extended the solution for (2.58) to allow for rainfall rate P and infiltration rate G to vary with x (though for this case, the solutions can not be solved analytically in general).

Parlange *et al.* (1981) considered the case when the excess rainfall rate R is a function of t with $R \geq 0$ for $t \geq 0$. They presented a general analytical solution for (2.58) with the initial and boundary conditions of (2.61).

The solution is expressed as

$$h = \int_{t_0}^{t} R(t')dt', \quad x = mK\int_{t_0}^{t}[\int_{t_0}^{\bar{t}} R(t')dt']^{m-1}d\bar{t}, \quad x \leq x_c; \tag{2.76}$$

$$h = \int_{0}^{t} R(t')dt', \quad x \geq x_c, \tag{2.77}$$

where $0 \leq t_0 \leq t$ and

$$x_c = mK\int_{0}^{t}[\int_{0}^{\bar{t}} R(t')dt']^{m-1}d\bar{t}. \tag{2.78}$$

Note that for constant R, (2.76) to (2.78) reduce to the solution of Henderson and Wooding (1964). Parlange *et al.* (1981) applied their solutions for a single peak excess rainfall rate given by $R = R_0 e^{-t/\tau}(1 - e^{-t/\tau})$ where R_0 and τ are arbitrary constants, which determine the width and peak of $R(t)$.

Cundy and Tento (1985) presented an explicit solution for (2.58) for a constant rainfall rate P and infiltration rate $G(t)$ given by Philip's equation (Philip, 1969). They also considered the same boundary and initial conditions of (2.61).

Defining t^* as the time when the rainfall rate equals to the infiltration rate, i.e. $R = 0$, then their solution needs to be separated into two regimes. One is for $R = P - G > 0$ when $0 < t < t^*$, another one is for $R = P - G < 0$ when $t \geq t^*$.

While Cundy and Tento (1985) were able to obtain an explicit solution for their particular $R(t)$ function, Sander *et al.* (1990) generalized their solution for R being an arbitrary function of time and having the property of $R(t) \geq 0$ for $t \leq t^*$ and $R(t) < 0$ for $t > t^*$. For the first time regime, the solution is given as (2.76) and (2.77). For the second time regime, the solution has the same form as in the regime $t \leq t^*$ but t_0 varies in the range $0 < t_0 \leq t_2$ where t_2 can be calculated from

$$\int_{t_2}^{t} R(\bar{t})d\bar{t} = 0. \tag{2.79}$$

Physically t_2 defines the upslope edge of the free drying surface when it is traveling down the hillslope. For $t > t^*$, $h = 0$ no longer occurs at $x = 0$ (as $G > P$) but is given by $t_0 = t_2$ and occurs at

$$x = mK \int_{t_2}^{t} [\int_{t_2}^{\bar{t}} R(\bar{\bar{t}})d\bar{\bar{t}}]^{m-1} d\bar{t}. \tag{2.80}$$

The solution was evaluated for a single peak $R = R_0(e^{-t/\tau} - k_{sat}/R_0)(1 - e^{-t/\tau})$ which had the property of $R \to -k_{sat}$ as $t \to \infty$ where k_{sat} is saturated hydraulic conductivity.

2.2 Soil Erosion

Soil erosion modeling has wide applications. It can be used to study the loss of productive soil from agricultural fields; reduction in soil productivity and its impact on crop yields; land degradation; the transport of attached chemicals such as fertilizers and pesticides and the eutrophication of surface water bodies. Soil erosion does lead directly to the pollution of river estuaries and can have a significant impact on the local ecology. For example, there is a 22,000 square km hypoxia zone near the mouth of the Mississippi river and is due directly to the erosion of upstream farmlands containing high loads of nitrogen (Rabalais *et al.*, 2007). The frequent occurrence of red tides in Bohai (China) is closely related to the large amount of nutrient inputs from the Yellow river which not only accounts for up to 50% of inflow to Bohai but carries high loads of nitrogen from eroded farmlands (Jiang *et al.*, 2005; Yu *et al.*, 2010; Zhao *et al.*, 2002). The algae bloom in the Taihu lake area in China has led to the lack of high quality water resources for the local people and the economy. These algae blooms have resulted directly from the accumulation of nitrogen and phosphorus arising from upstream erosion (Hu *et al.*, 2008). The reliable prediction of soil erosion and the transport of attached chemicals, can be used to develop management strategies for minimizing sediment and chemical transport, thereby reducing its impact on the environment.

Early in the last century, because of inappropriate application of European-based land management methods to countries such as the USA and Australia, the natural rates of soil erosion were dramatically accelerated resulting in serious land degradation problems in these countries. The problems motivated people to do research into soil erosion, especially in the USA (Hudson, 1981). In this section, the main soil erosion models are reviewed and their range of applications is discussed. In particular, special attention is paid to the Hairsine-Rose model, the progress in finding solutions to this model and its application to experimental data.

2.2.1 Soil Erosion Models

In 1907, a policy of land protection was declared by the United States Department of Agriculture (USDA), which led to the development of research programmes on the effect of different land management and treatments on water flow and levels of soil erosion in chosen fields. With the establishment of Federal and State Experiment Stations, this research was expanded and accelerated, with 1928 to 1958 being a period of intensive collection and tabulation of runoff and soil loss data (Sander *et al.*, 2007b). The analysis from these experiments provided guidance on the role of many factors and agronomic treatments in controlling soil loss (Ayres, 1936). Also, based on the large amount of data collected by USDA, Wishmeier and Smith (1960) developed the famous Universal Soil Loss Equation (USLE) which was classified later as an **empirically based** mathematical model (a model constructed basing on collected data and limited to conditions for which the data was obtained). At that time, rainfall seemed to be considered as a more important mechanism than runoff in the process of soil erosion as reflected in the studies by Laws (1940), Ellison (1947), Ekern (1951) and Hudson (1957).

The USLE is a combination of five factors which is given as

$$A = RR \times Kr \times LS \times CP \times PP, \tag{2.81}$$

where A represents the potential long term average annual soil loss;

RR is the rainfall and runoff factor by geographic location;

Kr is the soil erodibility and depends on the organic matter and texture of the soil, its permeability and profile structure;

LS is the topographical factor and depends on both the length and gradient of the slope;

CP the plant cover factor and is a simple relation between erosion on bare soil and erosion observed under a cropping system;

PP is a factor that takes account of specific erosion control practices such as contour tilling or mounding, or contour ridging.

The USLE has had historical dominance in studying soil erosion and conservation measures because it is a practically oriented approach, easy to understand and to use. However it has limitations as has been pointed out in Wishchmeier (1976):

- The estimation of the soil loss is for specific geographic areas and particular land use and management
- The calculation applies for long-term (over 20 years) average, not for individual erosion events
- The equation only considers rain as the source of energy, not overland flow needed for entrainment, so it only applies to sheet flow below the critical shear stress
- This method focuses on net erosion process itself, it doesn't apply to situation where net deposition of sediments is occurring.

To overcome the limitations of USLE, various modifications have been made. The most widely used improved USLE model is Revised USLE (RUSLE) which was developed by Renard *et al.* (1994). It uses the same formula as USLE but includes some refinements to the determining factors. Another modified USLE is called MUSLE which is an attempt to compute soil loss for a single storm event (Aksoy and Kavvas, 2005). Other empirically based models like SEDD – SEdiment Delivery Distributed (Ferro, 2000) and AGNPS – AGricultural NonPoint Source (Young *et al.*, 1989) are derived from USLE. The USLE and its successors have a common character that is they all concentrate on estimating the quantity of soil loss and do not describe the actual soil erosion process which turns to be a more important objective in recent soil erosion research.

The alternative to empirical approaches has been to develop more **physically based** erosion and sediment transport models (models that are developed from

mass conservation equations (Aksoy and Kavvas, 2005)). The mass conservation equation for sediment laden water flowing down a sloping surface is written as

$$\frac{\partial(hc)}{\partial t} + \frac{\partial(qc)}{\partial x} = E_r, \tag{2.82}$$

where h is water depth (m), c is suspended sediment concentration (kg m^{-3}), q is volumetric flux per unit width ($m^2 \ \ s^{-1}$), qc is the sediment flux (kg $m^{-1}s^{-1}$) and E_r (kg $\ m^{-2}s^{-1}$) includes all processes which add to or remove sediment from the flow. Both h and q are determined for solutions from the St Venant equation for overland flow, and usually from the kinematic wave approximation to these equations.

In the content below, we are going to introduce some representative models based on (2.82). Although all these models include equations for determining both runoff and soil erosion, we only focus on how they model the soil erosion process.

ANSWERS (Beasley *et al.*, 1980) is a model designed for erosion on agricultural watersheds and is event-oriented. It divides the watershed into small and independent elements and treats the runoff and erosion process as independent functions of the hydrologic and erosion related parameters in each element. The erosion process assumes that soil particles can be detached by rainfall and runoff but only can be transported by runoff. The deposited sediment is assumed to require the same amount of energy as required for the original soil for re-detachment in this model (Aksoy and Kavvas, 2005). ASWERS uses the steady state form of (2.82) and $E_r = D_R + D_F$ (Foster and Meyer, 1972) where D_R is the rate of detachment by rainfall ($kg \ \ m^{-2} \ \ s^{-1}$) and D_F is the rate of detachment by runoff ($kg \ \ m^{-2} \ \ s^{-1}$). They are formulated as

$$D_R = 0.027 C_{cr} K_r A_I P^2, \tag{2.83}$$

and

$$D_F = 0.018 C_{cr} K_r A_I S_0 q, \tag{2.84}$$

where C_{cr} is the cropping and management factor, K_r is the soil erodibility factor, A_I is an area increment (m^2), P is rainfall intensity ($mm \;\; min^{-1}$), S_0 is slope steepness and q is the flow rate per unit width ($m^2 \;\; min^{-1}$).

WEPP (Nearing *et al.*, 1989) is a model to predict soil erosion and sediment delivery from field, farms, forest, rangeland, construction sites and urban areas (Laflen *et al.*, 1997). It uses daily continuous simulation to model the generation of runoff. WEPP divides runoff between rills and interrill areas and consequently it calculates erosion in the rills and interrills areas separately (Aksoy and Kavvas, 2005). WEPP also uses the steady state form of (2.82) to describe the hillslope erosion and E_r is expressed as (Nearing *et al.*, 1989)

$$E_r = D_i + D_r, \tag{2.85}$$

where D_i is the rate of erosion between rills ($kg \;\; m^{-2} \;\; s^{-1}$) and D_r is the rate of erosion within a rill ($kg \;\; m^{-2} \;\; s^{-1}$). The interrill erosion is conceptualized as a process of sediment delivery to rills. The rate of interill erosion can be calculated from

$$D_i = K_i I_e^2 C_e G_e \frac{R_s}{W}, \tag{2.86}$$

where K_i is the interrill erodibility parameter, $I_e = [(\int P^2 dt)/t_e]^{0.5}$ is the effective rainfall intensity with t_e the total time when rainfall rate exceeds infiltration rate, C_e is the effect of canopy on interrill erosion, G_e is the effect of ground cover on interrill erosion, R_s is the spacing of rills and W is the computed rill width.

When the sediment load is less than sediment transport capacity, then D_r represents a net detachment process (i.e. more sediment is eroded than deposited) and can be calculated from

$$D_r = K_{rr}(\tau_f - \tau_c)[1 - q_s/T_c], \tag{2.87}$$

where K_{rr} is a rill soil erodibility parameter ($s \;\; m^{-1}$), τ_f is flow shear stress acting on the soil (Pa), τ_c is critical shear stress (Pa), $q_s = qc$ and T_c is sediment transport capacity ($kg \;\; m^{-1} \;\; s^{-1}$) defined as

$$T_c = k_t \tau_f^{3/2}, \tag{2.88}$$

where k_t is a transport coefficient.

When the sediment load is greater than the sediment transport capacity, then D_r represents a net deposition process (i.e. more sediment is deposited than eroded) and can be calculated from

$$D_r = [\delta v_s/q][T_c - q_s], \tag{2.89}$$

where δ is a raindrop induced turbulence coefficient, v_s is the effective fall velocity for the sediment ($m \ \ s^{-1}$).

It is worthwhile noting that while D_r is a continuous function of q_s as the flow transitions from net erosion to net deposition condition, its derivative dD_r/dq_s is not. Physically there is not reason why this should be so as both erosion and deposition processes themselves vary continuously as q_s transitions T_c in response to spatial and temporal evolving flow conditions.

EUROSEM (Morgan *et al.*, 1998) is a model to simulate soil erosion for both individual fields and small catchment. It can simulate the runoff in the rill or between the rills and also can be applied to runoff on smooth planes. EUROSEM is designed as an event-based model since it was thought that erosion was dominated by only a few events per year (Aksoy and Kavvas, 2005). EUROSEM considers net detachment of soil by rainfall and runoff with E_r is formulated as (Morgan *et al.*, 1998)

$$E_r = D_R + D_F. \tag{2.90}$$

Soil detachment by rainfall is calculated by

$$D_R = aKEe^{-\varrho h} \quad (kg \ \ m^{-2} \ \ s^{-1}), \tag{2.91}$$

where a is an experimentally determined index of the rainfall detachability of the soil ($kg \ \ J^{-1}s^{-1}$), KE is the total kinetic energy of the net rainfall at the ground surface ($J \ \ m^{-2}$), ϱ is a soil texture exponent, varying between 0.9 and 3.1 and h is the mean depth of the runoff (m).

Soil detachment by runoff is calculated from

$$D_F = \rho_s \alpha_z v_s (TC - CC) \quad (kg \ \ m^{-2} \ \ s^{-1}), \tag{2.92}$$

where ρ_s is the particle density ($kg\ \ m^{-3}$), α_z is a flow detachment efficiency coefficient (dimensionless), v_s is the particle settling velocity ($m\ \ s^{-1}$), TC is a dimensionless volumetric transport capacity and CC is the volumetric sediment concentration ($= c/\rho_s$).

The volumetric transport capacity for flow in rills is calculated differently from the that of flow between rills. For flow in rills, it is given by the equation of Govers (1990) as

$$TC = (\frac{0.32}{d_{50}+5})^{0.6}(\omega - \omega_{cr})^{\kappa}, \tag{2.93}$$

where d_{50} is the median particle size of the soil (μm), ω is the unit stream power ($=\ 10\ \overline{u}S_0$ in which $\overline{u}$ is mean flow velocity), ω_{cr} is the critical unit stream power ($= 0.4\ cm\ \ s^{-1}$) and κ is the experimentally derived particle size coefficient calculated by

$$\kappa = (\frac{d_{50}+5}{300})^{0.25}. \tag{2.94}$$

For the flow between rills, TC is based on the equation of Everaert (1991), using a range of particle sizes from 33 to 390 μm and is given by

$$TC = \frac{19 - d_{50}/30}{10^4}\frac{1}{\rho_s q}[(\overline{\Omega} - \overline{\Omega}_{cr})^{0.7/5} - 1]^5, \tag{2.95}$$

where $\overline{\Omega}$ is the modified stream power defined by

$$\overline{\Omega} = \frac{(U^*\overline{u})^{3/2}}{h^{2/3}}, \tag{2.96}$$

in which U^* is the shear velocity ($m\ \ s^{-1}$). Now $\overline{\Omega}_{cr}$ is a critical value of $\overline{\Omega}$ given by substituting U_c^* into (2.96) and U_c^* is taken from White (1970) as

$$U_c^* = \sqrt{y_c(\rho_s - 1)gd_{50}}, \tag{2.97}$$

in which y_c is the modified Shields' critical shear velocity based on particle Reynolds number ($m\ \ s^{-1}$) and g is the acceleration due to gravity.

LISEM (De Roo *et al.*, 1996) is a model based on EUROSEM. It is the first erosion model to be completely incorporated in a raster geographic information system (GIS) for easy use. LISEM also considers soil erosion by rainfall and

runoff respectively with an E_r expressed as in (2.90). Since LISEM assumes that the flow across-sectional area can vary with x then h and q in (2.82) must be replaced with $W * h$ and $W * q$ respectively.

The rainfall detachment is described by

$$D_R = (\frac{2.82}{AG} * KE * e^{-1.48h} + 2.96) * (P - I_R) * \frac{\Delta x}{\Delta t}, \quad (kg \;\; s^{-1}) \tag{2.98}$$

where AG is the soil aggregate stability (median number of drops), I_R is the interception (mm), Δx is the size of an element (m) and Δt is the time increment (s) in the GIS. The erosion by runoff is expressed as

$$D_F = \alpha_z * W * v_s * (\frac{T_c - q_s}{q}), \quad (kg \;\; s^{-1}) \tag{2.99}$$

where W is the width of the flow (m) and the coefficient α_z calculated by

$$\begin{aligned} &\alpha_z = 1, \quad \text{for net deposition;} \\ &\alpha_z = \frac{1}{0.89 + 0.56CH}, \quad \text{for net detachment} \end{aligned} \tag{2.100}$$

in which CH is the cohesion of the soil at saturation (KPa).

KINEROS (Smith, 1981; Woolhiser *et al.*, 1990) is an event oriented model and designed for small urban and agricultural watershed soil erosion. Like EUROSEM and LISEM, KINEROS also considers erosion process as a combination of raindrop splash erosion and runoff erosion and does not separate rill and interrill erosion. And it only uses a single-mean sediment particle size in the formulation. The right hand side of (2.82) E_r is expressed as below in KINEROS (for flow of uniform width W).

The erosion rate by rainfall D_R ($kg \;\; m^{-1} \;\; s^{-1}$) is

$$D_R = \begin{cases} \rho_s * c_f * k(h) * P^2/W, & R > 0; \\ 0, & R < 0; \end{cases} \tag{2.101}$$

where c_f is a constant and $k(h)$ is a reduction factor representing the reduction in splash erosion caused by increasing depth of water and it can be given by

$$k(h) = exp(-c_h h), \tag{2.102}$$

in which c_h is a damping coefficient for splash erosion (m^{-1}).

The runoff erosion rate D_F is

$$D_F = \rho_s * c_g * (TC - CC) * h, \quad (kg \;\; m^{-1} \;\; s^{-1}) \tag{2.103}$$

where c_g is a transfer rate coefficient (s^{-1}). The transport capacity defined in KINEROS is

$$TC = \omega_0 S_0^{\beta_0} q^{\gamma_0 - 1} P^{\delta_0} [1 - \frac{\tau_c}{\tau_b}]^{\varepsilon_1}, \quad \tau_e \geq \tau_c. \tag{2.104}$$

where τ_c is the critical shear stress (Pa), τ_b is the bed shear stress (Pa), ω_0, β_0, γ_0, δ_0 and ε_1 are selectable values depending on local hydraulic conditions.

While KINEROS uses only a single-mean particle size to represent the soil, in its modified version KINEROS2 (Smith *et al.*, 1995a,b), the sediment are characterized by a distribution of up to five size class.

WESP (Lopes, 1987; Lopes and Lane, 1988) is also a event-oriented model for small watersheds. The soil erosion mechanisms considered in WESP are the entrainment of sediment by overland flow, sediment entrainment by rainfall and sediment deposition. Thus, E_r in this model is

$$E_r = D_R + D_F - d, \tag{2.105}$$

where D_R is the rate of sediment entrainment by overland flow and expressed as (Croley, 1982; Foster, 1982)

$$D_R = K_R \tau_e^{b_1}, \quad (kg \;\; m^{-1} \;\; s^{-1}) \tag{2.106}$$

where K_R is a soil detachability factor for shear stress ($kg \;\; m \;\; N^{-1.5} s^{-1}$), τ_e is the average "effective" shear stress ($N \;\; m^{-2}$) and b_1 is an exponent in the range 1.0 to 2.0.

The rate of entrainment by rainfall D_F is (Lane and Shirley, 1985)

$$D_F = K_I P R, \quad (kg \;\; m^{-2} \;\; s^{-1}) \tag{2.107}$$

where K_I is soil detachability by rainfall impact ($kg\ \ s\ \ m^{-4}$), P is the rainfall rate ($m\ \ s^{-1}$) and R is the excess rainfall rate ($m\ \ s^{-1}$). The rate of deposition d is (Mehta, 1983)

$$d = \epsilon_0 \bar{c} v_s, \tag{2.108}$$

where ϵ_0 is a dimensionless coefficient depending on the soil and fluid properties and $\bar{c}$ is the local mean sediment concentration ($kg\ \ m^{-3}$).

The Hairsine-Rose (HR) model (Hairsine and Rose, 1991, 1992a,b; Rose *et al.*, 1983a) is a model for erosion by rainfall and sheet flow on a plane soil surface. The full 1D Hairsine-Rose model for soil erosion and sediment transport in a strip of unit width down a plane surface is conceptually described as in Fig. (2.11). When cohesive soil is eroded and transferred into suspension, it begins to deposit again due to gravity. The layer of deposited sediment has no cohesive strength and is therefore easier to erode than the original soil. Hence the HR model partitions the rainfall detachment and runoff entrainment erosion processes between the original soil and the deposited layer. Additionally the deposition rate of suspended sediment is size class dependent with larger particles depositing rapidly and smaller clay size particles remaining in suspension. Consequently the deposited layer will be dominated by larger sized particles. If the original soil is now split into I different size classes and c_i and m_i define the suspended sediment concentration and deposited mass per unit area of particles of size class i, then mass conservation for the HR model is given by (Hairsine *et al.*, 2002)

$$\frac{\partial (h c_i)}{\partial t} + \frac{\partial (q c_i)}{\partial x} = e_i + e_{di} + r_i + r_{ri} - d_i \quad i = 1, \ldots, I \tag{2.109}$$

and

$$\frac{\partial m_i}{\partial t} = d_i - e_{di} - r_{ri}, \qquad i = 1, \ldots, I \tag{2.110}$$

The right hand side of (2.109) and (2.110) are source terms (units of $kg\ \ m^{-2}\ \ s^{-1}$) including the rate of rainfall detachment (e_i), the rate of rainfall re-detachment (e_{di}), the rate of runoff entrainment (r_i), the rate of runoff re-entrainment (r_{ri}) and the rate of deposition (d_i).

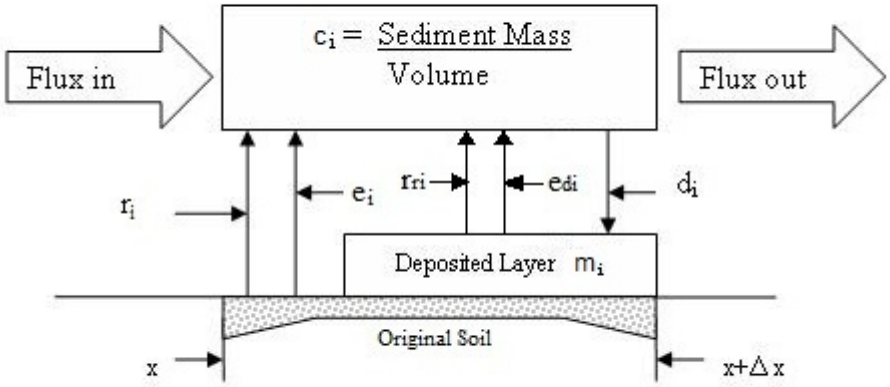

Figure 2.11: Flow diagram describing the interaction of erosion processes between the sediment flux, the original soil and the deposited layer (from Hairsine *et al.* (2002))

The 1D physical-based models, ANSWERS, LISEM, WEPP, EUROSEM, KINEROS, KINEROS2 and WESP focus mainly on watershed scale erosion and sediment transport, while USLE and HR model pay attention to erosion and sediment transport on the hillslope scale. AGNPS, ANSWERS (extended version by Rose and Ghadiri (1991)), WEPP and EUROSEM include the rill structure in their models while other models don't. Amongst these physically based models, ANSWERS, LISEM (latest version), KINEROS2 and HR models characterize sediment by different size class with respect to their settling velocities, i.e. they are multi-size class models. The other models choose a single-mean characteristic size class like D_{50} in EUROSEM as representative of the soil particle (a concise summary of these models is given in Table (2.1)). However, a single effective size class can't be representative of the behavior of eroded soil either in suspension or in deposited layer on soil surface as deposition is a size selective process. The sediment size distribution is also very important for determining contaminant fluxes as pollutants (both chemical and biological) are usually preferentially sorbed to finest particles (Aksoy and Kavvas, 2005). Therefore an understanding of the transport dynamics of the individual particles, as well as the overall total concentration, has significant implications on the understanding of the supply of non-point source pollutants to waterways (Sander *et al.*, 1996). The multi-size models such as ANSWERS and KINEROS2 were developed on the basis of a single unique transport capacity, however this has been experimentally shown to vary under net erosion and net deposition conditions for the same soil type, slope and flow rates by Polyakov and Nearing (2003) and theoretically in Sander *et al.* (2007a). Secondly, the transport capacity is difficult to determine for individual particle size class a priori.

Based on its advantages discussed above, we adopt the HR soil erosion and sediment transport model in this thesis. The next section presents some of the historical developments of the HR model and solutions obtained for various flow conditions.

Table 2.1: Erosion/sediment transport models

Model	Type	Scale	Flow	Size Class	Chemical Transport	Vegetation Modules
USLE	Empirical	Hillslope	Sheet	Single-size	No	No
AGNPS	Empirical	Small catchment	Sheet,rill, gully	Single-size	N, P, Chemical oxygen, organic carbon	No
ANSWERS	Physical	Small catchment	Sheet	Multi-size	Nutrients	Yes
WEPP	Physical	Hillslope/catchment	Sheet,rill	Single-size	No	Yes
EUROSEM	Physical	Field/small catchment	Sheet,rill	Single-size	No	No
LISEM	Physical	Small catchment	Sheet	Multi-size (up to 6 classes)	No	Yes
KINEROS	Physical	Small catchment	Sheet	Single-size	No	No
KINEROS2	Physical	Small catchment	Sheet	Multi-size (up to 5 classes)	No	No
WESP	Physical	Small catchment	Sheet	Single-size	No	No
Hairsine-Rose	Physical	Laboratory/small hillslope	Sheet	Multi-size (arbitrary classes)	No	No

2.2.2 Hairsine-Rose Model

This section introduces the development of the HR model since its first appearance in 1983. Rose *et al.* (1983a) introduced a new soil erosion modelling approach which formed the basis of the HR model. Three erosion processes were considered in their model: rainfall detachment, water flow entrainment and sediment deposition to the soil surface. They also assume that sediment is sorted conceptually into I classes with each class having an equal mass fraction of $1/I$, giving the model equations as

$$\frac{\partial(hc_i)}{\partial t} + \frac{\partial(qc_i)}{\partial x} = e_i + r_i - d_i, \tag{2.111}$$

and

$$m_t = WL \int_0^{t_R} c(L) R_1 dt, \tag{2.112}$$

where t_R is the duration of the runoff event and R_1 is the runoff rate per unit of plane area ($= q(L)/L$), m_t is the accumulated mass of sediment from a plane of width W and $c = \sum c_i$ is the total suspended sediment concentration.

The rate of detachment of the i^{th} class sediment e_i is taken as a non-size class selective process. It is defined proportional to a power of rainfall rate, $e_i = \frac{aC_dP^l}{I}$ where a is the detachability of soil by rainfall, C_d is the fraction of the soil surface exposed to rainfall, P is the rainfall rate and l is a non-dimensional exponent.

The rate of deposition of the i^{th} class sediment d_i depends on the settling or terminal velocity v_i and concentration of sediment in class i. It is given by $d_i = v_i c_i$.

The rate of entrainment of the i^{th} class sediment r_i is derived basing on the concept of net transport rate of bedload introduced in Bagnold (1977). It is given as

$$r_i = (\rho g S_0 B_0 R_1 C_r / I)(\gamma_i - \frac{v_i}{R_1}\frac{x_*}{x}) + \frac{\partial(hc_i)}{\partial t}, \quad (x \geq x_*) \tag{2.113}$$

where

$$B_0 = (\frac{\rho_s}{\rho_s - \rho})\frac{\eta}{0.6g}, \tag{2.114}$$

and η is the efficiency of entrainment; C_r is the fraction of the soil surface unprotected by mulch, stone, or other material; $x_* = \Omega_{cr}/(\rho g S R_1)$; Ω_{cr} is threshold stream power ($W \ \ m^{-2}$); S_0 is the slope of the plane; $\gamma_i = 1 + v_i/R_1$.

The steady state solution of (2.111) is obtained and given as

$$c_i = \frac{aC_d P^l}{\gamma_i R_1 I} + (\rho g S_0 B_0 C_r / I)(1 - x_*/x), \quad x \geq x_*. \tag{2.115}$$

The application of this model for a arid-zone catchment is presented in Rose *et al.* (1983b).

Hairsine and Rose (1991) basically extended the original model of Rose *et al.* (1983a) by accounting for the difference between eroding original cohesive soil as opposed to eroding deposited non-cohesive sediment. In this paper, it considered the case that soil erosion on the plane slope surface is driven solely by raindrops and that the shear stress between water flow and soil surface (or its resulting stream power) is assumed to be not big enough to cause entrainment and re-entrainment. The model equations of (2.109) and (2.110) therefore simplify to

$$\frac{\partial(hc_i)}{\partial t} + \frac{\partial(qc_i)}{\partial x} = e_i + e_{di} - d_i, \quad i = 1, 2, \ldots, I, \tag{2.116}$$

$$\frac{\partial m_i}{\partial t} = d_i - e_{di}. \tag{2.117}$$

This paper is the first to raise the concept of the coarser deposited sediments shielding a fraction H of the original soil and replaces C_d introduced in Rose *et al.* (1983a) with $(1 - H)$. Consequently the rate of detachment e_i is now given by

$$e_i = (1 - H)\frac{aP^l}{I}. \tag{2.118}$$

Since raindrop energy is reduced as it penetrates the surface water layer, the soil detachability a is actually a decreasing function of the water depth h. Proffitt *et al.* (1991) proposed the following functional relationship

$$a = a_0, \quad h \leq h_0; \tag{2.119}$$

$$a = a_0(\frac{h_0}{h})^b, \quad h > h_0, \tag{2.120}$$

where a_0 is maximum detachability at breakpoint depth h_0, which is about three drops diameters, and b is an exponent in the range of 0.66 ± 0.07.

Hairsine and Rose (1991) also proposed a slight modification to the deposition rate d_i as (Croley, 1982)

$$d_i = \alpha_i v_i c_i, \tag{2.121}$$

where α_i is the ratio of the concentration adjacent to the bed to the mean concentration over the entire depth. This can be taken as 1 in shallow flows, but if in rills and the water depth is $1 - 2cm$, $\alpha_i > 1$ (Hairsine, 1988).

The re-detachment of deposited layer is also a non-size class selective process and is proportional to the fraction of particles of that size in the layer. The rate of re-detachment e_{di} is then given by

$$e_{di} = H a_d P^l \frac{m_i}{m_t} \tag{2.122}$$

where $m_t = \sum_{i=1}^{I} m_i$ and therefore m_i/m_t is the fraction of particles of a given size class i in the layer. The detachability of deposited layer a_d is also a function of water depth and is given by a similar depth dependence as a, i.e.

$$a_d = a_{d0}, \quad h \leq h_0, \tag{2.123}$$

$$a_d = a_{d0}(\frac{h_0}{h})^b, \quad h > h_0. \tag{2.124}$$

in which a_{do} is maximum detachability of deposited soil at depth h_0.

A steady state analytical solution is presented in this paper for $\frac{\partial m_i}{\partial t} = \frac{\partial c_i}{\partial t} = 0$ and $q = Rx = Kh^m$. The solution is expressed by

$$\begin{aligned} c &= \frac{a_0 P^l}{\varepsilon R}, \quad h \leq h_0; \\ c &= \frac{a_0 P^l}{\varepsilon R}(\frac{q_0}{q})^\varepsilon - \frac{a_0 P^l}{R(\varepsilon - b/m)}[(\frac{q_0}{q})^{b/m} - (\frac{q_0}{q})^\varepsilon], \quad h > h_0; \end{aligned} \tag{2.125}$$

where q_0 is the water flux when $h = h_0$, $\varepsilon = 1 + \frac{a_0 \sum_{i=1}^{I} \alpha_i v_i}{IQa_d}$.

The expression for H is also given as

$$H = c\frac{\sum_{i=1}^{I} \alpha_i v_i}{a_d P^l I}. \tag{2.126}$$

As pointed out in Sander *et al.* (2007b), (2.125) shows c is a decreasing function of q with $c \to 0$ as $q \to \infty$. However as q increases, there will be a distance x downstream where q is large enough for entrainment processes to begin. Therefore, equation (2.125) only applies for $0 \leq q \leq q_{cr}$ where q_{cr} defined from the threshold stream power (which will be introduced) as $q_{cr} = \Omega_{cr}/\rho g S_0$. For $q > q_{cr}$, it is then necessary to consider flow driven erosion.

While Hairsine and Rose (1991) focused on rainfall-driven erosion, Hairsine and Rose (1992a,b) considered the case of flow-driven erosion. When $q > q_{cr}$ and there is a sufficient water depth (approximately three raindrop diameters (Proffitt *et al.*, 1991)) such that raindrop impact is negligible i.e. $e_i = e_{di} = 0$, entrainment and re-entrainment become the dominant erosive mechanisms. Consequently the three processes they considered in these papers are entrainment, deposition and re-entrainment of deposited sediment. The model equations then become

$$\frac{\partial (hc_i)}{\partial t} + \frac{\partial q c_i}{\partial x} = r_i + r_{ri} - d_i, \quad i = 1, 2, \ldots, I \tag{2.127}$$

and

$$\frac{\partial m_i}{\partial t} = d_i - r_{ri}. \tag{2.128}$$

To determine the rate of entrainment of sediment r_i, Hairsine and Rose (1992a) adopt the concept of "stream power" by Bagnold (1966). Stream power is the rate of working of the mutual shear stress between the soil surface and overland flow. It is the power per unit bed area available to do work and formulated as

$$\Omega = \rho g S_0 q. \tag{2.129}$$

Hairsine and Rose (1992a) assumed that Ω must be greater than the threshold stream power Ω_{cr} for entrainment to occur. Part of this excess stream power $(\Omega - \Omega_{cr})$ is dissipated as heat and noise, and another part of it is effective in entrainment and re-entrainment. Taking F as this fraction, then $F(\Omega - \Omega_{cr})$ is the effective excess stream power for entrainment and re-entrainment, $(1 - H)F(\Omega - \Omega_{cr})$ is the effective excess stream power for entrainment of original soil and

$HF(\Omega - \Omega_{cr})$ is the remaining effective excess stream power for re-entrainment of deposited sediment.

The original soil cohesive matrix has a resistance to its removal by fluid stresses. Defining J as the specific energy per unit mass of soil required to entrain it and assuming that entrainment is a non-size class selective process, then the total rate of entrainment is Ir_i, and the total rate of energy required for entrainment is Ir_iJ. Since this must be equal to the effective excess stream power available for entrainment, i.e.

$$Ir_iJ = (1 - H)F(\Omega - \Omega_{cr}), \tag{2.130}$$

then (2.130) can be rearranged for r_i as

$$r_i = (1 - H)\frac{F}{IJ}(\Omega - \Omega_{cr}). \tag{2.131}$$

The re-entrainment process is similar with that of entrainment, but the cohesive strength of the deposition layer is assumed to be insignificant. Therefore, the stream power expended in this process is solely active in changing the potential energy of the sediment which is lifted from the bed to a height h in the flow. The immersed weight of the soil is proportional to $\frac{\rho_s - \rho}{\rho_s}$ and the height that the sediment is lifted to is expressed as $\frac{h}{\alpha_i}$ where α_i is defined as in (2.121). If we defined the rate of re-entrainment as r_{ri}, then the rate of change in potential energy of i size class sediment is $r_{ri}g(\frac{h}{\alpha_i})\frac{\rho_s - \rho}{\rho_s}$. As noted previously the effective excess stream power available for re-entrainment is $HF(\Omega - \Omega_{cr})$. As re-entrainment is a non-selective process with respect to sediment size of deposition layer like entrainment of the original soil, the effective excess stream power available for an individual class is proportional to the mass fraction of the class in the deposited layer $\frac{m_i}{m_t}$. Thus, the effective excess stream power must be equal to the rate of potential change of sediment of each size class. i.e.

$$r_{ri}g(\frac{h}{\alpha_i})\frac{\rho_s - \rho}{\rho_s} = HF(\Omega - \Omega_{cr})\frac{m_i}{m_t}, \tag{2.132}$$

and therefore

$$r_{ri} = \frac{\alpha_i HF}{g}\frac{\rho_s}{\rho_s - \rho}(\frac{\Omega - \Omega_{cr}}{h})\frac{m_i}{m_t}. \tag{2.133}$$

Steady state analytical solutions are presented in the paper for the case $H < 1$ and $H = 1$. For the case of $H < 1$, it is noted by Sander *et al.* (2007c) that solution contained an error and a correction was therefore given.

For $H < 1$, the correct solution is ($c_i = c/I$),

$$\begin{aligned} c &= \frac{A_1}{\lambda}\xi^{m-1}[1 - \frac{2m-1}{m\lambda\xi} + \frac{(2m-1)(2m-2)}{(m\lambda\xi)^2} + \cdots \\ &+\frac{(-1)^{j_1}(2m-1)(2m-2)(2m-3)..(2m-j_1)}{(m\lambda\xi)^{j_1}}] - \frac{A_2}{\lambda\xi}[1 - \frac{m-1}{m\lambda\xi} \\ &+\frac{(m-1)(m-2)}{(m\lambda\xi)^2} + \ldots + \frac{(-1)^{j_2}(m-1)(m-2)(m-3)..(m-j_2)}{(m\lambda\xi)^{j_2}}] \\ &+\frac{\xi_{cr}^{m-1}e^{-m\lambda(\xi-\xi_{cr})}}{\lambda\xi^m}\{A_2[1 - \frac{m-1}{m\lambda\xi_{cr}} + \frac{(m-1)(m-2)}{(m\lambda\xi_{cr})^2} + \ldots \\ &+\frac{(-1)^{j_2}(m-1)(m-2)(m-3)..(m-j_2)}{(m\lambda\xi_{cr})^{j_2}}] - A_1\xi_{cr}^m[1 - \frac{2m-1}{m\lambda\xi_{cr}} \\ &+\frac{(2m-1)(2m-2)}{(m\lambda\xi_{cr})^2} + \cdots + \frac{(-1)^{j_1}(2m-1)(2m-2)(2m-3)..(2m-j_1)}{(m\lambda\xi_{cr})^{j_1}}]\} \end{aligned} \tag{2.134}$$

where the summation terms continue until $j_1 = 2m - 1$ and $j_2 = m - 1$, $\xi = q^{1/m} = (Rx)^{1/m}$, $\xi_{cr} = q_{cr}^{1/m}$ and

$$\lambda = \frac{g}{RJK^{1/m}I}\frac{\rho_s - \rho}{\rho_s}\Sigma_{i=1}^{I} v_i, \tag{2.135}$$

$$A_1 = \frac{F\rho g S_0}{RJ}, \quad A_2 = \frac{F\Omega_{cr}}{RJ}. \tag{2.136}$$

When m is a non-integer, c can be rewritten in terms of incomplete gamma functions (Sander *et al.*, 2007c)

$$\begin{aligned} c\xi^m e^{m\lambda\xi} &= \frac{mA_1}{(-1)^{2m}m^{2m}\lambda^{2m}}[\Gamma(2m, -m\lambda\xi_{cr}) - \Gamma(2m, -m\lambda\xi)] \\ &+\frac{mA_2}{(-1)^m m^m \lambda^m}[\Gamma(m, -m\lambda\xi) - \Gamma(m, -m\lambda\xi_{cr})], \end{aligned} \tag{2.137}$$

with H given by

$$H = \frac{cgh(\rho_s - \rho)\sum_{i=1}^{I} v_i}{\rho_s F(\Omega - \Omega_{cr})I}. \tag{2.138}$$

For $H = 1$, the solution is

$$c = \frac{F[\rho_s(\rho_s - \rho)](\Omega - \Omega_{cr})}{gh \sum_{i=1}^{I} v_i / I}. \tag{2.139}$$

Hairsine and Rose (1992b) extended the soil erosion model developed in Hairsine and Rose (1992a) by considering rill flow. The model is based on the assumption that the plane surface is composed of N rills per unit width with all rills being parallel down slope and incised in a homogeneous soil mass. Different from the previously mentioned models like WEPP and EUROSEM, the Hairsine and Rose (1992b) model is to simulate erosion in an individual rill instead of rill networks.

Sander *et al.* (1996) provided the first time-dependent solutions to Hairsine and Rose (1991) model when $r_i = r_{ri} = 0$. Unsteady solutions of (2.116) and (2.117) require an additional equation which describes the evolution of H as a function of the change of mass in the deposited layer. They assumed that this function could be approximated by the linear relation

$$H = \min(\frac{m_t}{m_t^*}, 1) \tag{2.140}$$

where m_t^* is the mass per unit area of sediment required for complete effective shielding.

An approximate analytical solution is obtained at $x = L$ (the end of slope) by assuming that changes in time dominant any spatial gradients, and therefore neglect the spatial derivative term in (2.116). The solution is applied to the experiments in Proffitt *et al.* (1991) and very good agreement is found against measured discharge concentrations for a wide range of experimental conditions.

Hairsine *et al.* (1999) is a companion paper to Sander *et al.* (1996) and considered the same flow and erosion conditions. Equations (2.116) and (2.117) are integrated over the duration of the erosion event and the length of the flow domain. They used this formulation to explain the formation of a deposited layer on the soil surface which results in sediment sorting on the hillslope and interpreted the experimentally observed trends that sediment leaving an area of soil being

eroded by raindrop impact is finer than the original soil (Alberts *et al.*, 1980, 1983; Meyer *et al.*, 1975).

In Hairsine *et al.* (2002), the HR model is used to describe steady state sediment flows across "net deposition" zones. In reality, these zones occur when sediment-laden overland flow passes across an area of reducing surface slope like foot slopes (Fig. (2.12) case 1) or increased hydraulic roughness like buffer zones (such as vegetation filter Fig. (2.12) case 2). In this case the deposited layer develops very rapidly to completely shield the original soil. As the deposited layer is assumed to offer no resistance to the eroding process, the sediment concentration is expected to be a maximum under net deposition conditions (Hairsine and Rose, 1992a). The importance of flow within these zones is due to the impact they have on the sorting of the transported sediment and the resulting enrichment of sediment-sorbed pollutant fluxes.

The model equations considered in Hairsine *et al.* (2002) were

$$\frac{d(qc)}{dx} = e_{di} + r_{ri} - d_i, \tag{2.141}$$

$$\frac{\partial m_i}{\partial t} = d_i - e_{di} - r_{ri}. \tag{2.142}$$

In this paper, it assumes that the deposited layer will not actually achieve steady state in such flows due to the continuous deposition of sediment even though the suspended sediment concentration does become steady. Hence (2.142) still contains the time derivative $\frac{\partial m_i}{\partial t}$. With the assumption that the water flow is deep enough to neglect the re-detachment by rainfall, Hairsine *et al.* (2002) presented solutions for (2.141) and (2.142) for two special cases.

When rainfall re-detachment and overland flow re-entrainment are both assumed to be negligible and for $q = q_0 + Rx$, the multiclass solution for (2.141) and (2.142) is

$$c_i = c_{i0}(\frac{q_0}{q})^{1+\alpha_i v_i/R} \tag{2.143}$$

where c_{i0} is the boundary values of c_i and q_0 is the value of q at $x = 0$.

Figure 2.12: Areas of net deposition (from www.google.com)

When the distribution of sediment sizes is characterized by a single representative settling velocity and re-entrainment is assumed to be active, the steady state solution for (2.141) and (2.142) is (for $q = q_0$)

$$c = c_0 exp(\frac{-\alpha v x}{q_0}) + \frac{\gamma_0 q_0^{1-\frac{1}{m}}}{\alpha v}(1 - \frac{q_{cr}}{q_0})[1 - exp(\frac{-\alpha v x}{q_0})]. \tag{2.144}$$

For q again varying with x, i.e. $q = q_0 + Rx$ then,

$$c(x) = c_0(\frac{q_0}{q})^{\varepsilon} + \frac{\gamma_0 q_0^{1-\frac{1}{m}}}{R(\varepsilon + 1 - \frac{1}{m})}[(\frac{q_0}{q})^{\frac{1}{m}-1} - \frac{q_0}{q})^{\varepsilon}] - \frac{\gamma_0 q_0^{\frac{-1}{m}} q_{cr}}{R(\varepsilon - \frac{1}{m})}[(\frac{q_0}{q})^{\frac{1}{m}} - (\frac{q_0}{q})^{\varepsilon}] \tag{2.145}$$

where $\varepsilon = 1 + \frac{(\alpha v)}{R}$ and

$$\gamma_0 = \frac{\alpha F \rho_s \rho S_0 K^{\frac{1}{m}}}{\rho_s - \rho}. \tag{2.146}$$

The solution was evaluated by using the experimental data in Beuselinck *et al.* (1999) with good agreement found.

Sander *et al.* (2002) considered the same HR model equations as in Hairsine *et al.* (2002). The re-entrainment and deposition are assumed to be the only active erosion mechanisms. They extended the steady state single-class analytical solution in Hairsine *et al.* (2002) to a steady state multi-class analytical solutions when $q = q_0 =$ constant. Their solution is presented as

$$c_i(x) = c_{i0}\big[\frac{c_I(x)}{c_{I0}}\big]^{v_i/v_I}, \quad i = 1, 2, \ldots, I-1 \tag{2.147}$$

$$\int_{c_I(0)}^{c_I} \left[\frac{\gamma^*}{\sum_{i=1}^{I} v_i c_{i0}[\overline{c}_I/c_{I0}]^{v_i/v_I}} - 1\right]^{-1} \frac{d\overline{c}_I}{\overline{c}_I} = \frac{v_I}{q}x \tag{2.148}$$

$$m_i(x,t) = v_i c_i \left[1 - \gamma^*/\Sigma_{i=1}^{I} v_i c_i\right] t, \quad i = 1, 2, \ldots, I \tag{2.149}$$

where $\gamma^* = \gamma q_0^{1-1m}\big[1 - \frac{q_{cr}}{q_0}\big]$. Excellent agreement across all size classes was found with their solution when applied to the experimental data of Beuselinck (1999). Also numerical solutions are discussed for q varying with x when $R < 0$ and $R > 0$.

Beuselinck *et al.* (2002) gave a multi-class solution to (2.141) and (2.142) with the re-entrainment and rainfall re-detachment mechanisms all active and q constant. The solution has the same form as expressed in (2.147) to (2.149) but γ^* is formulated as

$$\gamma^* = \gamma q_0^{1-1/m}\big(1 - \frac{q_{cr}}{q_0}\big) + a_{d0} P \big(\frac{h}{h_0}\big)^b. \tag{2.150}$$

Sander *et al.* (2007a) applied the HR model to the steady state experimental results of Polyakov and Nearing (2003). A new analytical solution is presented for net erosion ($H < 1$) which allowed for arbitrary mass proportions p_i of sediment

in each size class. Note that $\sum p_i = 1$. The net erosion solution is given as (q constant)

$$c_i = p_i \frac{\gamma}{\sum_{i=1}^{I} p_i v_i}[1 - exp(-\frac{\lambda \sum_{i=1}^{I} p_i v_i}{\gamma q} x)], \tag{2.151}$$

and

$$m_i = \frac{v_i c_i m_t^*}{\gamma}. \tag{2.152}$$

The net deposition solution is given as (2.147) to (2.149).

Not only were they able to predict the total suspended sediment concentration under both net erosion and net deposition flow conditions, but they were also able to predict the size class distributions of the eroded sediment for both flow conditions. Furthermore they showed that the transport capacity cannot be unique for a soil composed of a range of size classes and that uniqueness only occurs for a truly single size class soil. Due to its lack of uniqueness for a given soil type, it is clear that the transport capacity concept is deficient in modeling sediment transport of real soils under different flow conditions.

2.3 Conclusions

From the solutions of kinematic flow equation presented in the literature, it is notable that all of them were developed under zero depth boundary and initial conditions. The non-zero boundary and initial conditions, or unequal boundary and initial conditions have to my knowledge never been previously presented. Especially, the solution of the kinematic flow equation where R is time-dependent and $R(t) > 0$, $0 < t < t^*$ and $R(t) < 0$, $t > t^*$, is a much more complicated case under different boundary and initial conditions because of the expansion and shock waves which appear in the solution. When $t > t_2$ (defined in (2.79)), the single continuous water flow profile splits into such that two drying fronts arise with one moving towards the upstream boundary and another one moving downstream. These solutions provide a demanding test of the accuracy of any numerical solution for the kinematic flow equation through capturing the expansion

wave and the correct position and the height of the shock wave. The different boundary and initial conditions used for obtaining solutions for the kinematic flow equation could be applied in a laboratory flume to provide a wider range of hydraulic flow conditions and to test the HR model's ability to match the data from the erosion experiments. Therefore, one of the aims of this research is to develop new analytical solutions for kinematic flow equation for different combinations of boundary and initial conditions and also for different types of time dependent behaviors in the excess rainfall rate.

The HR model is quite different to previously developed soil erosion models. Then differences lie in that (i) it models the erosion and transport of a distribution of particle sizes; not a single size class (ii) it models the development of a covering layer of deposited particles on the soil surface that has different erosive properties to the original soil and (iii) it models the processes of erosion, entrainment, and gravity deposition separately and therefore does not require the use of a transport capacity concept. While there are many analytical steady state solutions of the HR model, only a few approximate time dependent solutions have been developed. In general the full model requires numerical methods to compute suspended sediment concentration. Such solution will then provide a better understanding of the transport dynamics of sediment distributions and the growth of net deposition zones and their influences on sediment transport processes.

CHAPTER 3

Analytical Solutions to the Kinematic Wave Equation

In general, there are no exact analytical solutions available to the 2D kinematic wave equation (2.56). However many solutions have been found for 1D kinematic flow (3.1), and these were discussed in the literature review in 2.1.4. In this chapter, new solutions to (3.1) will be developed for a range of boundary and initial conditions and different types of behaviour in the excess rainfall rate. Since (3.1) is a fist order hyperbolic partial differential equation, these new solutions will be obtained by using the method of characteristics.

When the flow is occurring on a surface of constant slope, the 1D kinematic wave flow equation can be written as

$$\frac{\partial h}{\partial t} + mKh^{m-1}\frac{\partial h}{\partial x} = R(x,t). \tag{3.1}$$

Solutions are sought for the following the initial and boundary conditions

$$h = h_i, \quad t = 0, \quad x > 0, \tag{3.2}$$

$$h = h_s, \quad x = 0, \quad t > 0. \tag{3.3}$$

Two types of behaviour in the excess rainfall rate R are considered, being R

constant and R varying with t. In each of these two cases, three combinations of boundary and initial condition are considered, $h_s = h_i$, $h_s < h_i$ and $h_s > h_i$.

3.1 R Constant

3.1.1 $h_s = h_i = h_b$

According to the method of characteristics, (3.1) can be written as

$$\frac{dt}{1} = \frac{dx}{mKh^{m-1}} = \frac{dh}{R}, \tag{3.4}$$

which can be replaced with following two ordinary differential equations

$$dh = Rdt, \tag{3.5}$$

and

$$dx = mKh^{m-1}dt. \tag{3.6}$$

Integrating (3.5) using $h = h_b$ at $t = 0$ gives

$$h = Rt + h_b \tag{3.7}$$

and integrating (3.6) with $x = 0$ and $t = t_0 = 0$, we have

$$x = \int_0^t mKh^{m-1}dt. \tag{3.8}$$

Substituting (3.7) into (3.8), it gives the characteristic curve

$$x = \frac{K}{R}\left[(Rt + h_b)^m - h_b^m\right], \tag{3.9}$$

As presented in Fig. (3.1), (3.9) is the characteristic curve emanating from the origin which divides the $x - t$ plane into two regions A and B.

In Fig. (3.1), t_0 parameterizes the characteristics emanating from the t axis while x_0 parameterizes the characteristics emanating from the x axis. The characteristic curves located in region A can be calculated by integrating (3.6) subject to $t = 0$, $x = x_0$ to give

$$x = \int_0^t mKh^{m-1}dt + x_0. \tag{3.10}$$

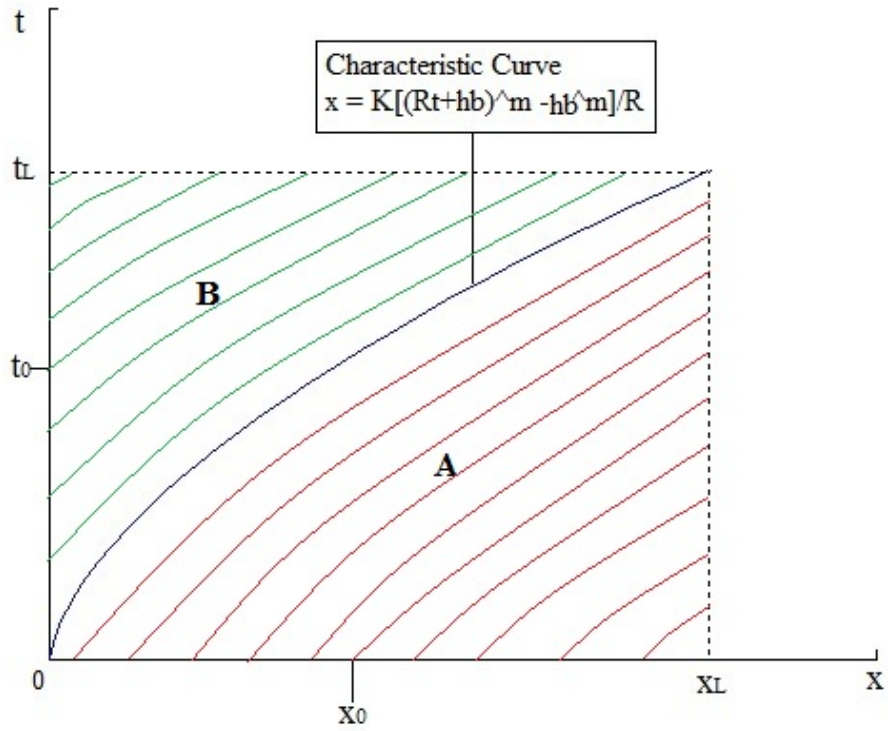

Figure 3.1: Characteristic curve of kinematic wave equation (3.1) when $h_i = h_s = h_b$

Substituting from (3.7) into (3.10) results in

$$\begin{aligned} x &= \int_0^t mK(Rt + h_b)^{m-1} dt + x_0 \\ &= \frac{K}{R}[(Rt + h_b)^m - h_b^m] + x_0. \end{aligned} \tag{3.11}$$

Thus, in regime A in which $x \geq \frac{K}{R}\left[(Rt + h_b)^m - h_b^m\right]$, h is only dependent on t and given by $h = Rt + h_b$.

The characteristic curves in region B can be found by integrating (3.6) subject to $x = 0$, $t = t_0$ to obtain

$$x = \int_{t_0}^t mKh^{m-1} dt \tag{3.12}$$

Integrating (3.5) with $t = t_0$, $h = h_b$ gives

$$h = R(t - t_0) + h_b \tag{3.13}$$

which combined with (3.12) results in

$$\begin{aligned} x &= \int_{t_0}^{t} mK[R(t - t_0) + h_b]^{m-1} dt \\ &= \frac{K}{R}(h^m - h_b^m). \end{aligned} \tag{3.14}$$

Thus, in region B where $x \leq \frac{K}{R}\left[(Rt + h_b)^m - h_b^m\right]$, h is only dependent on x and given by $h = (\frac{Rx}{K} + h_b^m)^{1/m}$.

The full solution to (3.1) subject to (3.2) and (3.3) with $h_s = h_i = h_b$ is

$$h = \left(\frac{Rx}{K} + h_b^m\right)^{\frac{1}{m}} \qquad x \leq \frac{K}{R}\left[(Rt + h_b)^m - h_b^m\right], \tag{3.15}$$

$$h = Rt + h_b \qquad x \geq \frac{K}{R}\left[(Rt + h_b)^m - h_b^m\right]. \tag{3.16}$$

which is consistent with the solution given in Henderson and Wooding (1964) when $h_b = 0$. Fig. (3.2) gives the plot of h as a function of x at times $t = 3, 15, 30, 45, 120 \ \ s$ when $h_b = 0.5mm$. $R = 100 \ \ mm \ \ hr^{-1}$, $m = 5/3$, $S_0 = 0.004$, $n = 0.02 \ min \ \ m^{1/3}$ and $K = \sqrt{S_0}/n$.

3.1.2 $h_s \neq h_i$

As the boundary and initial conditions have different values, the characteristic curves that emanate from the origin of $x - t$ plane will have different gradients. Considering the first characteristic coming off the x axis, we integrate (3.5) subject to (3.2) to obtain

$$h = Rt + h_i. \tag{3.17}$$

Combing (3.17) with (3.6) and integrating (3.6) with the condition $h = h_i$, $x = x_0$ results in the characteristic equation

$$x = \frac{K}{R}\left[h^m - h_i^m\right] + x_0. \tag{3.18}$$

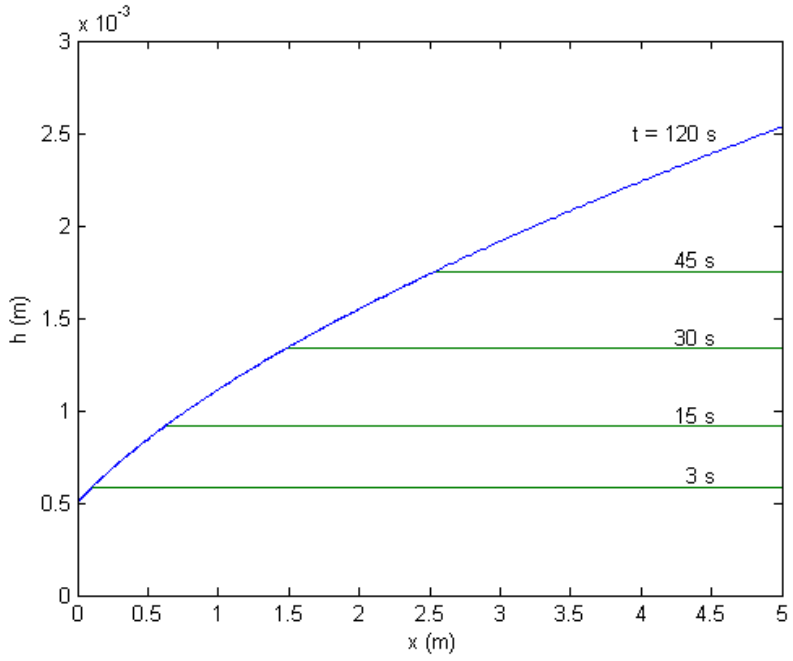

Figure 3.2: Plot of h as a function of x down the plane at times $t = 3, 15, 30, 45,$ 120 s and $h_s = h_i = h_b = 0.5$ mm.

To obtain the equation for the characteristic coming of the t axis, (3.5) is first integrated subject to $t = t_0$, $h = h_s$ to find

$$h = R(t - t_0) + h_s. \tag{3.19}$$

Again combining (3.19) with (3.6) and using the boundary condition (3.3) gives

$$\begin{aligned} x &= \frac{K}{R}\left[R(t - t_0) + h_s\right]^m - \frac{K}{R}h_s^m \\ &= \frac{K}{R}h^m - \frac{K}{R}h_s^m. \end{aligned} \tag{3.20}$$

Note that if we take $x_0 \to 0$ in (3.18) and $t_0 \to 0$ in (3.20), they don't converge to the same equation since $h_i \neq h_s$. Thus, we say there are two series of characteristic curves with different gradients in $x - t$ plane. They create either fan-like characteristics or intersecting characteristics, which will lead to either

the development of an expansion wave or a shock wave depending on $h_s < h_i$ or $h_s > h_i$ respectively.

3.1.2.1 $h_s < h_i$

As presented in Fig. (3.3), for $h_s < h_i$, (3.1) has a region of fan-like characteristic curves which is bounded by the two curves $x = \frac{K}{R}\left[(Rt + h_i)^m - h_i^m\right]$ and $x = \frac{K}{R}\left[(Rt + h_s)^m - h_s^m\right]$. These divide the $x - t$ plane into three regions A, B, C.

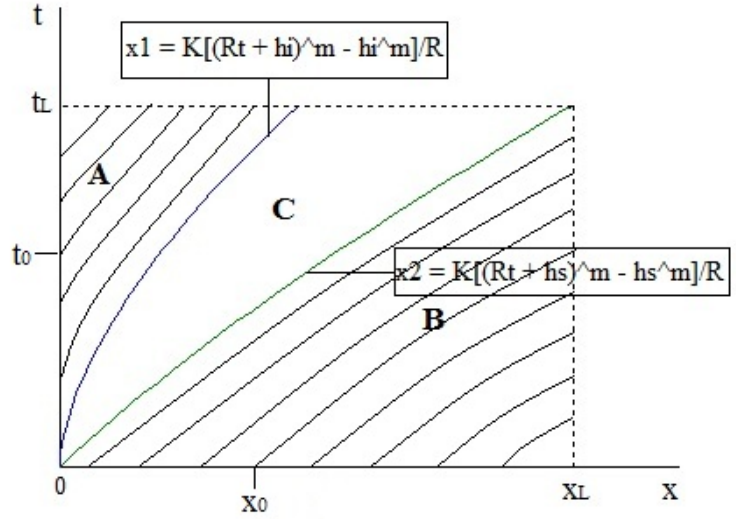

Figure 3.3: Characteristics of kinematic wave equation (3.1) when $h_s < h_i$

In region A, we have the solution (from (3.20) and (3.20)) of

$$h = (\frac{R}{K}x + h_s^m)^{1/m}, \tag{3.21}$$

$$x = \frac{K}{R}[R(t - t_0) + h_s]^m - \frac{K}{R}h_s^m; \tag{3.22}$$

in which h is a function of x only.

In region B, the solution is given by

$$h = Rt + h_i, \tag{3.23}$$

$$x = \frac{K}{R}\left[(Rt + h_i)^m - h_i^m\right] + x_0 \tag{3.24}$$

in which h is only time dependent.

In region C, the solution for h is both x and t dependent and is given in the following two equations

$$x = \frac{K}{R}\left[(Rt + h_c)^m - h_c^m\right], \tag{3.25}$$

$$h = h_c + Rt \tag{3.26}$$

where h_c is a parameter that varies in the range $h_s \leq h_c \leq h_i$. Note that $h_c = h_s$ recovers the boundary condition of (3.22) with $t_0 = 0$, while $h_c = h_i$ captures the other bounding solution given by (3.24) with $x_0 = 0$.

Therefore, for $h_s < h_i$, the full solution for kinematic wave equation (3.1) is

$$h = (\frac{Rx}{K} + h_s^m)^{1/m}, \qquad x < x_a, \tag{3.27}$$

$$h = Rt + h_i, \qquad x > x_b, \tag{3.28}$$

$$x = \frac{K}{R}[h^m - h_c^m], \qquad x_a \leq x \leq x_b, \tag{3.29}$$

where $x_a = \frac{K}{R}[(Rt + h_s)^m - h_s^m]$ and $x_b = \frac{K}{R}[(Rt + h_i)^m - h_i^m]$.

Fig. (3.4) gives h as a function of x down the plane at times $t = 3, 15, 30, 45, 120\ \ s$ when we take $h_s = 1\ \ mm$ and $h_i = 2\ \ mm$. The parameters used are the same as for $h_s = h_i = h_b$.

3.1.2.2 $h_s > h_i$

When $h_s > h_i$, Fig. (3.5) shows that region C is where the characteristics coming from either axis now intersect, resulting in multi-valued solutions. The problem of multi-valued solutions is resolved by introducing a discontinuous solution or shock wave. The equation which governs the evolution of the shock position x_s is given by Rankine-Hugonoit condition (Haberman, 1997)

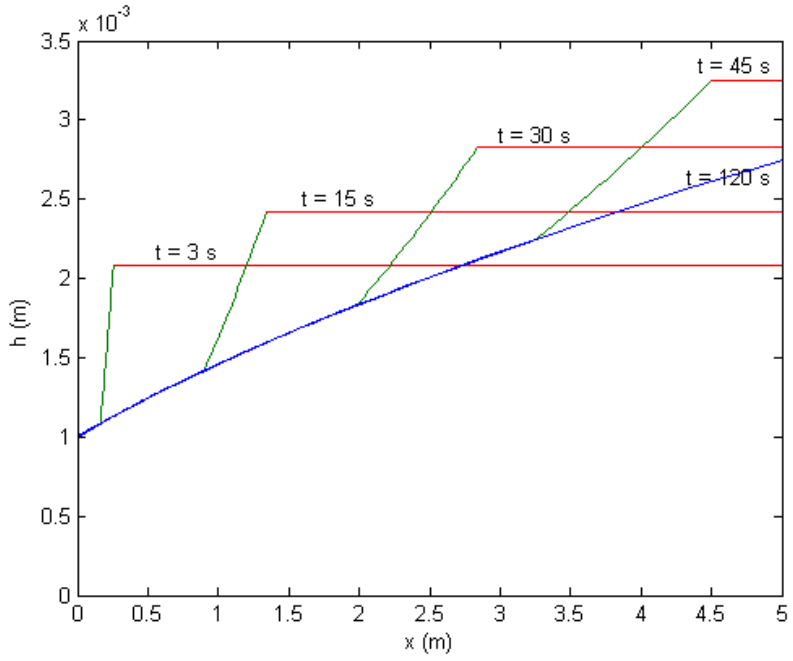

Figure 3.4: Plot of h as a function of x down the plane at times $t = 3, 15, 30, 45,$ $120 \;\; s$ and $h_s = 1 \;\; mm$ and $h_i = 2 \;\; mm$.

$$\begin{aligned} \frac{dx_s}{dt} &= \frac{q(x_s^+,t) - q(x_s^-,t)}{h(x_s^+,t) - h(x_s^-,t)} \\ &= \frac{K(h(x_s^+,t))^m - K(h(x_s^-,t))^m}{h(x_s^+,t) - h(x_s^-,t)}, \end{aligned} \tag{3.30}$$

where $h(x_s^+,t) = Rt + h_i$, $h(x_s^-,t) = (\frac{Rx_s}{K} + h_s^m)^{1/m}$ are the heights on either side of shock.

Equation (3.30) can be solved numerically to obtain x_s. Thus the solution can be expressed as

$$h = (h_s^m + \frac{Rx}{K})^{1/m}, \quad x \le x_s, \tag{3.31}$$

$$h = Rt + h_i \quad x \ge x_s. \tag{3.32}$$

Fig. (3.6) gives h as a function of x down the plane at times $t = 3, 15, 30, 45, 120 \;\; s$

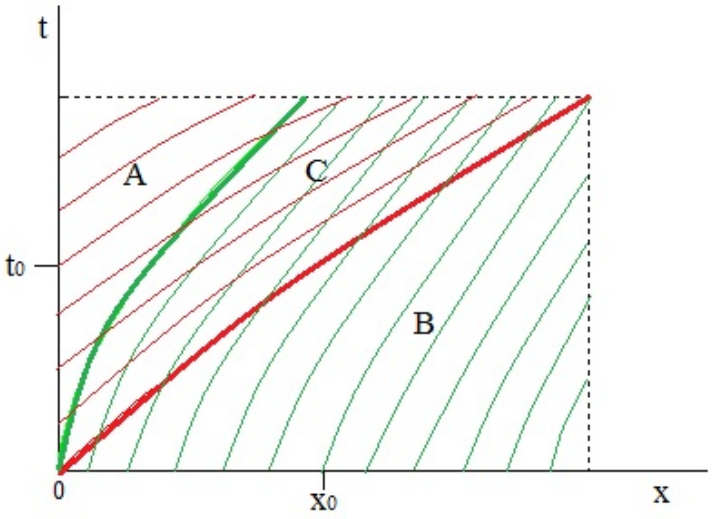

Figure 3.5: Intersecting characteristics of kinematic wave equation (3.1) when $h_s > h_i$

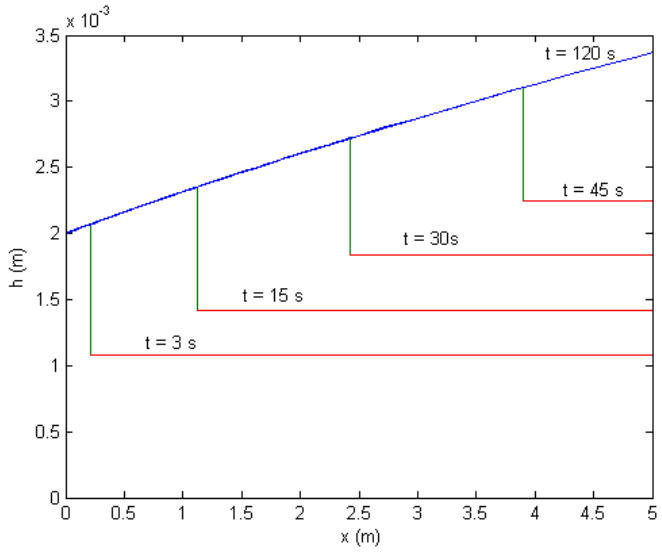

Figure 3.6: Plot of h as a function of x down the plane at times $t = 3, 15, 30, 45,$ 120 s and $h_s = 2$ mm and $h_i = 1$ mm

when we take $h_s = 2 \ \ mm$, $h_i = 1 \ \ mm$. The parameters used are the same as for the two previous cases.

3.2 R Dependent on t

In this section, the case where R is a function of t is considered and as previously it is assumed that spatial variation in R can be ignored. As in the presentation of the case when R is constant, (3.1) is solved under different boundary and initial conditions, $h_s = h_i$, $h_s < h_i$ and $h_s > h_i$.

3.2.1 $R(t) \geq 0$ for $t \geq 0$

3.2.1.1 $h_s = h_i = h_b$

Parlange *et al.* (1981) has given the analytical solution for (3.1) when $h_b = 0$ as

$$h = \int_{t_0}^{t} R(t^{'})dt^{'}, \quad x = Km \int_{t_0}^{t} [\int_{t_0}^{\bar{t}} R(t^{'})dt^{'}]^{m-1} d\bar{t}, \quad x \leq x_c, \tag{3.33}$$

$$h = \int_{0}^{t} R(t^{'})dt^{'}, x = Km \int_{0}^{t} [\int_{0}^{\bar{t}} R(t^{'})dt^{'}]^{m-1} d\bar{t} + x_0, \quad x \geq x_c. \tag{3.34}$$

where $x_c = Km \int_0^t [\int_0^{\bar{t}} R(t^{'})dt^{'}]^{m-1} d\bar{t}$ and $0 \leq t_0 \leq t$.

This solution can be easily generalized for the case when the boundary and initial condition are non-zero ($h_b \neq 0$) as

$$h = \int_{t_0}^{t} R(t^{'})dt^{'} + h_b, \quad x = mK \int_{t_0}^{t} h^{m-1} d\bar{t}, \quad x \leq x_c^{'} \tag{3.35}$$

$$h = \int_{0}^{t} R(t^{'})dt^{'} + h_b, \quad x = mK \int_{0}^{t} h^{m-1} d\bar{t} + x_0, \quad x \geq x_c^{'}. \tag{3.36}$$

where $x_c^{'} = mK \int_0^t [\int_0^{\bar{t}} R(t^{'})dt^{'} + h_b]^{m-1} d\bar{t}$ and $0 \leq t_0 \leq t$.

Parlange *et al.* (1981) applied their solution for a single peak excess rainfall function

$$R(t) = R_0 e^{-t/\tau}(1 - e^{-t/\tau}) \quad for \quad t > 0 \tag{3.37}$$

where R_0 and τ are arbitrary constants which control the height and timing of the peak.

The solution of (3.35) and (3.36) can then be written as,

for $x \leq x_c^{'}$,

$$\frac{h}{R_0\tau} = e^{-t_0/\tau} - e^{-t/\tau} - \frac{1}{2}e^{-2t_0/\tau} + \frac{1}{2}e^{-2t/\tau} + \frac{h_b}{R_0\tau} \tag{3.38}$$

$$x = \frac{5}{3}KR_0^{2/3}\tau^{5/3}\int_{t_0/\tau}^{t/\tau}(e^{-t_0/\tau} - e^{-t^{'}} - \frac{1}{2}e^{-2t_0/\tau} + \frac{1}{2}e^{-2t^{'}} + \frac{h_b}{R_o\tau})^{2/3}dt^{'} \tag{3.39}$$

for $x \geq x_c^{'}$,

$$\frac{h}{R_0\tau} = \frac{1}{2} - e^{-t/\tau} + \frac{1}{2}e^{-2t/\tau} + \frac{h_b}{R_0\tau} \tag{3.40}$$

$$x = \frac{5}{3}KR_0^{2/3}\tau^{5/3}\int_{0}^{t/\tau}(\frac{1}{2} - e^{-t^{'}} + \frac{1}{2}e^{-2t^{'}} + \frac{h_b}{R_0\tau})^{2/3}dt^{'} + x_0 \tag{3.41}$$

where $x_c^{'} = \frac{5}{3}KR_0^{2/3}\tau^{5/3}\int_0^{t/\tau}(\frac{1}{2} - e^{-t^{'}} + \frac{1}{2}e^{-2t^{'}} + \frac{h_b}{R_0\tau})^{2/3}dt^{'}$ and $0 \leq t_0 \leq t$.

Fig. (3.7) gives the normalized height $\frac{h}{R_0\tau}$ as a function of the fractional distance down the plane x/L for various reduced times t/τ where L was chosen as the value of x when $t = 3t_m$ and $t_0 = 0$ in equation (3.39), $t_m = ln2$ is the value of t when $R(t)$ is maximum.

3.2.1.2 $h_s < h_i$

As for the case of R constant, when R is varying with t and $h_s < h_i$, the solution can be divided into three regions with the central region again resulting in an expansion fan.

For $x < mK\int_0^t[\int_0^{\bar{t}} R(t^{'})dt^{'} + h_s]^{m-1}d\bar{t}$, the solution is

$$h = \int_{t_0}^{t} Rdt^{'} + h_s, \tag{3.42}$$

$$x = mK\int_{t_0}^{t}[\int_{t_0}^{\bar{t}} R(t^{'})dt^{'} + h_s]^{m-1}d\bar{t}. \tag{3.43}$$

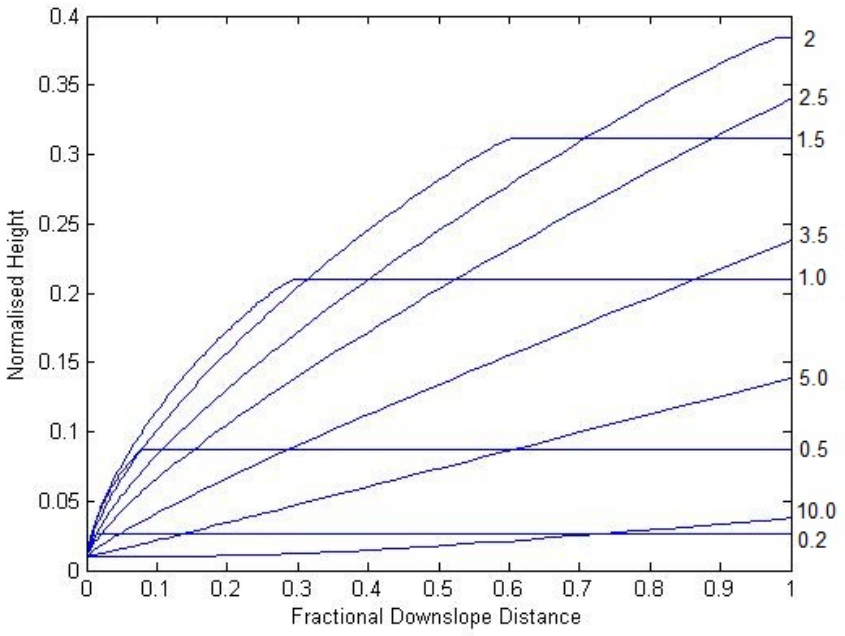

Figure 3.7: Plot of the normalized height $h/R_0\tau$ as a function of the fractional distance down the plane x/L for reduced times t/τ = 0.2, 0.5, 1, 1.5, 2.0, 2.5, 3.5, 5.0, 10.0 and $h_b/R_0\tau = 0.01$.

For $x > mK\int_0^t[\int_0^{\bar{t}} R(t')dt' + h_i]^{m-1}d\bar{t}$, the solution is

$$h = \int_0^t Rdt' + h_i, \tag{3.44}$$

$$x = mK\int_0^t[\int_0^{\bar{t}} R(t')dt' + h_i]^{m-1}d\bar{t} + x_0. \tag{3.45}$$

For the region $mK\int_0^t[\int_0^{\bar{t}} R(t')dt' + h_s]^{m-1}d\bar{t} \leq x \leq Km\int_0^t[\int_0^{\bar{t}} R(t')dt' + h_i]^{m-1}d\bar{t}$, the solution is

$$h = \int_0^t Rdt' + h_c, \tag{3.46}$$

$$x = mK\int_0^t[\int_0^{\bar{t}} R(t')dt' + h_c]^{m-1}d\bar{t} \tag{3.47}$$

with $h_s \leq h_c \leq h_i$.

When applying this solution to the excess rainfall of Parlange *et al.* (1981) as given by (3.37) and defining

$$x_a = \frac{5}{3}KR_0^{2/3}\tau^{5/3}\int_0^{t/\tau}(\frac{1}{2}-e^{-t'}+\frac{1}{2}e^{-2t'}+\frac{h_s}{R_0\tau})^{2/3}dt', \tag{3.48}$$

$$x_b = \frac{5}{3}KR_0^{2/3}\tau^{5/3}\int_0^{t/\tau}(\frac{1}{2}-e^{-t'}+\frac{1}{2}e^{-2t'}+\frac{h_i}{R_0\tau})^{2/3}dt', \tag{3.49}$$

.

then for $x < x_a$, the solution is

$$\frac{h}{R_0\tau} = e^{-t_0/\tau}-e^{-t/\tau}-\frac{1}{2}e^{-2t_0/\tau}+\frac{1}{2}e^{-2t/\tau}+\frac{h_s}{R_0\tau}, \tag{3.50}$$

$$x = mK\int_{t_0}^{t}h^{m-1}dt, \tag{3.51}$$

For $x > x_b$, the solution is

$$\frac{h}{R_0\tau} = \frac{1}{2}-e^{-t/\tau}+\frac{1}{2}e^{-2t/\tau}+\frac{h_i}{R_0\tau}, \tag{3.52}$$

$$x = mK\int_{0}^{t}h^{m-1}dt+x_0, \tag{3.53}$$

and lastly for $x_a \le x \le x_b$,

$$\frac{h}{R_0\tau} = \frac{1}{2}-e^{-t/\tau}+\frac{1}{2}e^{-2t/\tau}+\frac{h_c}{R_0\tau}, \tag{3.54}$$

$$x = mK\int_{0}^{t}h^{m-1}dt. \tag{3.55}$$

Fig. (3.8) gives the plot of the normalized height $h/R_0\tau$ as a function of the fractional distance down the plane x/L for various times $t/\tau = 0.5, 1, 1.5, 2.0, 2.5$ and $h_s/R_0\tau = 0.1$, $h_i/R_0\tau = 0.2$. L is the value of x calculated from (3.51) when $t = 3t_m$ and $t_0 = 0$. x_a and x_b is calculated by using Simpson's method.

Note that the values of h_s and h_i used here are bigger than realistic because we want to show the result more clearly. If h_s and h_i have smaller values, the green parts in above plot will be too small to be noticed.

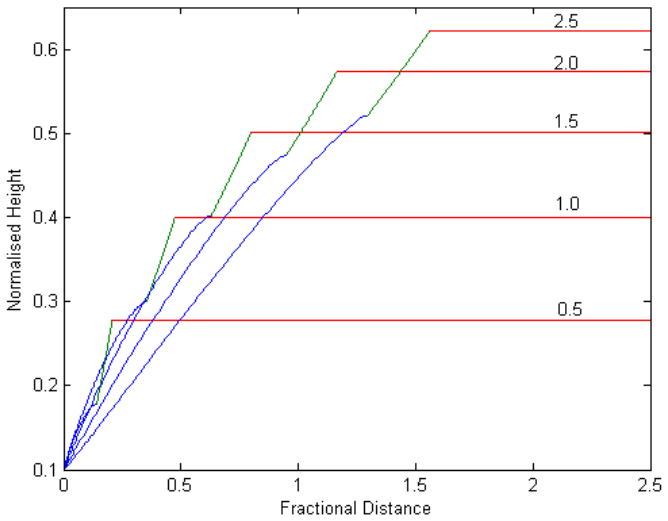

Figure 3.8: Plot of the normalized height $h/R_0\tau$ as a function of the fractional distance down the plane x/L, for various reduced times $t/\tau = 0.5, 1, 1.5, 2, 2.5$, $h_s/R_0\tau = 0.1$ and $h_i/R_0\tau = 0.2$.

3.2.1.3 $h_s > h_i$

With $h_s > h_i$ there will again be a region where characteristics from the x and t axis intersect, resulting in a shock whose path is denoted by $x_s(t)$. The solution for $x < x_s(t)$ is still given by (3.42) and (3.43) while for $x > x_s(t)$ it is described by (3.44) and (3.45). To find the position of the shock requires using (3.30) again which results in

$$\frac{dx_s}{dt} = \frac{K[\int_0^t R dt' + h_i]^m - Kh(x_s^-, t)^m}{\int_0^t R dt' + h_i - h(x_s^-, t)} \tag{3.56}$$

with $h(x_s^-, t)$ found from (3.42) and (3.43). Clearly (3.56) must be integrated numerically and requires knowledge of t_0 in order to find $h(x_s^-, t)$. As the numerical integration routine produces future estimates of x_s and t, their values are used in (3.43) to solve for t_0, which is then used in (3.42) to give $h(x_s^-, t)$.

The solution for $h_s > h_i$ is shown in Fig. (3.9). The normalized height $\frac{h}{R_0\tau}$

is plotted as a function of the fractional distance down the plane x/L for various times $t/\tau = 0.5, 1, 1.5, 2.0, 2.5$ and $\frac{h_s}{R_0\tau} = 0.2$, $\frac{h_i}{R_0\tau} = 0.1$.

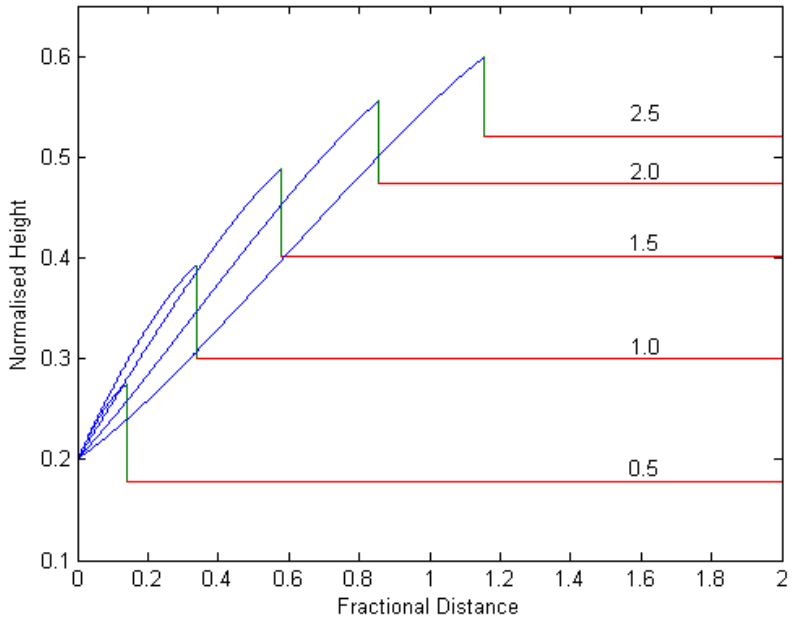

Figure 3.9: Plot of the normalized height $\frac{h}{R_0\tau}$ as a function of the fractional distance down the plane x/L, for various reduced times $t/\tau = 0.5, 1, 1.5, 2.0, 2.5$ and $h_s/R_0\tau = 0.2$, $h_i/R_0\tau = 0.1$.

3.2.2 $R(t) \geq 0$, $0 \leq t \leq t^*$ and $R(t) < 0$, $t > t^*$

In reality, the excess rainfall rate $R(t)$, is not always positive. Initially the rainfall rate exceeds the infiltration rate, $R(t) > 0$. When the rainfall rate decreases there will be some time $t = t^*$ at which the rainfall and infiltration rates are equal and so $R(t^*) = 0$. For $t > t^*$, infiltration is dominant and $R(t)$ becomes negative, and as $t \to \infty$ the excess rainfall rate may be assumed to approach $-k_{sat}$ where k_{sat} is the saturated hydraulic conductivity. A typical functional

form for $R(t)$ which has these properties is given by a simple extension of (3.37), i.e.

$$R(t) = R_0(e^{-bt} - \frac{k_{sat}}{R_0})(1 - e^{-bt}) \tag{3.57}$$

and is shown in Fig. (3.11). Thus the solution of (3.1) is divided into two parts for $R(t) \geq 0$, $t \leq t^*$ and $R(t) < 0$, $t > t^*$.

3.2.2.1 $h_s = h_i = h_b$

As $t \to \infty$, $R \to -k_{sat}$ and the steady state solution of (3.1) is given by (Rose *et al.*, 1983)

$$q = Kh_b^m - k_{sat}x \tag{3.58}$$

or

$$h = (h_b^m - \frac{k_{sat}x}{K})^{1/m} \tag{3.59}$$

since $q = Kh^m$.

The maximum distance (3.59) holds for is given by setting $h = 0$, which gives

$$x_f = \frac{Kh_b^m}{k_{sat}} \tag{3.60}$$

where x_f is the maximum front position that water gets to when the boundary condition remains at $h_s = h_b$, and then $h = 0$ for $x \geq x_f$.

As shown in Fig. (3.10), the characteristic which emanates from the origin divides the $x - t$ plane into three regions. In region B, the solution is the same as for the case $R \geq 0$, $t \geq 0$ and given by

$$h = \int_0^t R(t^{'})dt^{'} + h_b, \tag{3.61}$$

$$x = mK \int_0^t h^{m-1}dt^{'} + x_0. \tag{3.62}$$

In region A, the solution is

$$h = \int_{t_0}^t R(t^{'})dt^{'} + h_b, \tag{3.63}$$

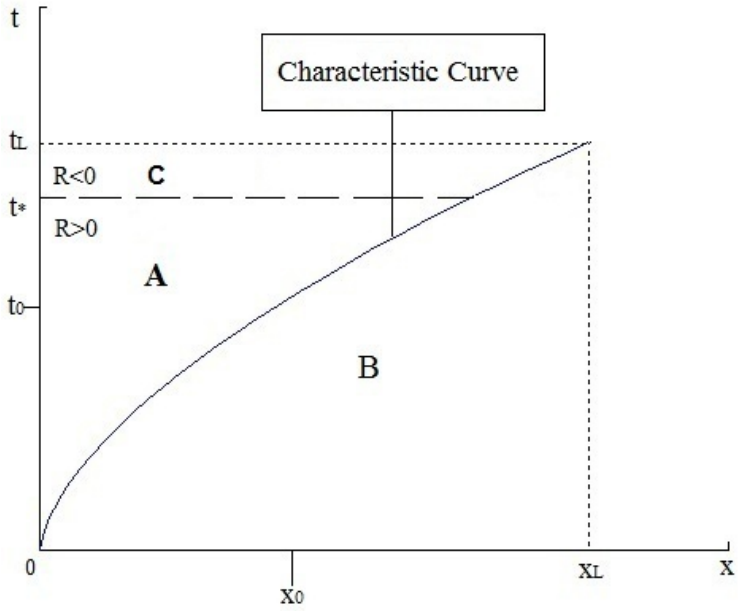

Figure 3.10: Four regions in the $x - t$ plane divided by the characteristic from $(0, 0)$

$$x = mK \int_{t_0}^{t} h^{m-1} dt'. \tag{3.64}$$

In region C, the solution is still given by (3.63) and (3.64) but t_0 now has different ranges depending on the time t. These will be discussed below.

For $R(t)$ as shown in Fig. (3.11), then consider any time $t > t^*$ such that $\int_0^t R dt' > -h_b$. Thus t_0 will still vary over the range $0 < t_0 < t$ with $t_0 = t$ implying $x = 0$. Now for $t^* < t_0 < t$, $\int_{t_0}^{t} R dt' < 0$ and from (3.63) and (3.64), it is clear that h must decrease with x, i.e. $\partial h/\partial x < 0$. For the range $0 < t_0 < t^*$ the integral in (3.63) will begin to increase again and h will then start to increase with x, i.e. $\partial h/\partial x > 0$. Consequently there is a local minimum in $h(x, t)$ which occurs at $x = x^*$ with x^* given by

$$x^* = mK \int_{t^*}^{t} h^{m-1} dt', \tag{3.65}$$

as shown in Fig. (3.12). This local minimum will touch the x axis at some time

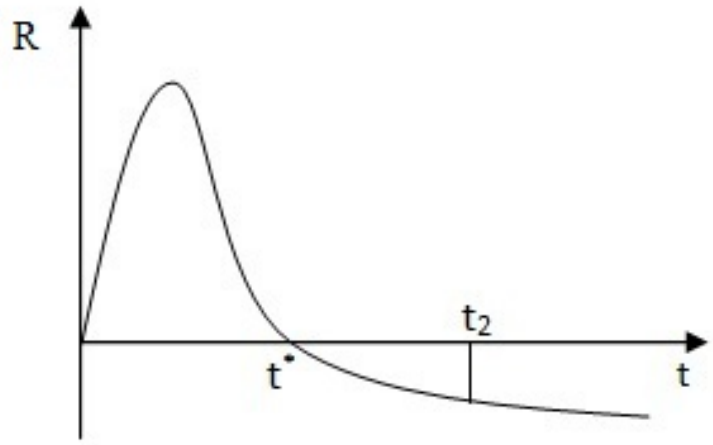

Figure 3.11: R as a function of t

$t = t_2$ with $t_2 > t^*$ defined by

$$\int_{t^*}^{t_2} R dt = -h_b, \tag{3.66}$$

resulting in $h = 0$ at $x = x_2$ where

$$x_2 = mK \int_{t^*}^{t_2} (\int_{t^*}^{t} R dt + h_b)^{m-1} dt. \tag{3.67}$$

Fig. (3.12) shows that for $t^* < t < t_2$, h heads to zero at $x = x^*$ and $h = 0$ at $x = x_2$, $t = t_2$.

Therefore, we divide the solutions into two regions, for $t < t_2$ and for $t \geq t_2$.

(a) For $t < t_2$, $h > 0$ for all $x > 0$ and the solution is given by (3.63) and (3.64) with $0 < t_0 \leq t$.

(b) For $t \geq t_2$, there will be two drying fronts appearing on the plane as shown in Fig. (3.13). They start from $x = x_2$ at $t = t_2$, with one moving upslope towards x_f and one moving downslope until it infiltrates and disappears. We define $x_3(t)$ as the edge of the upslope drying front and $x_4(t)$ as the edge of the downslope drying front which give the locations where $h = 0$ as a function of time.

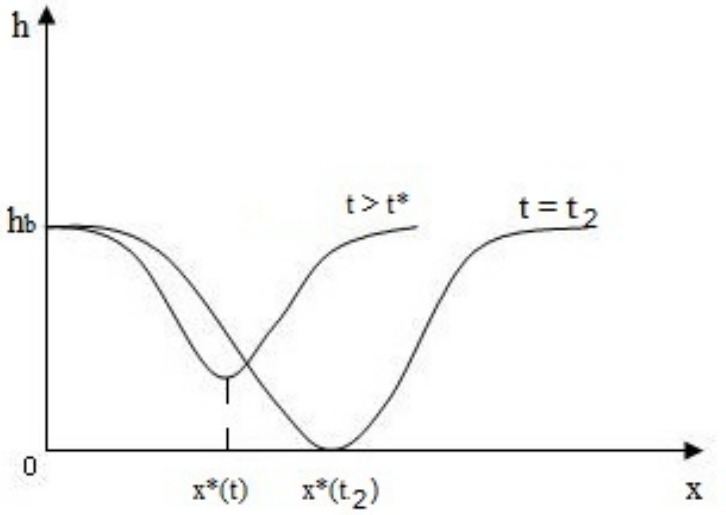

Figure 3.12: h varies with x at $t < t_2$

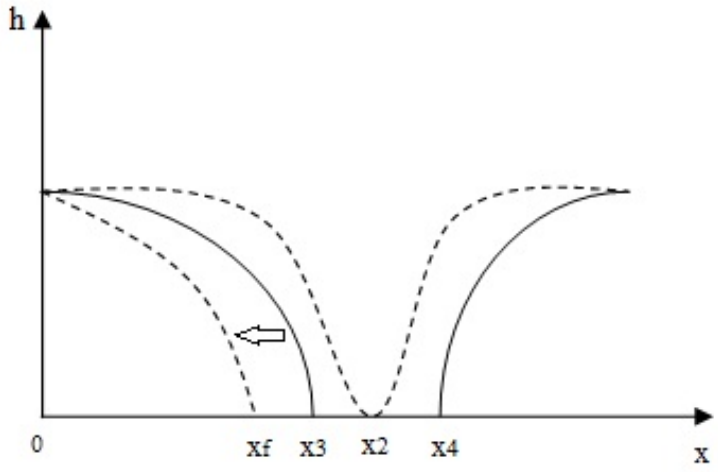

Figure 3.13: Two drying fronts $x_3(t)$ and $x_4(t)$

(I) Upslope drying solution

As shown in Fig. (3.14), there exists for all t ($t \geq t_2$), a value t_3 ($t^* \leq t_3 < t$)

such that

$$h = \int_{t_3}^{t} R dt^{'} + h_b = 0, \tag{3.68}$$

or

$$\int_{t_3}^{t} R dt^{'} = -h_b. \tag{3.69}$$

Obviously t_3 depends on t and as t increases t_3 increases.

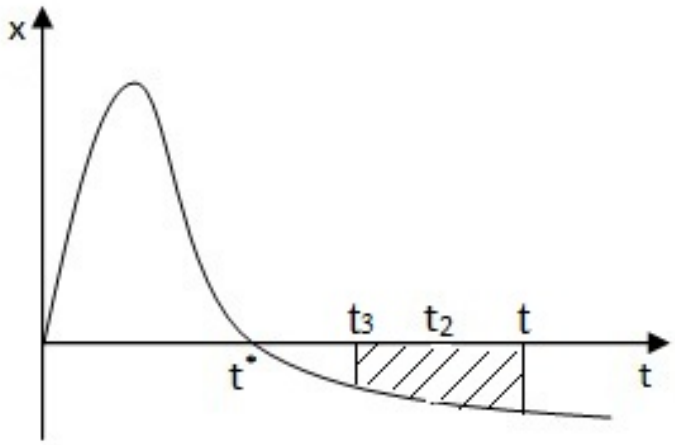

Figure 3.14: t_3 for upslope drying front when $t \geq t_2$

Thus the solution for $0 < x < x_3(t)$ is given by (3.63) and (3.64) with $t_3 \leq t_0 \leq t$ and

$$x_3(t) = mK \int_{t_3}^{t} h^{m-1} dt'. \tag{3.70}$$

as $t \to \infty$, $x_3(t) \to x_f$ and the upslope solution approaches (3.59).

(II) Downslope drying solution

Fig. (3.15) shows that for $t > t_2$ it is also possible to define a value t_4 $(0 \leq t_4 < t^*)$ such that

$$h = \int_{t_4}^{t} R dt^{'} + h_b = 0. \tag{3.71}$$

Note that t_4 is also dependent on t and t_4 decreases with an increase of t.

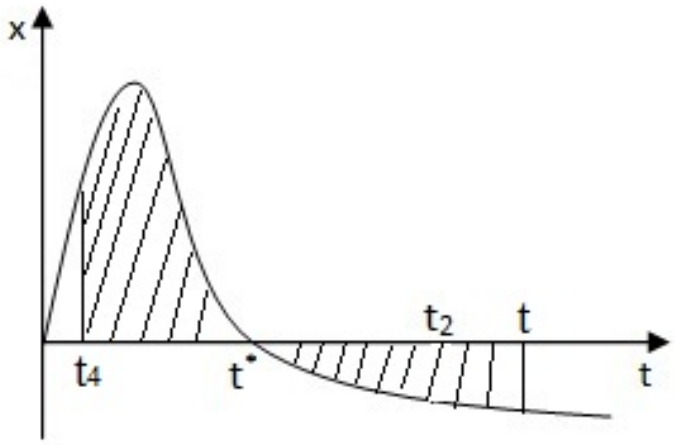

Figure 3.15: t_4 for downslope drying front when $t \geq t_2$

Thus the solution for $x > x_4(t)$ is then given by (3.63) and (3.64) with $0 \leq t_0 \leq t_4$ with

$$x_4 = mK \int_{t_4}^{t} h^{m-1} dt'. \tag{3.72}$$

This downslope drying solution holds until either $x_4(t)$ has reached the end of the slope, or all the water has infiltrated, which is given by $t = t_d$ where t_d is defined by

$$\int_0^{t_d} R dt' = -h_b. \tag{3.73}$$

This analytical solution is applied to a simple case with $R = R_0(\exp(-bt) - Ksat/Ro)(1-\exp(-bt))$. Fig. (3.16) shows the analytical and numerical solution for $t > t^*$ and $h_b = 1\,mm$. For $h_b = 0$, the solution is consistent with the solution given by Sander *et al.* (1990). The parameters used in the code are: $m = 5/3$, $K = 6.6144$, $R_0 = 1.5 \times 10^{-4}$, $Ksat = 3 \times 10^{-5}$, $b = 0.0181$ and $\Delta x = 0.01$.

Fig. (3.16) clearly shows the decrease in h from $x = 0$ for $t > t^*$ and the local minimum in h is seen to approach $x = 6$ approximately around $t = t_2 = 2.8\ mins$. For $t > 2.8\ mins$, the upslope and downslope profiles are seen to emerge and move

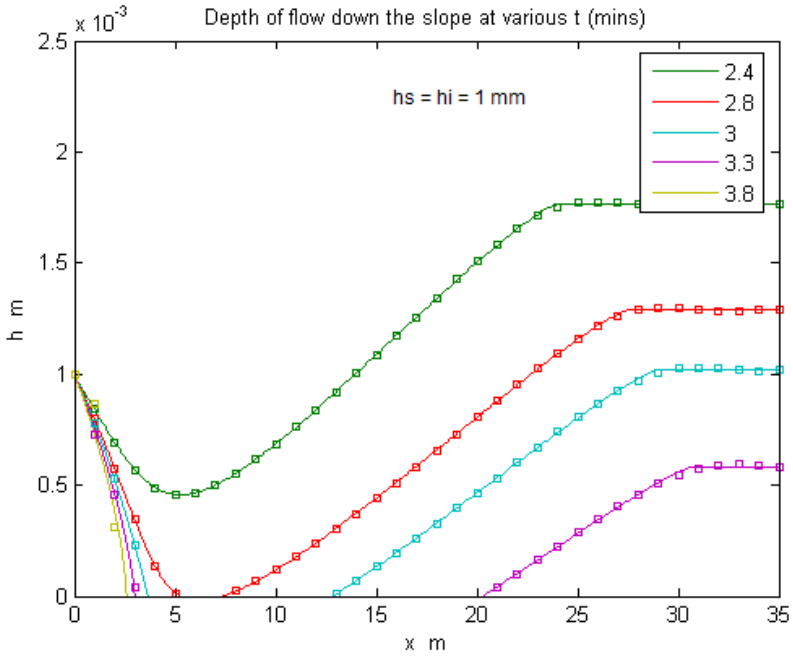

Figure 3.16: Depth of flow down the slope at various time: analytical (line), numerical (squares).

with the upslope profile approaching steady state. The numerical results were obtained using the method of lines which is discussed in detailed in section 4.1.2. The numerical results were included as a consistency check on the computations of the analytical solution.

3.2.2.2 $h_s < h_i$

This solution follows along similar lines to the previous one except for the inclusion of an expansion wave. However since $h = h_s$ at $x = 0$, t_2 is defined as

$$\int_{t^*}^{t_2} R dt' = -h_s, \tag{3.74}$$

then for $t \leq t_2$, $h \geq 0$ for all x and the solution is given by (3.42) to (3.47), i.e.

$$h = \int_{t_0}^{t} R dt' + h_s, \quad x = mK \int_{t_0}^{t} h^{m-1} dt', \quad x \leq x_a, \tag{3.75}$$

$$h = \int_{0}^{t} R dt' + h_i, \quad x = mK \int_{0}^{t} h^{m-1} dt' + x_0, \quad x \geq x_b, \tag{3.76}$$

$$h = \int_{0}^{t} R dt' + h_c, \quad x = mK \int_{0}^{t} h^{m-1} dt', \quad x_a < x < x_b, \tag{3.77}$$

where

$$x_a = mK \int_0^t [\int_0^{\bar{t}} R dt' + h_s]^{m-1} d\bar{t}, \tag{3.78}$$

$$x_b = mK \int_0^t [\int_0^{\bar{t}} R dt' + h_i]^{m-1} d\bar{t}, \tag{3.79}$$

and $h_s \leq h_c \leq h_i$, $0 \leq t_0 \leq t$.

Fig. (3.17) shows the form of the solution for $t = t_2$ with x_2 given by

$$x_2 = mK \int_{t^*}^{t_2} [\int_{t^*}^{t} R dt' + h_s]^{m-1} dt''. \tag{3.80}$$

For $t > t_2$, we again have two drying fronts x_3 and x_4 as shown in Fig. (3.18).

(I) Upslope drying solution

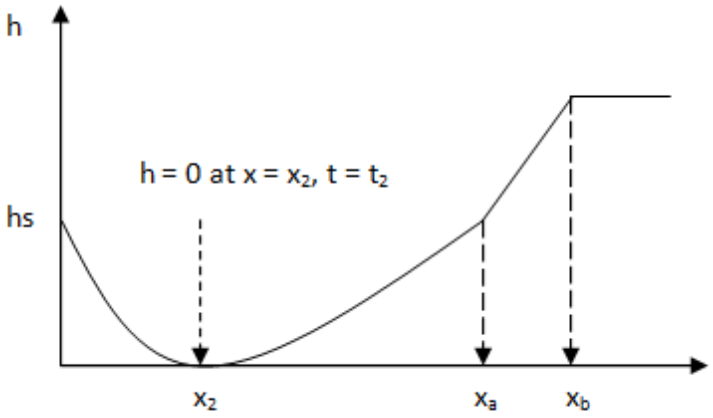

Figure 3.17: Depth of flow down the slope h varying with slope distance x at $t = t_2$

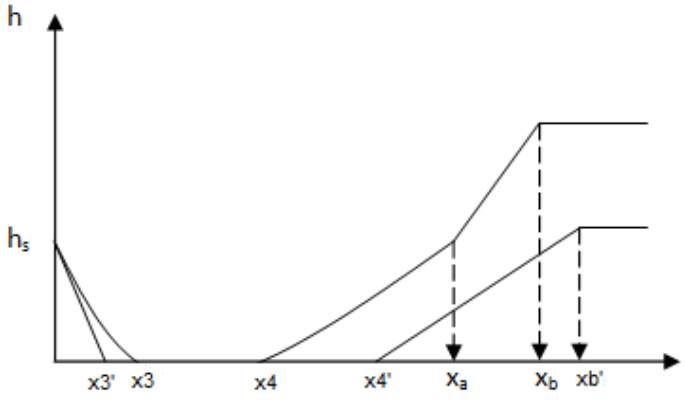

Figure 3.18: Depth of flow down the slope h varying with slope distance x at $t_2 < t < t_d$

There is no expansion wave in the upslope drying solution and the solution is the same as upslope drying solution for $h_s = h_i = h_b$ but with h_b replaced by h_s,

i.e. we can define t_3 as in Fig. (3.14) such that

$$\int_{t_3}^{t} Rdt^{'} = -h_s. \tag{3.81}$$

The solution is then given by

$$h = \int_{t_0}^{t} Rdt' + h_s, \quad x = mK \int_{t_0}^{t} h^{m-1} dt' \tag{3.82}$$

with $t_3 \leq t_0 \leq t$ and

$$x_3(t) = mK \int_{t_3}^{t} h^{m-1} dt' \tag{3.83}$$

with $x_f \leq x_3(t) \leq x_2$.

(II) Downslope drying solution

This solution includes two cases as shown in (3.18): (a) $t_2 < t < t_{ds}$, (b) $t > t_{ds}$ with t_{ds} is defined as the time at which the lower end of the expansion wave touches the x axis, i.e.

$$\int_{0}^{t_{ds}} Rdt' = -h_s. \tag{3.84}$$

(a) $t_2 < t < t_{ds}$

We still define $x_4(t)$ by (3.72) but with h_b replaced by h_s. The downslope solution for $x > x_4(t)$ is then given by

$$h = \int_{t_0}^{t} Rdt' + h_s, \qquad x = mK \int_{t_0}^{t} h^{m-1} dt', \qquad x_4(t) \leq x \leq x_a; \tag{3.85}$$

$$h = \int_{0}^{t} Rdt' + h_c, \quad x = \int_0^t [\int_0^{t'} Rdt'' + h_c]^{m-1} dt', \quad x_a < x < x_b; \tag{3.86}$$

$$h = \int_{0}^{t} Rdt' + h_i, \qquad x = mK \int_0^t h^{m-1} dt' + x_0, \qquad x \geq x_b, \tag{3.87}$$

with $0 \leq t_0 \leq t_4$.

(b) $t > t_{ds}$

The downslope solution now is given by (3.86) and (3.87) with x_a is replaced by $x_4(t)$ and h_c is restricted to $h_n(t) \leq h_c \leq h_i$ with $h_n(t)$ is defined by

$$\int_{0}^{t} Rdt' = -h_n(t), \tag{3.88}$$

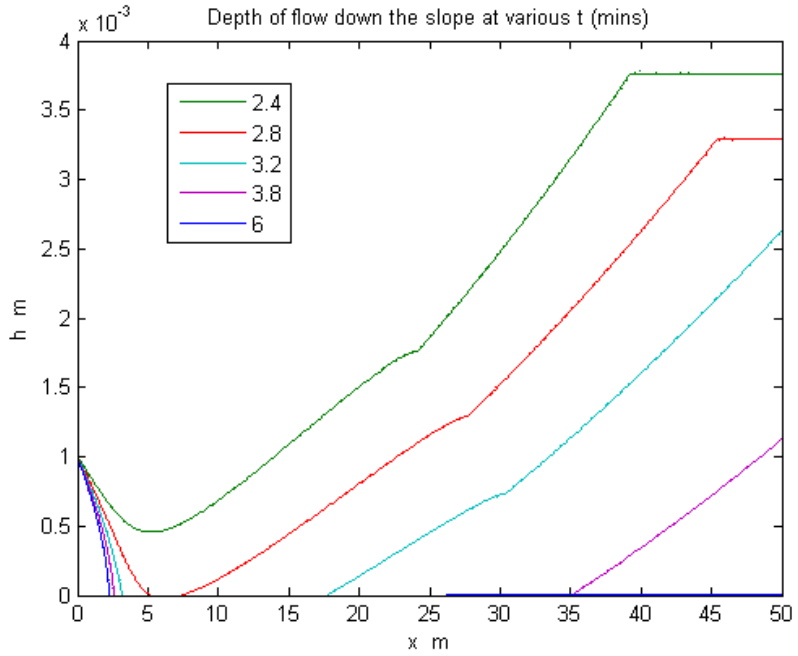

Figure 3.19: Depth of flow down the slope at various time: analytical (line), numerical (dotted line).

which allows $x_4(t)$ to be determined from

$$x_4(t) = \int_0^t [\int_0^{t'} Rdt'' + h_n]^{m-1} dt'. \tag{3.89}$$

This solution also holds until either $x_4(t) \geq L$ or the slope dries as defined by $t = t_d$ where

$$\int_0^{t_d} Rdt = -h_i. \tag{3.90}$$

This analytical solution is again applied to the simple case of $R(t)$ given by (3.57). Fig. (3.19) shows the analytical and numerical solution for $h_i = 3 \ \ mm$ and $h_s = 1 \ \ mm$. As it shows, the two solutions are virtually indistinguishable. The other parameters used are same as for $h_s = h_i = h_b = 1\, mm$.

3.2.2.3 $h_s > h_i$

This is a shock wave then it is necessary to consider the movement of the shock down the hillslope. First note that the maximum time any initial water (h_i) can remain on the hillslope is given by the downslope drying time t_d as defined in (3.90). Recalling also that t_2 is the time that the local minimum in $h(x,t)$ intersects the x axis and given by (3.74). The intersection of $h(x,t)$ with the x axis is x_2 and given by (3.80). The complete solution for $h_s > h_i$ is considered on the basis of whether shock position passes x_2 at $t = t_2$ or not.

For $t < t_2$, $h > 0$ on the whole domain. Thus the solution for this time period follows exactly the same procedure as outlined in section 3.2.1.3 with the shock position x_s found from (3.56). Note that it is necessary to check if $t_d < t_2$. In this case, the solution given in section 3.2.1.3 still holds for $t < t_d$. But for $t_d < t < t_2$, the shock condition is simplified to

$$\frac{dx_s}{dt} = Kh(x_s^-, t)^{m-1}, \tag{3.91}$$

as now $h(x_s^+, t) = 0$.

Typical $h(x)$ profiles are presented in Fig. (3.20) and Fig. (3.21) for $t < t_2 < t_d$ and $t_d < t < t_2$ respectively.

For $t \geq t_2$, the solution is still considered under two possible conditions: (i) $t_2 < t_d$, (ii) $t_2 > t_d$.

(i) $t_2 < t_d$

For this case, the shock position has passed x_2 at $t = t_2$, i.e. $x_s(t_2) > x_2$ as $h(x_s^+, t) > 0$ at $t = t_2$. Therefore, there are two drying fronts again. The upslope solution $0 < x < x_3(t)$ is as before and given by (3.81) to (3.83) with $t_3 \leq t_0 \leq t$.

The trailing edge of the downslope drying solution, $x_4(t)$ is given by

$$x_4(t) = mK \int_{t_4}^{t} (\int_{t_4}^{t'} R dt'' + h_s)^{m-1} dt', \tag{3.92}$$

where $t_4 < t^*$ for any time $t > t_2$ is defined from

$$h = \int_{t_4}^{t} R dt' + h_s = 0. \tag{3.93}$$

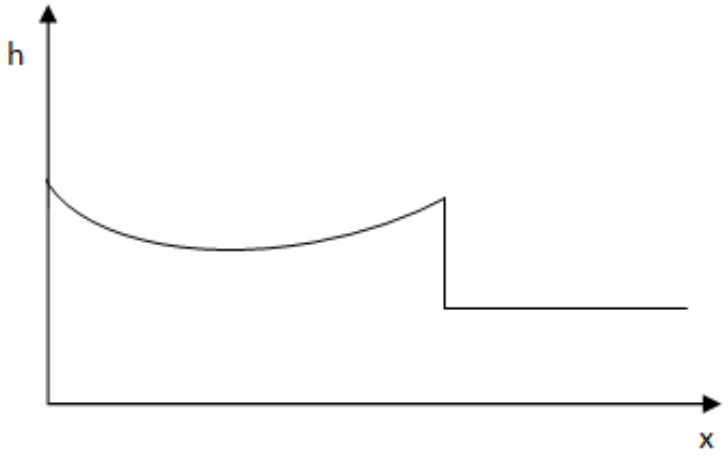

Figure 3.20: A typical $h(x)$ profile for $t < t_2 < t_d$

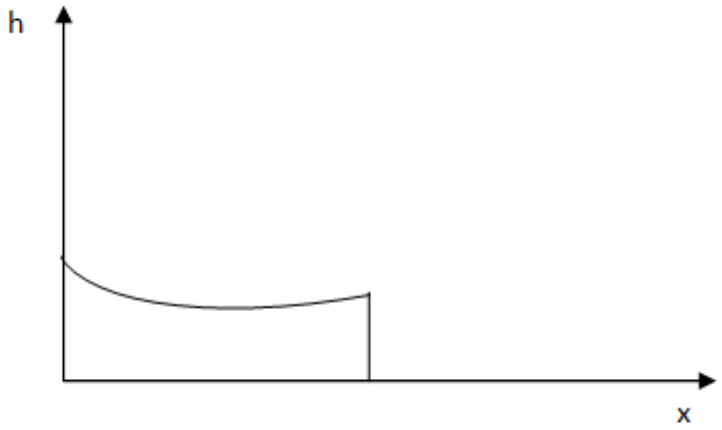

Figure 3.21: A typical $h(x)$ for $t_d < t < t_2$

The downslope solution is therefore given by

$$h = \int_{t_0}^{t} R dt' + h_s, \quad x = mK \int_{t_0}^{t} h^{m-1} dt', \quad x_4(t) \leq x \leq x_s(t), \tag{3.94}$$

and

$$h = \int_{0}^{t} R dt' + h_i, \quad x > x_s(t), \tag{3.95}$$

where $t_0^s \leq t_0 \leq t_4$ with t_0^s being found as part of integrating (3.56) to find $x_s(t)$. A typical solution profile for $t_2 < t < t_d$ is shown in Fig. (3.22) while Fig. (3.23) shows one for $t_2 < t_d < t$ in which $h(x_s^+, t) = 0$ and x_s is calculated from (3.91).

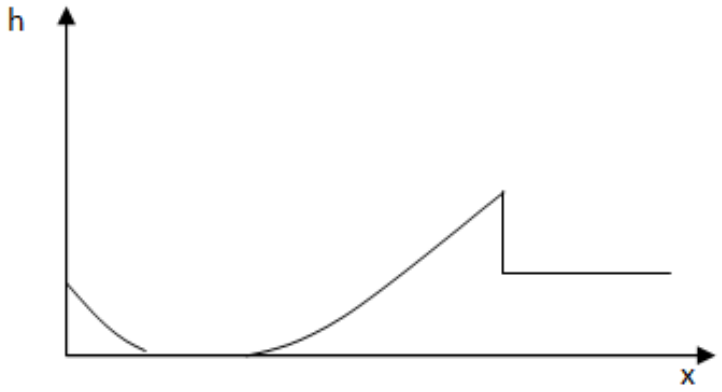

Figure 3.22: A typical $h(x)$ for $t_2 < t < t_d$

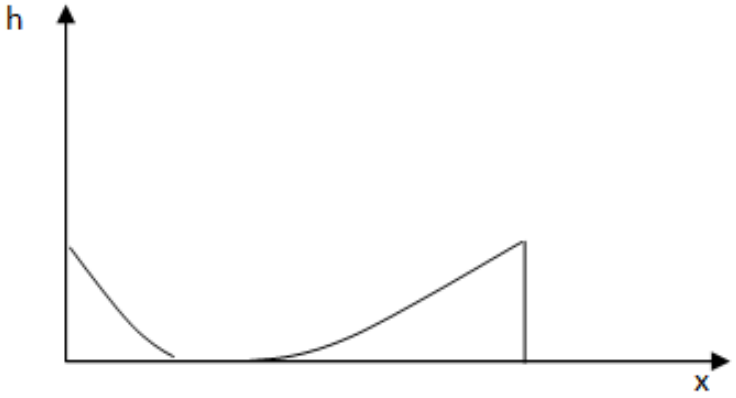

Figure 3.23: h vs x for $t_2 < t_d < t$

(ii) $t_d < t_2$

The solution is further considered under two possibilities: a. $x_s(t_2) > x_2$ or b. $x_s(t_2) < x_2$.

a. $x_s(t_2) > x_2$

There will exist both upslope and downslope drying solutions where the upslope solutions are given by (3.81) to (3.83) and the downslope solutions are given by (3.94) with $h = 0$, $x > x_s$. A typical profile of h as shown in (3.23).

b. $x_s(t_2) = x_2$

Remember that since $t_d < t_2$, then for $t_d < t < t_2$, $h(x_s^+, t) = 0$. As t increases from t_d to t_2, the height of the shock reduces such that as $t \to t_2$, $x_s \to x_2$ but with $h(x_s^-, t) \to 0$. Thus at $t = t_2$ the shock actually disappears. Consequently for $t > t_2$ as downslope solution emerges and only the upslope drying solution exists.

The solution therefore for $0 < x < x_3(t)$ is again given by (3.81) to (3.83) with $t_3 \leq t_0 \leq t$ and h approaches (3.59) as $x_3 \to x_f$ and $t \to \infty$. A typical $h(x, t)$ profile is presented as in Fig. (3.24).

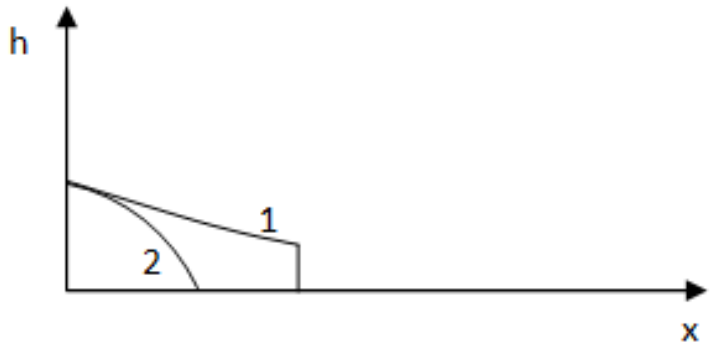

Figure 3.24: A typical $h(x)$ for 1. $t_d < t < t_2$ and 2. $t > t_2$

For $R(t)$ as given in (3.57), Fig. (3.25) and Fig. (3.26) shows the comparison between numerical and analytical solution of $h(x, t)$ for $t_2 < t_d$, $t_d < t_2$ and $x_s(t_2) > x_2$ respectively for $t > t^*$ while Fig. (3.27) presents the analytical solution of $h(x, t)$ only for $t_d < t_2$ and $x_s(t_2) < x_2$ as it shows more clearly the evolution of $h(x, t)$ in it. The parameters used are same as before except those

presented in the caption of each figure. Excellent agreement is found between the analytical and numerical solutions showing that we have implement analytical solution and shock tracking procedures correctly.

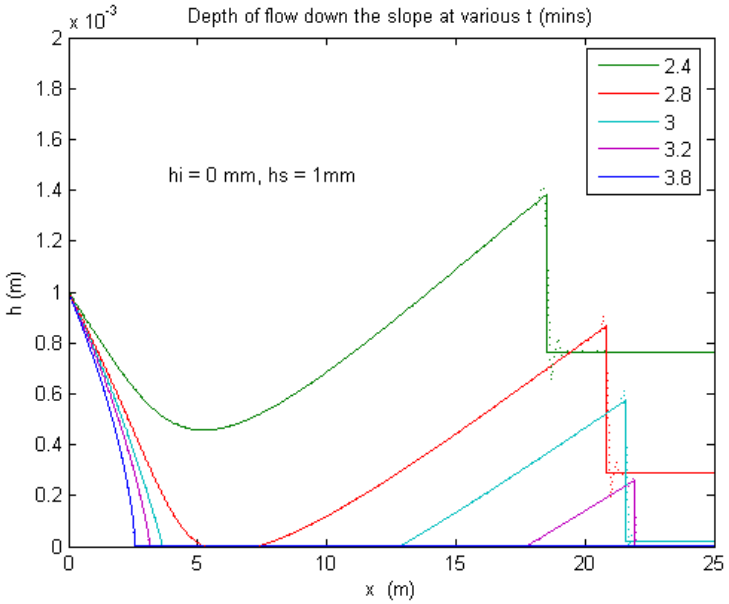

Figure 3.25: Depth of flow down the slope varying with t at different time: analytical solution (solid line), numerical solution (dotted line) for $t_2 < t_d$, $R_0 = 1.5e{-}4$, $k_{sat} = 3e - 5$ and $b = 0.0181$

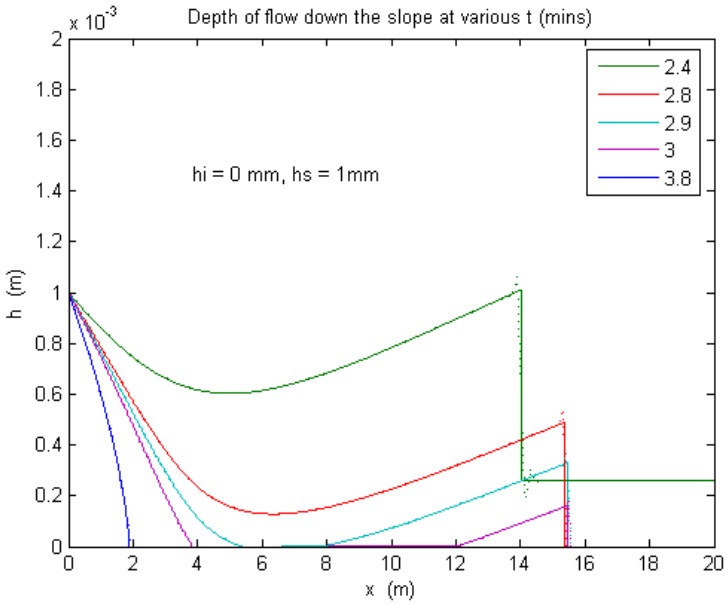

Figure 3.26: Depth of flow down the slope varying with t at different time: analytical solution (solid line), numerical solution (dotted line) for $t_d < t_2$ and $x_s > x_2$, $R_0 = 1.5e-4$, $k_{sat} = 7e-5$ and $b = 0.0081$

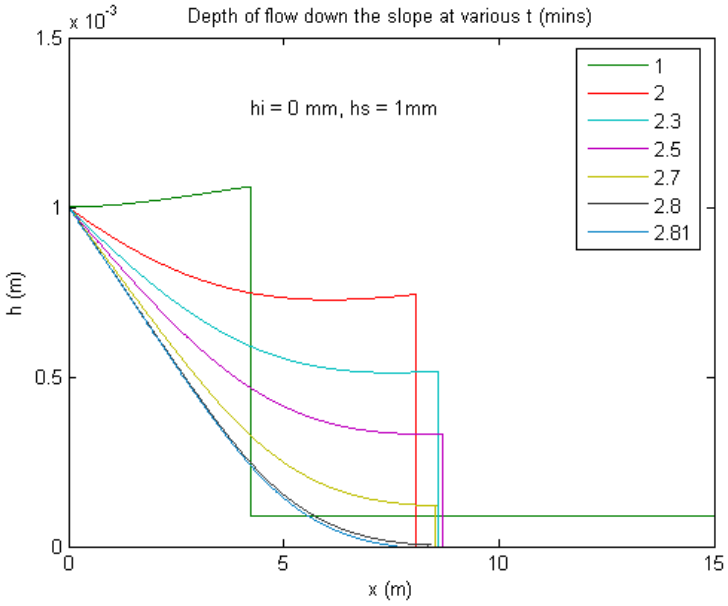

Figure 3.27: Depth of flow down the slope varying with t at different time: analytical solution only for $t_d < t_2$ and $x_s < x_2$, $R_0 = 1e-4$, $k_{sat} = 7e-5$ and $b = 0.0058$

3.3 Conclusion

The new analytical solutions are obtained by using the method of characteristics and presented in this chapter for the kinematic flow equation with different initial values h_i and boundary values h_s. There are three combinations of h_i and h_s investigated here; (a) $h_s = h_i$, the solution obtained for this case is shown to be consistent with the solution given in Henderson and Wooding (1964) for $h_s = h_i = 0$. (b) $h_s < h_i$, where the solution develops an expansion wave and (c) $h_s > h_i$, where a discontinuous shock wave (or to be more formally correct - a contact discontinuity) develops. Both constant and time dependent excess rainfalls are considered for these three combinations of initial and boundary conditions. In the case of time dependent excess rainfall, a further two sub-cases were considered, these being (i) $R(t) > 0$ for all $t > 0$ and (ii) $R(t) > 0$, $0 < t < t^*$ and $R(t) < 0$, $t > t^*$. The latter results in a much more complicated solution behavior compared to the former one due to the appearance of two drying fronts when $t > t_2$ as defined in (3.66) and (3.74), with either an expansion or shock wave included in one of the drying fronts. The analytical solutions of the kinematic wave flow with $R(t) > 0$, $0 < t < t^*$ and $R(t) > 0$, $t > t^*$ under those three combinations of h_i and h_s are compared to their numerical solutions solved by using the method of lines. The comparisons show that the two solutions are totally consistent and the ability of the numerical solution to capture the expansion and shock are very good and accurate. These new solutions are a comprehensive extension of the solution given by Sander *et al.* (1990).

Although, the boundary and initial conditions used for obtaining solutions for the kinematic wave equation do not have a direct relevance to hillslope overland flow, they can be applied in a laboratory flume to provide a wider range of hydraulic flow conditions and to test the HR model's ability to match the data from the erosion experiments under these conditions. Their other potential application is for irrigation ditches in the field. However, their most important value is to provide a stringent test of any numerical code.

CHAPTER 4

Time-dependent Hairsine-Rose Model

4.1 Standard HR Model

The time-dependent HR model equations that only consider water flow driven soil erosion processes are expressed as

$$\frac{\partial(hc_i)}{\partial t} + \frac{\partial(qc_i)}{\partial x} = r_i + r_{ri} - d_i, \tag{4.1}$$

and

$$\frac{\partial m_i}{\partial t} = d_i - r_{ri}. \tag{4.2}$$

In this chapter h and q will be taken as constant, while solutions for h and q varying with x, t will be discussed in Chapter 5.

The entrainment rate r_i and re-entrainment rate r_{ri} as given in Hairsine and Rose (1992a) and discussed in section 2.2.2 (see equations (2.131) and (2.133)) and given again below for convenience

$$r_i = p_i(1 - H)\frac{F}{J}(\Omega - \Omega_{cr}), \tag{4.3}$$

$$r_{ri} = H\frac{F}{gh}(\frac{\rho_s}{\rho_s - \rho})(\Omega - \Omega_{cr})\frac{m_i}{m_t}, \tag{4.4}$$

with the deposition rate d_i

$$d_i = v_i c_i, \tag{4.5}$$

and

$$H = min(\frac{m_t}{m_t^*}, 1). \tag{4.6}$$

In (4.3), p_i is the proportion of sediment in size class i and satisfies $\sum_{i=1}^{I} p_i = 1$. Equation (4.3) generalizes the entrainment rate of Hairsine and Rose (1991) who take $p_i = 1/I$.

In this chapter, we are going to consider solutions of the unsteady HR model and their application to the experimental data given in Polyakov and Nearing (2003). While full details of their experiments are given in section 4.1.4, it is worth noting here that they were conducted under flow driven conditions only and in the absence of rainfall, hence both the detachment and redetachment terms can be neglected. Sander *et al.* (2007a) were able to show that the HR model could accurately reproduce the separate particle size steady state suspended sediment concentrations under both net erosional and net depositional flows. This comparison was a stringent test of the HR approach to sediment transport modelling as opposed to the traditional use of models based on the concept of a sediment transport capacity. The aim of this chapter is to extend the analysis of Sander *et al.* (2007a) to test the ability of the HR model to reproduce the non-steady flow data presented in Polyakov and Nearing (2003). Section 4.1.1 and 4.1.2 first considers methods for solving equations (4.1) and (4.2) followed by section 4.1.4 which considers the comparison against the experimental data.

4.1.1 Semi-solution by the Method of Characteristics

For general boundary and initial conditions solutions of (4.1) and (4.2) require numerical methods. However they can be reduced to a system of ordinary differential equations on a specific sub-domain of x using the method of characteristics

(MOC) when there are spatially uniform initial conditions. This is shown by first considering net depositional conditions where $H = 1$, then by adding (4.1) and (4.2), and remembering that h and q are constants, results in

$$h\frac{\partial c_i}{\partial t} + q\frac{\partial c_i}{\partial x} = \frac{\partial m_i}{\partial t} \tag{4.7}$$

which can be integrated to obtain

$$m_i - m_{io} = h(c_i - c_{io}) + q\int_0^t \frac{\partial c_i}{\partial x}dt \tag{4.8}$$

where m_{io} and c_{io} are the constant initial values for m_i and c_i respectively. Equation (4.8) gives m_i as a function of c_i, hence equations (4.3) - (4.4) and (4.6) can now be written as functions of c_i and (4.1) becomes a partial differential equation for c_i only. The main difficulty with (4.8) is the integral term, however that does not mean that it is of no use, on the contrary the method of characteristics allows us to get some rather useful results from this form.

Using the method of characteristics (4.1) can be written as

$$\frac{dt}{h} = \frac{dx}{q} = \frac{dc_i}{r_{ri}(c_i) - v_i c_i}. \tag{4.9}$$

Consider the characteristic emanating from the origin, i.e. $t = 0$, $x = 0$, then using the first two terms in (4.9)

$$x = \frac{q}{h}t \tag{4.10}$$

which marks the boundary between the two domains of the solution. Since the boundary condition on c_i and the initial condition are not equal, (4.10) also gives the speed of the contact discontinuity or abrupt front in concentration propagating downstream from the $x = 0$ boundary. The region where $x > qt/h$ is only effected by the constant initial condition on c_{i0} and since $\partial c_i/\partial x = 0$ at $t = 0$, then $\partial c_i/\partial x = 0$ for all t for $x > qt/h$. Consequently for $x > qt/h$, the integral term is zero in (4.8). The solution in this region is then given from taking the first and third terms of (4.9), or solving

$$h\frac{dc_i}{dt} = \gamma\frac{m_{io} + h(c_i - c_{io})}{\sum_{i=1}^{I}[m_{io} + h(c_i - c_{io})]} - v_i c_i \tag{4.11}$$

subject to $t = 0$, $c_i = c_{i0}$ with $\gamma = \frac{F}{gh}\frac{\rho_s}{(\rho_s - \rho)}(\Omega - \Omega_{cr})$. The maximum concentration reached in this region is given by $dc_i/dt = 0$, or

$$\gamma \frac{m_{io} + h(c_i - c_{io})}{\sum_{i=1}^{I}[m_{io} + h(c_i - c_{io})]} = v_i c_i. \tag{4.12}$$

In the case when $H < 1$, all of the above analysis does not hold. However when $x > qt/h$ in (4.1) and (4.2), the solution is still independent of space and given by the system

$$h\frac{dc_i}{dt} = r_i + r_{ri} - d_i \tag{4.13}$$

and

$$\frac{dm_i}{dt} = d_i - r_{ri}. \tag{4.14}$$

Due to the many orders of magnitude variation in the particle settling velocities v_i, both (4.11) and (4.13) with (4.14) form a stiff system of equations. Consequently the MATLAB stiff system integrator ode15s is used to solve the two sets of equations.

4.1.2 Solving the HR Model Using the Method of Lines

The method of lines (MOL) produces a system of ordinary differential equations for each nodal point by discretising the spatial derivatives while maintaining the time derivative. Thus if we discretise the spatial domain as $x_j = (j-1)\triangle x$, $j = 1, 2, \ldots N$ and adopt the vector notation of $\mathbf{c}_i = c_i(x_j, t) = c_i^j(t)$, $\mathbf{m}_i = m_i(x_j, t) = m_i^j(t)$, $\mathbf{d}_i = d_i(x_j, t) = d_i^j(t)$, $j = 1, 2, \ldots N$, etc., then (4.1) and (4.2) can be expressed as the following coupled system of $2N$ ordinary differential equations for each size class as

$$h\frac{d\mathbf{c_i}}{dt} = -q\mathbf{D}\mathbf{c_i} + \mathbf{r_i} + \mathbf{r_{ri}} - \mathbf{d_i}, \tag{4.15}$$

$$\frac{d\mathbf{m_i}}{dt} = \mathbf{d_i} - \mathbf{r_{ri}}. \tag{4.16}$$

In (4.15), $\mathbf{D}$ is a differentiation matrix of size $(N \times N)$, whose entries depend on the order of the matrix. As this matrix operates on the advective derivative

term then the finite difference scheme needs to be upwind biased in order to compute stable solutions of (4.15). Examples of 1^{st}, 2^{nd} and 3^{rd} order upwind schemes for $\mathbf{D}$ are given below

$$\mathbf{D}_1 = \frac{1}{\Delta x}\begin{pmatrix} -1 & 1 & 0 & 0 & \cdots & 0 & 0 & 0 \\ -1 & 1 & 0 & 0 & \cdots & 0 & 0 & 0 \\ 0 & -1 & 1 & 0 & \cdots & 0 & 0 & 0 \\ & & \ddots & & & & & \\ & & & \ddots & & & & \\ & & & & \ddots & & & \\ & & & & & \ddots & & \\ 0 & 0 & 0 & 0 & \cdots & 0 & -1 & 1 \end{pmatrix} \tag{4.17}$$

$$\mathbf{D}_2 = \frac{1}{2\Delta x}\begin{pmatrix} -3 & 4 & -1 & 0 & \cdots & 0 & 0 & 0 \\ -1 & 0 & 1 & 0 & \cdots & 0 & 0 & 0 \\ 1 & -4 & 3 & 0 & \cdots & 0 & 0 & 0 \\ & & \ddots & & & & & \\ & & & \ddots & & & & \\ & & & & \ddots & & & \\ & & & & & \ddots & & \\ 0 & 0 & 0 & 0 & \cdots & 1 & -4 & 3 \end{pmatrix} \tag{4.18}$$

$$\mathbf{D}_3 = \frac{1}{6\Delta x}\begin{pmatrix} -11 & 18 & -9 & 2 & 0 & \cdots & 0 & 0 & 0 & 0 \\ -2 & -2 & 6 & -1 & 0 & \cdots & 0 & 0 & 0 & 0 \\ 1 & -6 & 3 & 2 & 0 & \cdots & 0 & 0 & 0 & 0 \\ 0 & 1 & -6 & 3 & 2 & \cdots & 0 & 0 & 0 & 0 \\ & & & \ddots & & & & & & \\ & & & & \ddots & & & & & \\ & & & & & \ddots & & & & \\ 0 & 0 & 0 & 0 & 0 & 1 & -6 & 3 & 2 & 0 \\ 0 & 0 & 0 & 0 & 0 & \cdots & -2 & 9 & -18 & 11 \end{pmatrix} \tag{4.19}$$

The third order scheme of (4.19) is used for computing solutions of (4.15) and (4.6) along with the ode15s MATLAB integrator.

4.1.3 Verification of the Numerical Solution

Parameter values used to compare the MOL solution with (4.13) and (4.14) were based on those from Polyakov and Nearing (2003) and Sander *et al.* (2007a), and are given in Table (4.1) and Table (4.2) below. Boundary and initial conditions for which the numerical solutions were obtained were

$$\begin{aligned} t = 0, x > 0, \;\; c_i = 0, \\ t > 0, x = 0, \;\; c_i = c_{i0} \end{aligned} \tag{4.20}$$

where $c_{i0} = 0$ for net erosion and given by Table (4.2) for net deposition flows.

Table 4.1: Hydraulic parameters used for simulation (assuming that the rill is rectangular).

Symbol	Value	Source
q	0.00115 $m^2\ s^{-1}$	Averaged values of those in Table (2)
h	5.55 mm	in Polyakov and Nearing (2003)
F	0.14	Optimized values to obtain the best fit for the experimental data in Fig. (1) in Polyakov and Nearing (2003)
J	25 $J\ kg^{-1}$	
Ω_{cr}	0.02 $W\ m^{-2}$	
m_t^*	3 $kg\ m^{-2}$	
ρ	1000 $kg\ m^{-3}$	from Sander *et al.* (2007a)
ρ_s	2000 $kg\ m^{-3}$	
S_0	0.07	

As stated earlier the MATLAB stiff system integrator ode15s[1] was used for the method of lines. Additional comparisons were also performed using other MATLAB integrators (ode45[1], ode23s[1]), which showed that we obtained at least 6 significant figures accuracy in solving the system of (4.13) and (4.14). By using a spatial step of $\triangle x = 0.01m$ the MOL produced a grid-independent solution

[1]They are the subroutines designed in MATLAB to integrate ordinary differential equations.

Table 4.2: Particle size distribution, settling velocities and the added sediment inflow concentration.

p_i	v_i $(m\ s^{-1})$	$c_i(0,t)$ $(kg\ m^{-3})$
0.376	0.0038	38.7
0.234	0.0137	24.1
0.2	0.0827	20.6
0.166	0.1369	17.1
0.0237	0.2317	2.5

to at least four significant figures. A comparison between the MOL and MOC solutions to (4.13) and (4.14) for $c_i(x)$ at $t = 0.15\ \ mins$ are shown in Fig. (4.1) where it can be seen that there is excellent agreement between the two methods. As stated earlier the MOC solution holds for the region $qt/h < x < L$ and applies for $0 < t < hL/q$.

A second test was performed to check that the MOL solution evolved to the different steady state analytical solutions of Sander *et al.* (2007a) for the net erosion and net deposition zones respectively. Fig. (4.2) again shows excellent agreement between the numerical and the analytical steady state solutions. The good level of agreement shown in both Fig. (4.1) and Fig. (4.2) along with the convergence shown by the numerical solution as $\triangle x$ was reduced gives confidence that the MOL solution was both accurate and reliable.

4.1.4 Application to Experimental Data

Polyakov and Nearing (2003) performed two sets of experiments to determine if transport capacity in a rill "is a unique value for a given soil, flow rate, and slope, and to determine if equilibrium sediment concentration in the rill obtained under [net] detachment was different from that observed under [net] deposition conditions." What their experiments showed was that the transport capacity

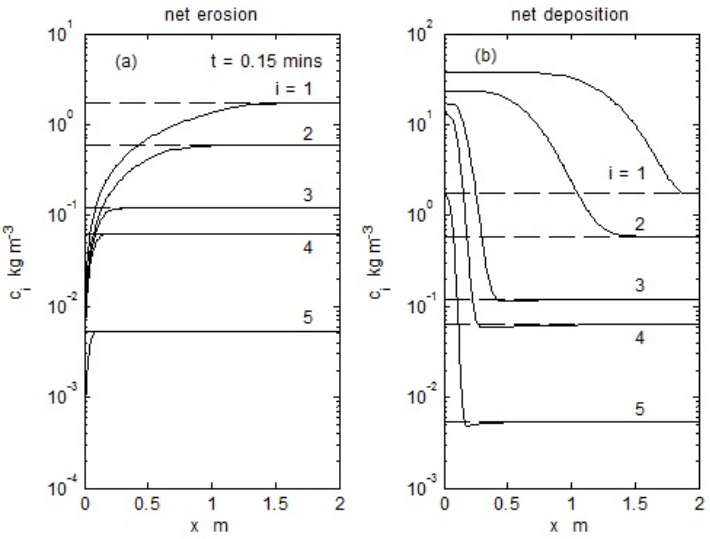

Figure 4.1: Comparison between $c_i(x,t)$ at $t = 0.15$ minutes from MOL (solid line) and MOC (dashed line) under net erosion conditions ($c_i = 0$ at $x = 0$) (a) and net deposition conditions $c_i(0,t)$ given by Table (4.2) (b). Smallest and largest size classed given by $i = 1$ and 5 respectively.

was not unique and that different values were obtained between the net erosion and net deposition experiments. Hence their experiments showed that transport capacity was hysteretic. One set of experiments considered steady state flow along an 8 m rill under both erosion and deposition conditions. Sander *et al.* (2007a) showed that the HR model could predict the transported size distribution of eroded particles for both steady state experiments as well as providing a physical explanation for hysteresis in the transport capacity. The second set of experiments of Polyakov and Nearing (2003) (on a 2 m rill) was concerned with studying the time variation in the behavior of eroded sediment as the inflow conditions at $x = 0$ were periodically cycled every 15 $mins$ between net erosion and net deposition states. The experimental results for a flow rate of 6 $l \ \ min^{-1}$ and the inflow

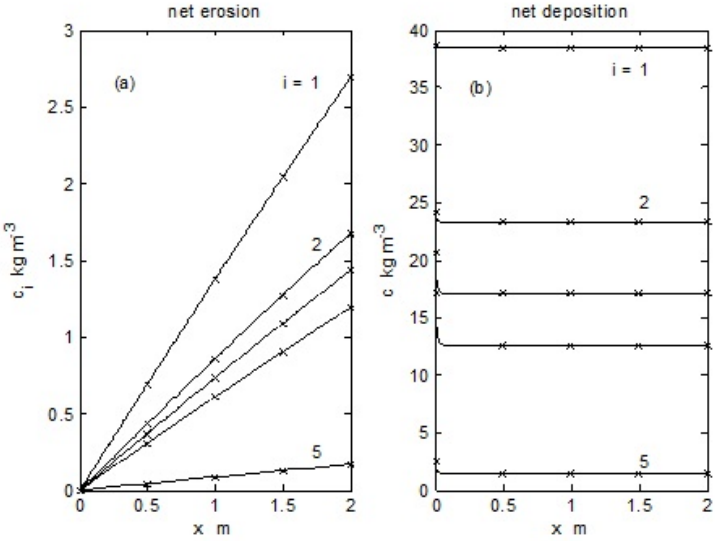

Figure 4.2: Steady state suspended sediment concentration $c_i(x)$ for (a) net erosion and (b) net deposition. Solid lines are for the method of lines while symbols are for the analytic solution from Sander *et al.* (2007a)

boundary conditions of

$$x = 0, \begin{cases} 0 < t < 15, & 30 < t < 45, & 60 < t < 75, & c_i = 0 \\ 15 < t < 30, & 45 < t < 60, & 75 < t < 90, & c_i = 103 p_i \ \ kg \ \ m^{-3} \end{cases} \tag{4.21}$$

are presented in Fig. (4.3) along with the numerical predictions for the parameter values listed in Table (4.1) and (4.2). Fig. (4.4) shows the breakdown of individual size classes for the numerical solution.

An interesting feature of the period 1 data in Fig. (4.3) is the appearance of an initial peak in sediment concentration near $t = 0$, which then declines to steady state by about 10 $mins$. Under rainfall-driven erosion it is common to see an early time peak due to the initial flushing of fine sediment (Sander *et al.*, 1996). However this non-monotonic behavior is usually not seen in runoff-driven erosion data, which generally show either a monotonic rise or fall in c towards steady state. Taking the initial condition of $c_i = 0$, $m_i = 0$ at $t = 0$, the predicted suspended sediment clearly shows a monotonic rise in $c(L, t)$ with a significant underestimation of the data for $t < 5$ $mins$, but with excellent agreement for $t > 5$ $mins$. Overall excellent agreement with the experimental data is found, with both the rate of rise and decline in c following the switching of the boundary conditions being very well captured by the HR model.

Polyakov and Nearing (2003) say that "preparation for consecutive runs included drying, replacing [the] top layer of soil and material lost from prior experiments with new sieved soil, breaking up clods and smoothing out irregularities in the surface". This suggests that the preparation of the bed prior to an experiment actually creates a layer of loose particles that can be regarded as forming part of a deposited layer, thus at $t = 0$, $m_i \neq 0$. Nonzero initial m_i's certainly permit this peak to be reproduced, but as we have no information on their possible values, this would simply result in increasing the number of parameters in the model for little gain. Additionally the physical importance of modeling the initial peak is negligible in terms of the overall match to the data in Fig. (4.3).

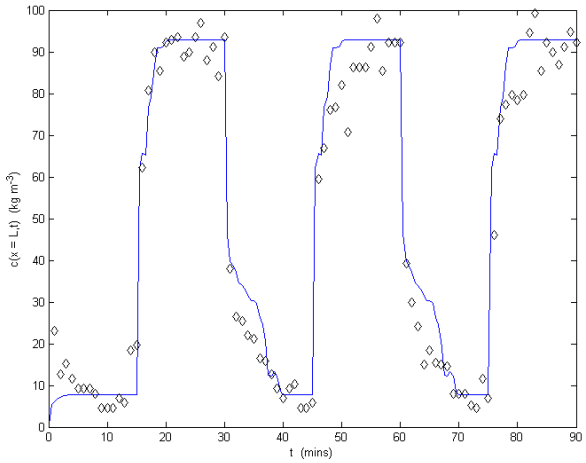

Figure 4.3: Comparison of experimental and predicted total suspended sediment concentration at the end of a 2 m rill. Data points (symbols) are from Polyakov and Nearing (2003)

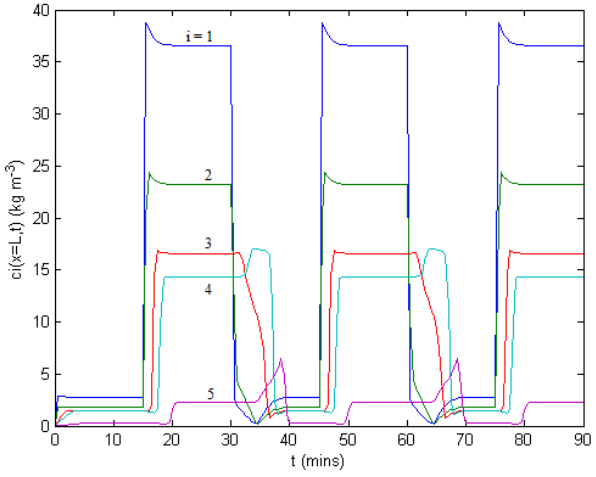

Figure 4.4: Predicted sediment concentration of each size class at the end of 2 m rill varying with time ($i = 1$ is the finest sediment and $i = 5$ is the largest sediment)

Fig. (4.5) to Fig. (4.16) display the variation in $c_i(x)$, $m_i(x)$ and $H(x)$ at various times during the experiment. The vertical line in the upper right hand diagram of each figure corresponds to the time of the spatial results presented in the another three diagrams of each figure. Consequently interpretations of the spatial results can be related back to which period of the net erosion or net deposition condition the results are from.

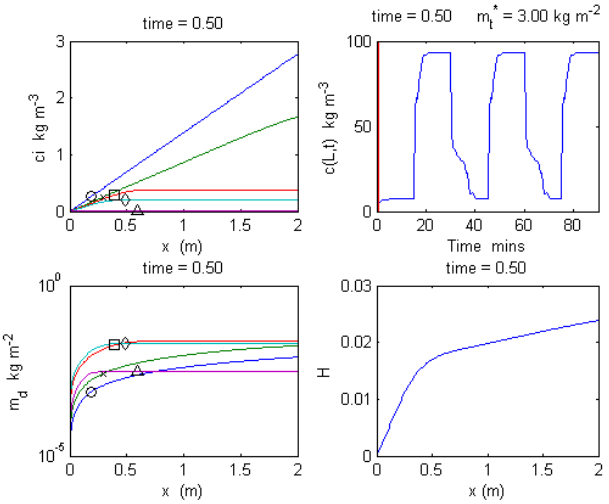

Figure 4.5: $t = 0.5$ minutes, blue line with circle ($i = 1$), green line with x-mark ($i = 2$), red line with square ($i = 3$), light blue line with diamond ($i = 4$), purple line with triangle ($i = 5$)

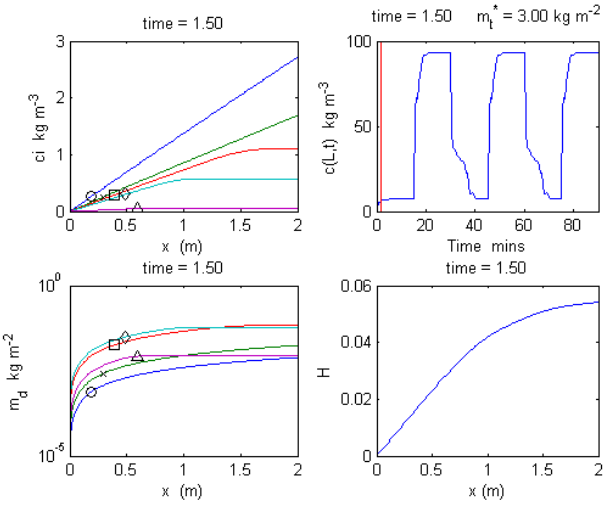

Figure 4.6: $t = 1.5$ minutes

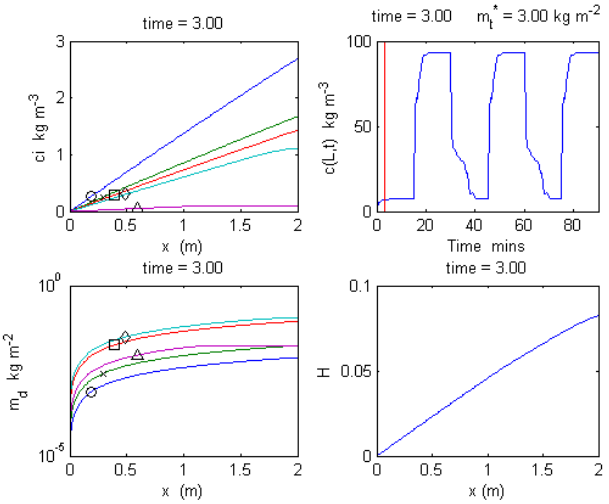

Figure 4.7: $t = 3$ minutes

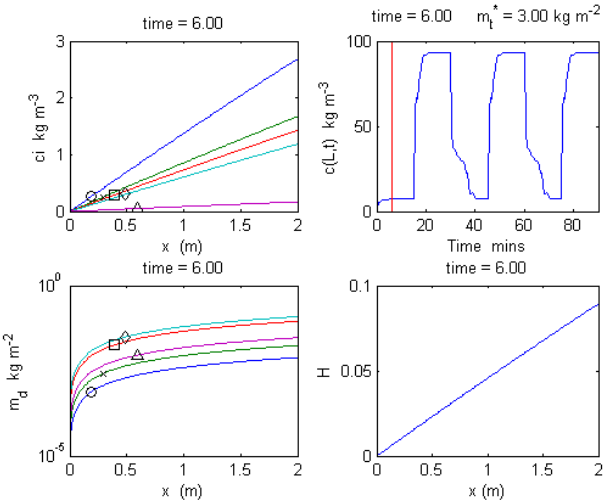

Figure 4.8: $t = 6$ minutes

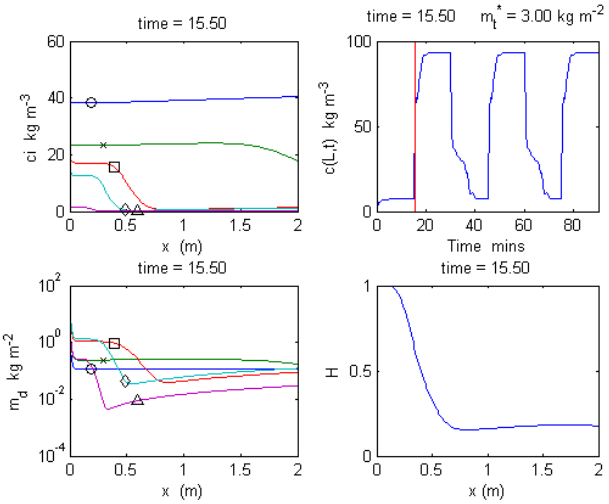

Figure 4.9: $t = 15.5$ minutes

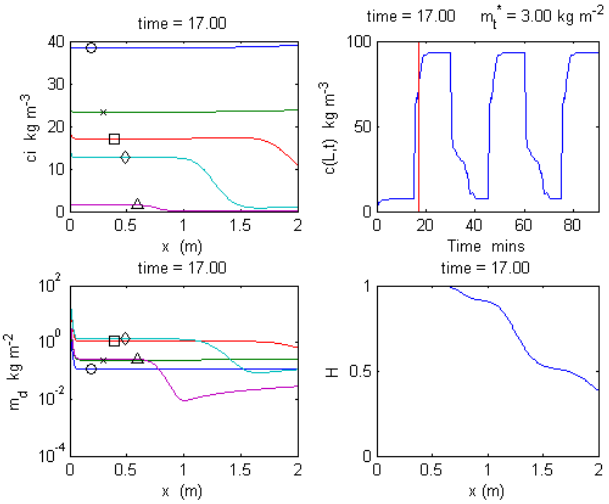

Figure 4.10: $t = 17$ minutes

At $t = 15\ \ mins$, the concentrations in each size class are $c_i = [2.6907\ \ 1.6745\ \ 1.4312\ \ 1.1879\ \ 0.1696]\ kg\ \ m^{-3}$ with the total concentration being $c = 7.15\ \ kg\ \ m^{-3}$. The corresponding concentrations at $t = 30\ \ mins$ are $c_i = [38.3731\ \ 23.3744\ \ 17.1351$

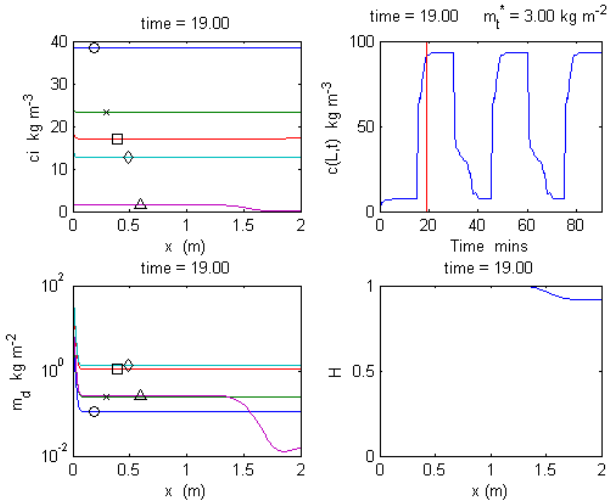

Figure 4.11: $t = 19$ minutes

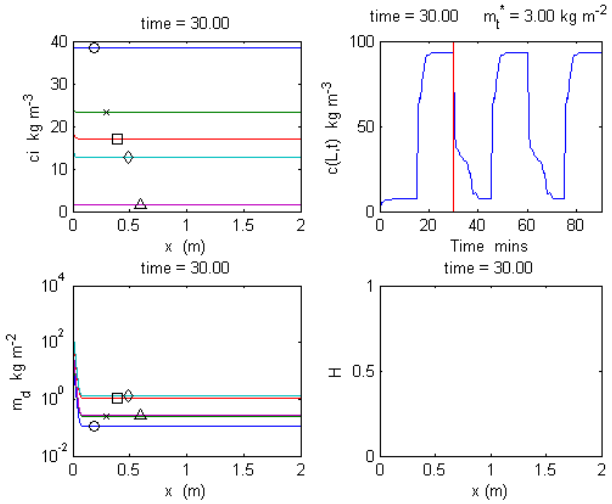

Figure 4.12: $t = 30$ minutes

12.6129 1.4957] $kg\ \ m^{-3}$ and $c = 93\ \ kg\ \ m^{-3}$. We note that these values are slightly different to data presented in Table (1) of Polyakov and Nearing (2003) due to the use of a single set of hydraulic parameters for both the net erosion and

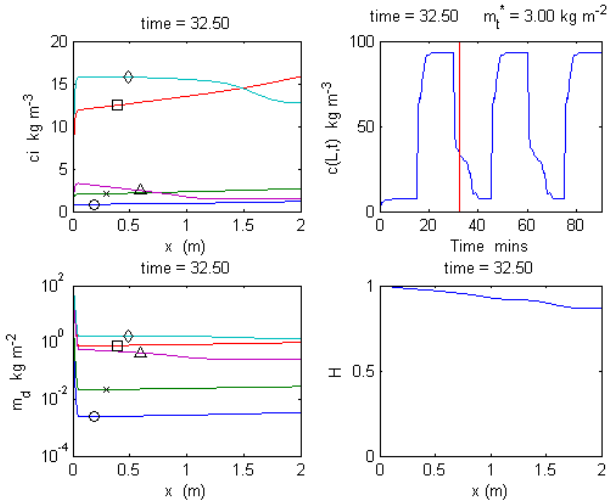

Figure 4.13: $t = 32.5$ minutes

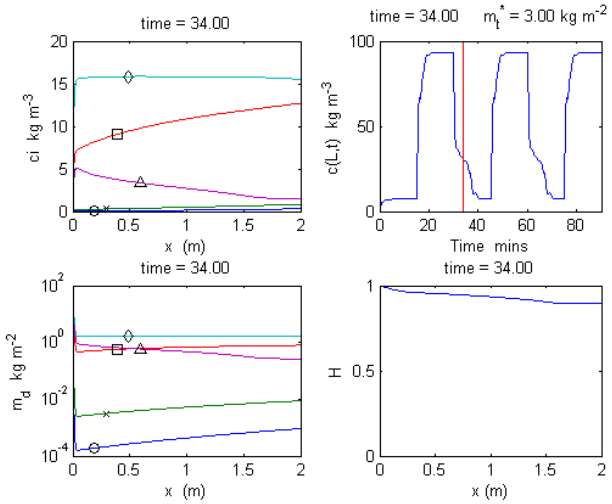

Figure 4.14: $t = 34$ minutes

net deposition periods even though their Table (2) showed that the flow width and depth varied significantly between the periods. Second, it is also clear from Fig. (1) and Fig. (2) of Polyakov and Nearing (2003) that the net deposition

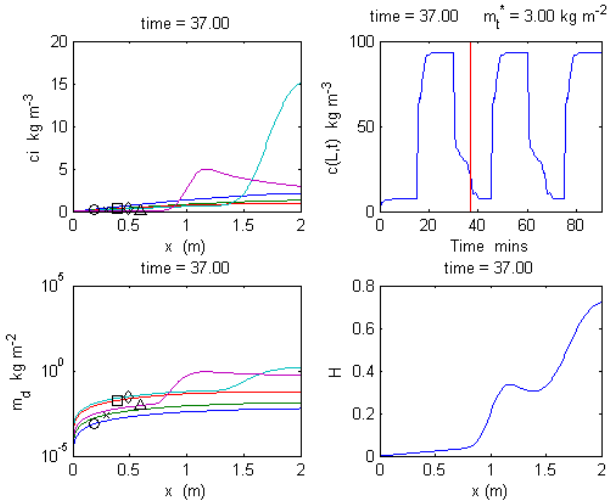

Figure 4.15: $t = 37$ minutes

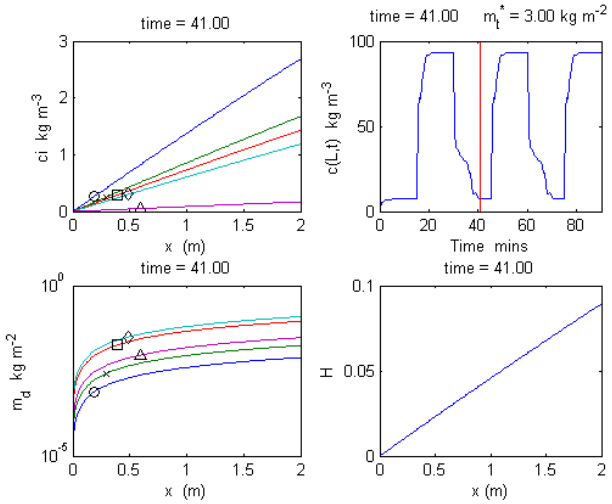

Figure 4.16: $t = 41$ minutes

steady state total suspended sediment concentrations are significantly different to those given in their Fig. (1) (90 $kg \quad m^{-3}$) and their Fig. (2) (approximately 80 $kg \quad m^{-3}$). The level of agreement with the data shown in Fig. (4.3) for

$c(L = 2m, t)$, which follows the excellent agreement to data for $c_i(x, \infty)$ found in Sander *et al.* (2007a), together appear to validate the HR model and suggest the conclusion that it can reproduce accurately detailed experimental data across a range of net erosion and net deposition conditions.

In Fig. (4.17) the spatial distribution of m_i at $t = 90\ \ mins$ is presented. Very similar looking distributions are found at the end of each depositional period (at 30 and 60 $mins$). The noticeable feature is the rapid rise in m_t to 1032 $\ kg\ \ m^{-2}$ near $x = 0$. This can be converted to a change in bed elevation z through $z = m_t/(1 - \phi)\rho_s$, where ϕ is the porosity of the deposited sediment. Taking $\rho_s = 2000kg\ \ m^{-3}$ with typical values of ϕ ranging from 0.4 to 0.6, then changes in the bed elevation near $x = 0$ would be between 86 and 129 $\ cm$. Clearly this is not physically realistic and therefore an additional transport mechanism that is not included in the HR model must be responsible for stopping the buildup of sediment around $x = 0$. Visual observations of soil particles rolling along the rill bed during the experiment suggest that one possible mechanism could be bed-load transport.

The Rouse (R_s) number given by

$$R_s = \frac{v_s}{\kappa_0 u^*} \tag{4.22}$$

where $u^* = (ghS_0)^{0.5}$ is the friction velocity, $\kappa_0 = 0.4$ is von Kármán's constant and v_s is the particle fall velocity has been applied widely in the literature to differentiate the modes of transport. These transport modes are given by suspended load for $R_s < 0.8$, saltating load for $0.8 < R_s < 2.5$ and bed-load for $R_s > 2.5$. Applying (4.22) to the five particle size classes of the Polyakov and Nearing (2003) data, results in $R_s = 0.15, 0.56, 3.4, 5.5$ and 9.4 for the smallest to the largest class respectively. This suggests that the two smallest sizes are transported in suspension with the next two size class saltating and the remaining larger class moving as bed-load. Since the largest size classes form the major contribution to m_t near $x = 0$, the Rouse number calculations do provide further

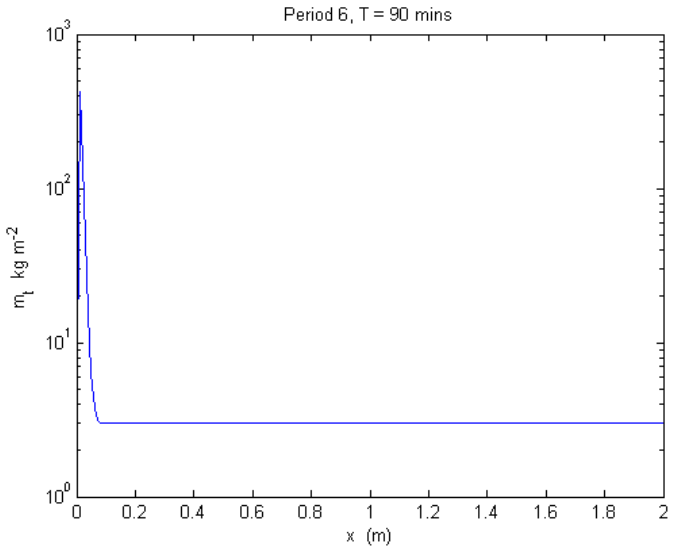

Figure 4.17: Spatial change of deposited sediment on rill bed

support for the reason that the HR model predicts a buildup of deposited sediment at the inflow boundary is due to the neglect of bed-load transport. In the following section the HR model is extended to include bed-load transport to see if this will improve the predictions around x = 0 for the net deposition periods.

4.2 Extension of HR Model to Bed-load Transport

From Bagnold (1966) the immersed bed-load transport rate is given by $q_b g(\rho_s - \rho)/\rho_s$ where q_b is the total bed-load transport rate ($kg\ \ m^{-1}\ \ s^{-1}$) that includes all sediment size classes. This must be proportional to the excess streampower available for transporting bed-load given by Hairsine and Rose (1992a) as $HF(\Omega - \Omega_{cr})$. The presence of H occurs because it is assumed that only the non-cohesive deposited layer is transported as bed-load, not the cohesive original soil. With both re-entrainment and bed-load occurring simultaneously, the excess stream power must be partitioned between the two processes. Denoting β as the fraction of the

excess stream power expended on bed-load transport then $1-\beta$ is expended on re-entrainment. Assuming that bed-load transport is non-selective with respect to sediment size and is proportional to the mass fraction m_i/m_t of the size class in the deposited layer, the rate of bed-load transport for each size class, q_{bi} is given by

$$q_{bi} = \beta \frac{F}{g}(\frac{\rho_s}{(\rho_s - \rho)})(\Omega - \Omega_{cr})H\frac{m_i}{m_t}. \tag{4.23}$$

The extended HR model is therefore

$$h\frac{\partial c_i}{\partial t} + q\frac{\partial c_i}{\partial x} = r_i + \widehat{r}_{ri} - d_i, \quad i = 1, 2, \ldots I, \tag{4.24}$$

and

$$\frac{\partial m_i}{\partial t} + \frac{\partial q_{bi}}{\partial x} = d_i - \widehat{r}_{ri}, \quad i = 1, 2, \ldots I, \tag{4.25}$$

where $\widehat{r}_{ri} = (1-\beta)r_{ri}$ is the reentrainment rate in the presence of bed-load transport. Note that from (4.4) and (4.23), alternative expressions for q_{bi} in terms of either r_{ri} or $\widehat{r}_{ri}$ are given by

$$q_{bi} = \beta h r_{ri} = \frac{\beta}{1-\beta} h \widehat{r}_{ri} \tag{4.26}$$

By summing equation (4.23) across the size classes, then for negligible Ω_{cr} it becomes equivalent to the model of Bagnold (1966) for

$$\frac{e_b}{\tan\mu} = \beta H F \tag{4.27}$$

where e_b is the efficiency of flow transporting the bed-load and $\tan\mu$ is the dynamic coefficient of internal friction. For a deposited layer providing complete coverage of the deposited layer and in the absence of re-entrainment, $H = 1$, $\beta = 1$ and $e_b/\tan\mu = F$. There is also a direct comparison of (4.23) to the bed-load transport model for mixed sediment given by (1) and (2) of Wilcock and Crowe (2003) written as

$$g(\frac{\rho_s}{\rho} - 1)\frac{q_{bi}}{\rho_s} = u^* \frac{\tau}{\rho} f(\tau_b/\tau_{ri})\frac{m_i}{m_t}, \tag{4.28}$$

where $u^* = \sqrt{\tau_b/\rho}$ is the shear velocity, τ_b is the bed shear stress, τ_{ri} is a reference bed shear stress for each size class, which may be replaced by the critical shear

stress τ_{ci}. Since $\Omega = \tau u$ where u is the average flow velocity and $e_b = u^*/u$, then from (4.23) and (4.28)

$$e_b f(\tau/\tau_{ci}) = \beta F H(1 - \Omega_{cr}/\Omega) \tag{4.29}$$

While the threshold stream power for each size class is likely to be different in reality (Wilcock, 1993), the Hairsine-Rose model assumes that the same value applies to all size classes. Steady state solutions to the extended model of (4.24) and (4.25) for both the net erosion and net deposition cases are now presented.

4.2.1 Steady State Solutions

Steady state net erosion and net deposition zones can be defined as regions where $m_t < m_t^*$ with $H < 1$ or $m_t \geq m_t^*$ with $H = 1$, respectively. Thus there exist two separate systems of equations for the steady state suspended sediment concentration within the two zones

(1) Net erosion zone ($m_t < m_t^*$, $H < 1$)

Under net erosion conditions, steady state suspended sediment conditions occur when both $\partial c_i/\partial t$ and $\partial m_i/\partial t$ are zero, thus (4.1) and (4.2) reduce to

$$q\frac{dc_i}{dx} = p_i\lambda(1 - \frac{m_t}{m_t^*}) + (1-\beta)\gamma\frac{m_i}{m_{t^*}} - v_i c_i \tag{4.30}$$

and

$$\frac{\beta\gamma}{m_t^*}h\frac{dm_i}{dx} = v_i c_i - (1-\beta)\gamma\frac{m_i}{m_t^*} \tag{4.31}$$

with

$$\lambda = \frac{F}{J}(\Omega - \Omega_{cr}). \tag{4.32}$$

(2) Net deposition zone ($m_t \geq m_t^*$, $H = 1$)

While $\partial c_i/\partial t$ must still be zero in a net deposition zone, $\partial m_i/\partial t$ is nonzero due to the continual build up of deposited sediment on the soil surface. Under these conditions (4.24) and (4.25) reduce to

$$q\frac{dc_i}{dx} = p_i\lambda(1 - \frac{m_t}{m_t^*}) + (1-\beta)\gamma\frac{m_i}{m_t} - v_i c_i \tag{4.33}$$

and

$$\frac{\partial m_i}{\partial t} + \beta\gamma h \frac{\partial}{\partial x}(\frac{m_i}{m_t}) = v_i c_i - (1-\beta)\gamma \frac{m_i}{m_t}. \tag{4.34}$$

If the suspended sediment concentration is to be independent of time, then the ratio m_i/m_t must depend solely on x. Thus defining

$$f_i(x) = \frac{m_i(x,t)}{m_t(x,t)} \tag{4.35}$$

then (4.34) can be written as

$$\frac{\partial m_i}{\partial t} = v_i c_i - (1-\beta)\gamma f_i - \beta\gamma h \frac{df_i}{dx}, \tag{4.36}$$

which for the long time asymptotic limit can be integrated to give to leading order

$$m_i(x,t) = [v_i c_i - (1-\beta)\gamma f_i - \beta\gamma h \frac{df_i}{dx}]t + \ldots \tag{4.37}$$

and

$$m_t(x,t) = (\sum_{i=1}^{I} v_i c_i - (1-\beta)\gamma)t + \ldots, \tag{4.38}$$

since $\sum_{i=1}^{I} f_i = 1$ by definition through (4.35).

By substituting (4.37) and (4.38) into (4.35) results in the following equation for $f_i(x)$

$$\beta\gamma h \frac{df_i}{dx} = v_i c_i - f_i \sum_{i=1}^{I} v_i c_i \tag{4.39}$$

with c_i determined from

$$q\frac{dc_i}{dx} = (1-\beta)\gamma f_i - v_i c_i. \tag{4.40}$$

Last, through (4.39), (4.37) can be simplified to

$$m_i(x,t) = f_i(\sum_{i=1}^{I} v_i c_i - (1-\beta)\gamma)t + \ldots \tag{4.41}$$

We also note that for $q_{bi} = 0$, $f_i = v_i c_i / \sum_{i=1}^{I} v_i c_i$ then (4.39) and (4.41) reduce to equations (12) and (14) of Sander *et al.* (2002).

4.2.2 Comparison with Experimental Data

In the presence of bed-load, sediment collected from the end of the flume is a combination of sediment transported in suspension and as bed-load. Consequently the experimental data in Fig.(4.3) would not be the actual total suspended sediment concentration c but an "effective" concentration C given by

$$C(L,t) = \sum_{i=1}^{I} (\frac{qc_i + q_{bi}}{q})_{x=L} = c(L,t) + \frac{1}{q} q_b(L,t), \tag{4.42}$$

where $q_b = \sum_{i=1}^{I} q_{bi}$.

It is only when $q_b = 0$ that C and c are equivalent and in general $c_i < C_i$. A comparison between the steady state data of Polyakov and Nearing (2003) and solutions of the steady state extended HR model are shown in Table (4.3) (parameters used here are from Table (2) in Sander *et al.* (2007a)).

The same level of excellent agreement for all size classes has been found as in Sander *et al.* (2007a) using the original HR model. A comparison between the time dependent experimental data and C (solid line) calculated from (4.24) to (4.26) and (4.42) is shown in Fig. (4.18), with the distribution of the total mass of sediment in the deposited layer after 90 $mins$ given in Fig. (4.19).

For these figures a value of $\beta = 0.75$ has been used while all other parameters remain the same as given in Table (4.1) except for F, which is taken as 0.3. Converting Fig. (4.19) into an elevation, now results in much more realistic values of $2 - 4$ mm. Including bed-load has significantly improved the physical plausibility of the calculated $m_t(x, 90)$, however it has come at the expense of poorer match to outflow data (Table (4.3) and Fig. (4.18)). Predicted steady state C's during the net deposition periods overestimate the data by approximately 10%. Net erosion periods though still have good agreement between theory and data. Improved agreement during net deposition periods can be obtained by altering parameter values to reduce C, but this leads to larger unphysical predictions of m_t near $x = 0$. Fig. (4.18) also gives a comparison between $C(L,t)$ and $c(L,t)$ for the duration of the experiment. The effect of bed-load transport is far more

Table 4.3: Measured and Predicted Sediment Concentration in each size class at the end of flume for $L = 2m$ and $L = 8m$

		C_i Net Erosion		C_i Net deposition	
Rill Length (m)	Size Class i	Measured[3]	Predicted	Measured[3]	Predicted
		$Q = 6L\ min^{-1}$			
2	1	3.5	4.57	48.2	35.39
	2	2.8	2.85	15.8	17.66
	3	2.3	2.43	7.1	4.50
	4	2.0	2.02	7.1	1.89
	5	0.3	0.29	0.8	0.12
8	1	13	7.93	37	35.39
	2	6.4	4.94	17.4	17.66
	3	5.7	4.22	10.2	4.50
	4	4.5	3.50	7.3	1.89
	5	0.6	0.50	1.5	0.12
		$Q = 9L\ min^{-1}$			
2	1	13.4	9.52	66.5	36.02
	2	7.9	5.92	21.8	18.77
	3	5.9	5.06	8.7	6.04
	4	5.9	4.20	9.8	2.89
	5	1.4	0.6	3.3	0.21
8	1	15.5	12.26	49.2	36.02
	2	12.4	7.63	30.2	18.77
	3	10.4	6.52	17.9	6.04
	4	10.9	5.41	11.2	2.89
	5	2.1	0.77	2.2	0.21

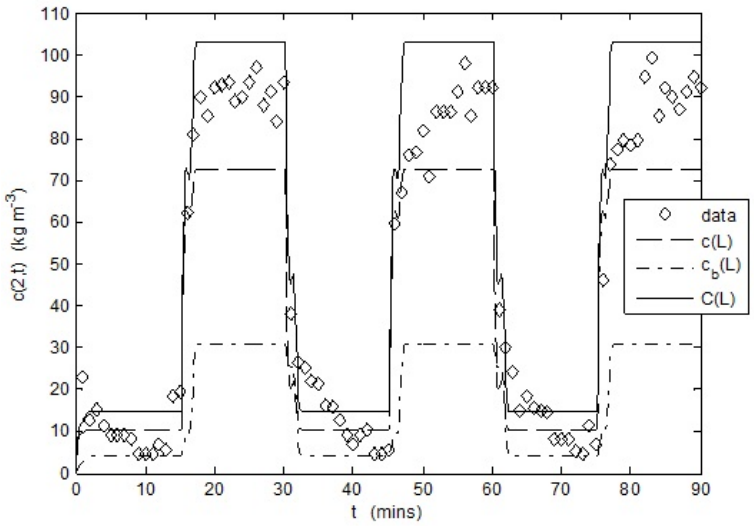

Figure 4.18: Comparison of experimental and predicted (including bed-load, $F = 0.3$, $\beta = 0.75$) total suspended sediment concentration at the end of a 2 m rill. Note $c(L) = c(x = L, t)$, $c_b(L) = c_b(x = L, t) = q_b(x = L, t)/q$ and $C(L) = C(x = L, t)$.

evident during net deposition periods as there is significantly more mass in the deposited layer available for transport compared with the net erosion period. This is apparent in Fig. (4.19) where $m_t(x, t)$ is compared at the end of erosion and deposition periods for $t = 75$ and 90 $mins$ respectively.

Note that the "wiggles" in the C and c curves in Fig. (4.18) are not due to numerical instability. These result from having discrete individual size classes to describe the sediment distribution, which travel down the flume in a series of waves with each size class having its own characteristic speed (see Fig. (4.5) to Fig. (4.10)). Evidence of these waves was first seen in numerical results presented in Fig. (3) of Hogarth *et al.* (2004). As the size of the particle increases it will spend more of its time on the soil bed and its corresponding wave speed down the slope will decrease (Hogarth *et al.*, 2004). Also, as the larger size size class waves exit the flume, there is a rapid increase in $c(L, t)$ and therefore $C(L, t)$. However

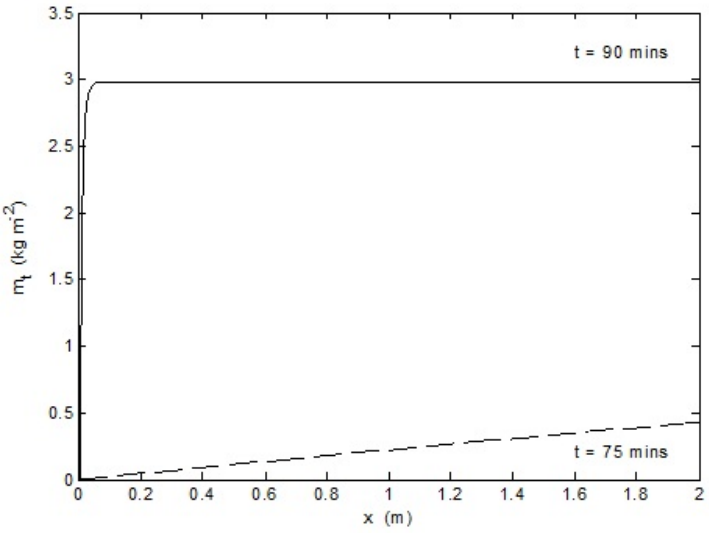

Figure 4.19: Spatial variation of the total mass of total sediment in the deposited layer at $t = 75$ and 90 $mins$ with $F = 0.3$ and $\beta = 0.75$.

for the smallest two size classes their concentrations decrease with distance behind the wave peak, causing a decrease in $C(L,t)$ over the very small time period it takes for this sediment to be flushed off the flume. This results in the small oscillations of the predicted $C(L,t)$ seen in Fig. (4.18). These waves begin to propagate at early times after the switching of boundary conditions at the start of each 15 $mins$ period, but they all quickly travel off the end of the flume resulting in steady state for each period being reached after only a couple of minutes.

The results of the simulations given in Fig. (4.18) and Fig. (4.19) clearly demonstrate that even with the addition of bed-load transport, the HR model is still not able to reproduce the data from Fig. (1) of Polyakov and Nearing (2003). The initial physical inconsistency emanates from the first net deposition period occurring for $15 < t < 30$ min where significant amounts of sediment are deposited near $x = 0$. The data in Table.(2) of Polyakov and Nearing (2003) give a Froude number (Fr) at $x = 2$ m of 1.1, indicating supercritical flow down the rill. Linear stability analysis of flow and bedform evolution in rivers (Fowler,

1997) shows that for $Fr > 1$, there is a very strong coupling between the flow velocity, flow depth and the bed morphology resulting in the formation of both dunes and anti-dunes. Previously published rill results from both experimental data (Nearing *et al.*, 1997) (Giménez and Govers, 2001) and numerical modeling (Lei and Nearing, 1998) have shown the importance of bed evolution on transport processes for Froude numbers near unity. Thus it would appear that a physically consistent model of the Polyakov and Nearing (2003) data given in their Fig. (1) requires the inclusion of bed morphology.

4.3 Asymptotic Analysis with Morphological Evolution

When morphological feedback is significant it is necessary to solve the full St Venant equations as both q and h can no longer be taken as constants. In addition another equation for mass conservation for the bed height z is required, for this we take a modified Exner model with bed-load. Taking a coordinate system with x aligned with the average bed slope and z being the distance normal to this slope from some arbitrary datum, then the full system of equations is given by Cao *et al.* (2002)

$$\frac{\partial h}{\partial t} + \frac{\partial q}{\partial x} = -\frac{\partial z}{\partial t}, \tag{4.43}$$

$$\frac{\partial q}{\partial t} + \frac{\partial}{\partial x}(\frac{q^2}{h} + \frac{gh^2}{2}) = gh(-\frac{\partial z}{\partial x} + S_0 - S_f) \tag{4.44}$$

and

$$\rho_s(1-\phi)\frac{\partial z}{\partial t} + \frac{\partial q_b}{\partial x} = \sum_{i=1}^{I}(d_i - r_{ri} - r_i) \tag{4.45}$$

where ϕ is the bed porosity, S_0 is the average bed slope over the length of the flume (being 7% for the data used in Table (4.1)) and S_f is the friction slope given by Manning's equation

$$S_f = \frac{n^2 q^2}{h^{10/3}} = \frac{\Omega}{\rho g q}. \tag{4.46}$$

An asymptotic analysis of the system of equations (4.43)-(4.45) and (4.24)-(4.26) is now performed in order to obtain a simplified system that still captures the dominate physical behavior as applied to the Polyakov and Nearing (2003) experiments. Define the non-dimensional variables by

$$\begin{array}{llll} \hat{x} = \frac{x}{x_0}, & \hat{t} = \frac{t}{t_0}, & \hat{c}_i = \frac{c_i}{c_0}, & \hat{h} = \frac{h}{h_0}, \quad \hat{z} = \frac{z}{h_0}, \\ \hat{q} = \frac{q}{q_0}, & \hat{q}_{bi} = \frac{q_{bi}}{q_{b0}}, & \hat{m}_i = \frac{m_i}{m_0}, & \hat{\Omega} = \frac{\Omega}{\Omega_0}, \quad \hat{v}_i = \frac{v_i}{v_0} \end{array} \tag{4.47}$$

where the "0" subscripts correspond to typical scaling values for the corresponding variable, and the circumflex denotes a non-dimensional quantity. Substituting for the variables in (4.47) and after making appropriate choices for the scaling values, the non-dimensional system of equations can be written as (after dropping the circumflex),

$$\varepsilon \frac{\partial h}{\partial t} + \frac{\partial q}{\partial x} = -\varepsilon \frac{\partial z}{\partial t}, \tag{4.48}$$

$$\varepsilon F_r^2 \frac{\partial q}{\partial t} + \frac{\partial}{\partial x}(F_r^2 \frac{q^2}{h} + \frac{h^2}{2}) = -h\frac{\partial z}{\partial x} + \delta h(1 - \frac{u^2}{h^{4/3}}), \tag{4.49}$$

$$\varepsilon \frac{\partial (hc_i)}{\partial t} + \frac{\partial (qc_i)}{\partial x} = Ap_i(1-H)(\Omega - \Omega_{cr}) + (\Omega - \Omega_{cr})\frac{H}{h}\frac{m_i}{m_t} - v_i c_i, \tag{4.50}$$

$$\frac{\partial m_i}{\partial t} + \alpha_1 \frac{\partial q_{bi}}{\partial x} = v_i c_i - (\Omega - \Omega_{cr})\frac{H}{h}\frac{m_i}{m_t}, \tag{4.51}$$

$$\frac{\partial z}{\partial t} + \alpha_1 \frac{\partial q_b}{\partial x} = \Sigma_{i=1}^{I}(v_i c_i - Ap_i(1-H)(\Omega - \Omega_{cr}) - (\Omega - \Omega_{cr})\frac{m_i}{m_t}), \tag{4.52}$$

$$q_{bi} = (\Omega - \Omega_{cr})H\frac{m_i}{m_t}, \quad \Omega = \frac{q^3}{h^{10/3}}, \tag{4.53}$$

$$H = \begin{cases} m_t & m_t \leq 1 \\ 1 & m_t > 1 \end{cases} \tag{4.54}$$

where

$$t_0 = \frac{h_0 \rho_s (1-\phi)}{v_0 c_0}, \quad x_0 = \frac{q_0}{v_0} = \frac{u_0 h_0}{v_0}, \quad c_0 = \frac{(1-\beta)F\Omega_0}{h_0 v_0 g}(\frac{\rho_s}{\rho_s - \rho}), \tag{4.55}$$

$$\varepsilon = \frac{x_0}{u_0 t_0} = \frac{c_0}{\rho_s(1-\phi)}, \quad \delta = \frac{x_0 S_0}{h_0} = \frac{x_0 n^2 u_0^3}{h_0^{7/3}}, \quad \Omega_0 = \frac{\rho g n^2 q_0^3}{h_0^{10/3}}, \quad A = \frac{h_0 g(\rho_s - \rho)}{J\rho_s}, \tag{4.56}$$

$$\alpha_1 = \frac{q_{b0}}{q_0 c_0} = \frac{\beta}{1-\beta}\frac{v_0}{u_0}, \quad v_0 = \sum_{i=1}^{I} p_i v_i, \quad q_{b0} = \frac{\beta}{1-\beta} h_0 v_0 c_0, \quad m_0 = h_0 \rho_s (1-\phi) = m_t^*. \tag{4.57}$$

Since it is the effect of bed morphology on sediment transport that is been investigated in the above analysis, then the time scale t_0 is chosen from the bed equation of (4.52). The spatial scale x_0 is chosen from the suspended sediment equation (4.51) and represents the average length the suspended particles are transported before falling onto the bed. The concentration scale c_0 is chosen by balancing the reentrainment and deposition rate terms in (4.51). The reentrainment term rather than the entrainment source term is used in this balance as deposited sediment is easier to reentrain than the original soil. The fall velocity scale v_0 is an average fall velocity for the given sediment distribution, and the deposited mass scale is based on the mass of sediment required for $H = 1$ while δ arises from a balance between the average bed slope and the bed friction term. All other scaling parameters then follow immediately.

From the data of Polyakov and Nearing (2003) then $q_0 = q$ and $h_0 = h$ from which u_0 and Manning's n can be computed. Since the sediment transport appeared to be partitioned between suspension and bed-load we take $\beta = 0.5$. Then, using an indicative value for the bed porosity of $\phi = 0.5$ along with the other parameter values as given in Tables (4.1) and (4.2), the scaling parameters in (4.55) to (4.57) are given by

$$n = 0.039, \quad c_0 = 41.5kg/m^3, \quad x_0 = 23.3mm, \quad t_0 = 2.2s, \quad v_0 = 0.05m/s,$$

$$m_0 = 4.4kg, \quad q_{s0} = q_0 c_0 = 0.05kg/m/s, \quad q_{b0} = 0.01kg/m/s, \quad \Omega_0 = 0.79W/m^2,$$

$$A = 0.001, \quad \alpha_1 = 0.24, \quad \delta = 0.29, \quad \varepsilon = 0.05, \quad F_r = 0.9.$$

It is worth noting that the order of magnitude of these values is quite consistent with the Polyakov and Nearing experiments. Also the length scale x_0, which corresponds to the size of oscillations in bedforms is remarkably consistent with the data shown in Fig. (6) of Gim*é*nez and Govers (2001) (refer to Fig. (4.20)). Since ε, A and Ω_{cr} are all $<< 1$ with δ and α_1 also small then by taking the limits

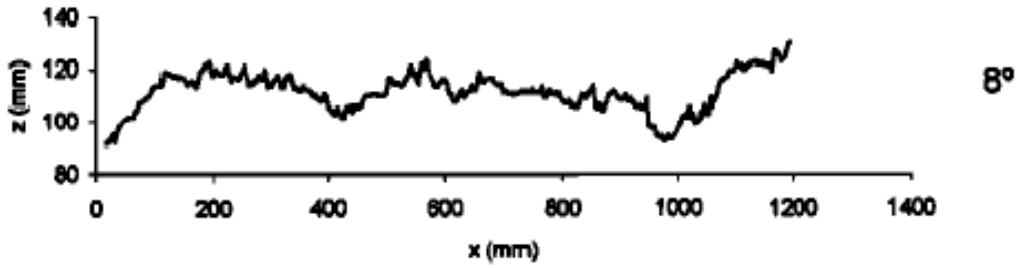

Figure 4.20: Soil surface profiles corresponding to slope of 8° and a discharge of 400 $L\ \ h^{-1}$ (from Giménez and Govers (2001))

of $\varepsilon \to 0$, $\delta \to 0$, $A \to 0$, $\alpha_1 \to 0$, $\Omega_{cr} \to 0$ the leading order equations are

$$\frac{\partial q}{\partial x} = 0, \tag{4.58}$$

$$\frac{\partial}{\partial x}(F_r^2 \frac{q^2}{h} + \frac{h^2}{2}) = -h\frac{\partial z}{\partial x}, \tag{4.59}$$

$$\frac{\partial (qc_i)}{\partial x} = \Omega \frac{H}{h}\frac{m_i}{m_t} - v_i c_i, \tag{4.60}$$

$$\frac{\partial m_i}{\partial t} = v_i c_i - \Omega \frac{H}{h}\frac{m_i}{m_t}, \tag{4.61}$$

$$\frac{\partial z}{\partial t} = \sum_{i=1}^{I} v_i c_i - \frac{H}{h}\Omega. \tag{4.62}$$

From (4.58) we have $q = uh = 1$ (as q has been scaled appropriately), thus the other equations become

$$(F_r^2 u - \frac{1}{u^2})\frac{\partial u}{\partial x} = -\frac{\partial z}{\partial x}, \tag{4.63}$$

$$\frac{\partial c}{\partial x} = \frac{H}{h}\Omega - \Sigma v_i c_i = -\frac{\partial z}{\partial t}. \tag{4.64}$$

since $z = \sum m_i = m_t$ and $H = z$ for $z \leq 1$. The above system shows that to leading order it is the feedback on flow hydraulics resulting from the evolution of the rill bed that has a substantial affect on the quantity of sediment transported.

As boundary conditions are cycled between net erosion and net deposition there are rapid and substantial changes in the local bed slopes throughout the length of the rill. This also results not only in considerable variation of flow velocity and discharge with distance, but also in the total sediment load transported down the rill. In particular, at the entry to the rill ($x = 0$), there will be a region where the greatest spatial and temporal changes in bed morphology occur, either as a result of increased erosion during the periods of clear water inflow, or from increased deposition during the periods of sediment-laden inflow. The inclusion of bed evolution counters the buildup of sediment at $x = 0$ under net deposition conditions. This is achieved by allowing the local increase in bedslope to feed back into the momentum equation that results in a locally increased flow velocity, fluid flux and stream power. As a consequence there is a greater re-entrainment rate resulting in a much greater sediment transport at the boundary that stops the excessive buildup of deposited sediment. The asymptotic analysis supports the numerical simulations by Lei and Nearing (1998) that not only confirm the sensitivity of bed morphology to regions near the upstream boundary but they also show that for the reliable prediction of spatial variation in erosion and deposition on hillslopes, interactions and feedback between flow hydraulics and bed morphology need to be accounted for.

4.4 Conclusions

It is common for both field-based and laboratory-based studies to validate soil erosion models against measured data collected at a single point through time. The study has demonstrated that the matching of both the spatial and temporal suspended sediment concentrations is not a sufficiently demanding test for validating an erosion model. This same conclusion was reached the highly simplified analytical model of Barry *et al.* (2010), who considered rainfall-driven erosion. The analysis presented here shows that accurate predictions of outflow with the

HR model could be obtained even though potentially important transport mechanisms had been ignored. The extension of the HR model to include a bed-load transport term improved the overall model performance, but it was still unable to obtain physically acceptable agreement for both the exported sediment load data and the spatial and temporal distribution of deposited sediment in the flume. Thus while transport by bed-load is significant in many flow situations, the numerical simulations showed that the addition of this mechanism is not sufficient for the HR model to explain the Polyakov and Nearing (2003) data. Finally, it is shown through an asymptotic analysis that the spatial and temporal interplay between the flow hydraulics and the bed morphology can be particularly important in determining and controlling sediment discharge and that in the case of the Polyakov and Nearing experiments it is far more influential than bed-load. It is concluded that erosion models may need to incorporate bed morphological effects, especially when applied at the scale where rilling predominates, so that they are able to capture the key physical mechanisms controlling the flow and associated sediment transport.

CHAPTER 5

Soil Erosion with Kinematic Flow

5.1 Introduction

In Chapter 4 solutions to the time dependent HR model were given under conditions of both flow depth h and flux q being constant. In this Chapter, the more realistic and naturally occurring conditions of h and q being both spatial and time dependent and governed by the kinematic wave equation is considered. Thus this chapter therefore looks at developing and analysing solutions to the system

$$\frac{\partial h}{\partial t} + \frac{\partial q}{\partial x} = R, \tag{5.1}$$

$$\frac{\partial (hc_i)}{\partial t} + \frac{\partial (qc_i)}{\partial x} = e_i + e_{di} + r_i + r_{ri} - d_i, \tag{5.2}$$

$$\frac{\partial m_i}{\partial t} = d_i - e_{di} - r_{ri}, \tag{5.3}$$

subject to the initial and boundary conditions

$$\begin{array}{llll} t = 0, & h = 0, & c_i = 0, & m_i = 0, \\ x = 0, & h = 0, & c_i = 0. & \end{array} \tag{5.4}$$

As a reminder, $q = Kh^m$ and $R = P - G$ where $P(t)$ and $G(t)$ are the rainfall and infiltration rates respectively. The rainfall detachment of original soil e_i and the rainfall re-detachment of deposited soil e_{di} respectively, are given by

$$e_i = p_i a P(1 - H), \tag{5.5}$$

$$e_{di} = a_d P \frac{m_i}{m_t} H, \tag{5.6}$$

where a is the rainfall detachability for bare soil and a_d is the rainfall detachability for deposited soil layer. Both a and a_d are flow depth dependent and given by (Hairsine and Rose, 1991)

$$a = a_0,\ a_d = a_{d0},\ h < h_0, \tag{5.7}$$

$$a = a_0(\frac{h_0}{h})^{\delta},\ a_d = a_{d0}(\frac{h_0}{h})^{\delta},\ h > h_0, \tag{5.8}$$

where h_0 is approximately three raindrop diameters and δ is a constant. The deposition rate of sediment $d_i = v_i c_i$ as used in Chapter 4, with the entrainment and re-entrainment terms described by equation (4.3) and (4.4) respectively. Note that bed-load transport will not considered any further.

In equation (5.4), we equate $t = 0$ with the time of the commencement of rainfall and thus the time that overland flow begins, or ponding time, is denoted by t_p. Once rainfall begins, and prior to runoff generation ($0 \leq t \leq t_p$), detachment of original cohesive soil is occurring and therefore the deposited layer is actually undergoing development. Consequently in order to solve (5.2) and (5.3) for $t > tp$ then both c_i and m_i at ponding time must first be known.

5.2 Development of Deposited Layer prior to Ponding Time

During the period $t < t_p$, both h and q are zero and assuming that rainfall and infiltration are distributed uniformly down the slope, then there are no spatial detachment gradients. As the left hand side of (5.2) is zero, we can write (since $r_i = r_{ri} = 0$ also)

$$d_i - e_{di} = e_i, \tag{5.9}$$

and (5.3) becomes ($a = a_0$ for $h = 0$)

$$\frac{dm_i}{dt} = e_i = p_i a_0 P(1 - H). \tag{5.10}$$

Summing (5.3) and noting $H = \frac{m_t}{m_t^*}$, the solution for H can be obtained as

$$H(t) = 1 - exp(-\frac{a_0 P}{m_t^*} t), \tag{5.11}$$

which at ponding time gives

$$H(t_p) = 1 - exp(-\frac{a_0 P}{m_{tp}^*} t_p). \tag{5.12}$$

As mentioned before the detachment process is dependent on the cohesiveness of the original soil, it is not a size class selective process. Since there is no water layer to transport detached particles, the distribution of all size classes to H must be in proportion to the original distribution in the cohesive soil, therefore $m_i = p_i m_t = p_i H m_t^*$ and therefore

$$m_i = p_i m_t^* [1 - exp(-\frac{a_0 P}{m_t^*} t)]. \tag{5.13}$$

Thus, at ponding time the distribution of masses in the deposited layer can be written as

$$m_i = p_i m_t^* [1 - exp(-\frac{a_0 P}{m_t^*} t_p)]. \tag{5.14}$$

Note that equivalent forms to (5.11) and (5.13) are derived by eq (7) and (6) in Heilig *et al.* (2001) for a constant P, though its derivation interpretation is different.

Combining (5.1) and (5.2), we have for $t \leq t_p$

$$h\frac{\partial c_i}{\partial t} + q\frac{\partial c_i}{\partial x} = e_i + e_{di} - d_i - Rc_i \tag{5.15}$$

and since h and q are still zero at ponding time, the left hand side of (5.15) is zero. Then c_i at $t = t_p$ can be solved and expressed by

$$c_i(x,t_p) = \frac{1}{R+v_i}(e_i + e_{di}) = \frac{p_i}{R+v_i}P[a_0 - (a_0 - a_{d0})H(t_p)]. \tag{5.16}$$

Alternatively (5.16) can be obtained by considering the characteristic equation from (5.15) and requiring only non-singular solutions. Even though c_i is non-zero at $t = t_p$, the mass flux of sediment given by qc_i is zero. Thus there is no physical inconsistency occuring by having non-zero initial concentration.

Having determined the evolution of the deposited layer prior to ponding time, then the solution of (5.1) to (5.3) is sought subject to the following initial and boundary conditions (i.e. replacing (5.42))

$$\begin{array}{llll} t = t_p, & h = 0, & c_i = c_{ip}, & m_i = m_{ip}, \\ x = 0, & h = 0, & c_i = \psi(t), & \end{array} \tag{5.17}$$

where c_{ip} and m_{ip} are given by (5.16) and (5.14) respectively, and $\psi(t)$ is given by (5.16) with $H(t_p)$ replaced by $H(t)$ as give by (5.11), i.e.

$$\psi(t) = \frac{p_i P}{R+v_i}[a_0 - (a_0 - a_{d0})H(t)]. \tag{5.18}$$

Since $h = 0$ at $x = 0$ for all time, then H and therefore c_i continue to evolve with time to steady state.

5.3 Analytical Expansion around Ponding Time

In general it is not possible to solve (5.1) to (5.3) analytically and numerical methods must be used. Due to $h = 0$ at $t = t_p$, the numerical solution can not start integrating (5.15) from $t = t_p$, there will be a numerically indeterminate 0/0 for the right side of (5.15). Thus, it is necessary to find an analytical expansion for the solution for small $t - t_p$. First, define a new time by

$$\tau = t - t_p. \tag{5.19}$$

so that expansion for τ around zero can be sought. The case of R constant will be considered first and then R time dependent.

5.3.1 R Constant

As it was presented in chapter 3, for constant R and $h_i = h_s = 0$ (h_i here is the initial value of h at $t = t_p$), the solution to the kinematic equation for $h(x,t)$ is given by

$$h = (\frac{Rx}{K})^{1/m}, \quad x \leq KR^{m-1}\tau^m; \tag{5.20}$$

$$h = R\tau, \quad x \geq KR^{m-1}\tau^m. \tag{5.21}$$

The characteristic emanating from the origin for the kinematic equation (5.1) is given by

$$x = m\int_0^\tau \frac{q}{h}dt, \tag{5.22}$$

while the characteristic coming from the origin for (5.15) is

$$x = \int_0^\tau \frac{q}{h}dt. \tag{5.23}$$

Consequently for a given time the characteristic from the origin has penetrated further into the domain for the kinematic equation then for (5.15). Since h is only time dependent for x greater than the right hand side of (5.22) (or (5.21) for R constant), then by defining a numerical grid with a step length of $\Delta x > KR^{m-1}\varepsilon^m$ for small time $\tau = \varepsilon$, then both c_i and m_i will also be independent of space across the entire grid (except at $x = 0$). Thus on this grid and for $x > \Delta x$, (5.2) and (5.3) can be replaced with (since $h < h_0$ and $\Omega < \Omega_{cr}$ for $\tau = \varepsilon$)

$$h\frac{dc_i}{d\tau} = p_i a_0 P(1 - \frac{m_t}{m_t^*}) + a_{d0}P\frac{m_i}{m_t^*} - (v_i + R)c_i, \tag{5.24}$$

$$\frac{dm_i}{d\tau} = v_i c_i - a_{d0}P\frac{m_i}{m_t^*}. \tag{5.25}$$

In particular, the following power series expansion in τ for c_i and m_i is looked for

$$c_i(t) = c_i^0 + c_i^1\tau + c_i^2\tau^2 + \cdots = \sum_{j=0}^{n} c_i^j \tau^j, \tag{5.26}$$

$$m_i(t) = m_i^0 + m_i^1\tau + m_i^2\tau^2 + \cdots = \sum_{j=0}^{n} m_i^j \tau^j, \tag{5.27}$$

$$m_t(t) = m_t^0 + m_t^1\tau + m_t^2\tau^2 + \cdots = \sum_{j=0}^{n} m_t^j \tau^j \tag{5.28}$$

where c_i^0 and m_i^0 are given by (5.16) and (5.14) and $m_t^j = \sum_{i=1}^{I} m_i^j$. The superscripts on c_i and m_i correspond to the constant coefficients of the powers in τ.

Substituting (5.26) and (5.27) into (5.25) gives

$$\begin{aligned} \sum_{j=1}^{n} j m_i^j \tau^{j-1} &= \sum_{j=0}^{n} v_i c_i^j \tau^j - \sum_{j=0}^{n} \frac{a_{d0} P}{m_t^*} m_i^j \tau^j \\ &= \sum_{j=1}^{n} (v_i c_i^{j-1} - \frac{a_{d0} P}{m_t^*} m_i^{j-1}) \tau^{j-1} \end{aligned} \tag{5.29}$$

Thus the m_i^j are given by the recurrence relation

$$m_i^j = \frac{1}{j}(v_i c_i^{j-1} - \frac{a_{d0} P}{m_t^*} m_i^{j-1}),\ j = 1, 2, \cdots \tag{5.30}$$

Substituting (5.26) to (5.28) into (5.24) gives

$$\begin{aligned} \sum_{j=1}^{n} j R c_i^j \tau^j &= p_i a_0 P - p_i a_0 P H(t_p) - (v_i + R) c_i^0 + a_{do} P p_i H(t_p) \\ &\quad - \frac{p_i a_0 P}{m_t^*} \sum_{j=1}^{n} m_t^j \tau^j - (v_i + R) \sum_{j=1}^{n} c_i^j \tau^j + \frac{a_{d0} P}{m_t^*} \sum_{j=1}^{n} m_i^j \tau^j \\ &= \sum_{j=1}^{n} [\frac{a_{d0} P}{m_t^*} m_i^j - \frac{p_i a_0 P}{m_t^*} m_t^j - (v_i + R) c_i^j] \tau^j. \end{aligned} \tag{5.31}$$

As the $j = 0$ term satisfies (5.16) it does not appear in (5.31). Thus (5.31) can be rearranged and solved for c_i^j as

$$c_i^j = \frac{P}{m_t^*}(\frac{a_{d0}m_i^j - p_i a_0 m_t^j}{v_i + (1+j)R}),\ j = 1, 2, \cdots \tag{5.32}$$

5.3.2 R Time Dependent and $R = P$

For R dependent on t, we take a simple case which assumes the infiltration rate $G = 0$. Physically this often occurs in laboratory based soil erosion flumes when the soil is pre-saturated prior to the commencement of rainfall and the base of the flume is impermeable. Thus, $R = P$ and we use the form of the excess rainfall rate as

$$R(\tau) = P(\tau) = R_0 e^{-b\tau}(1 - e^{-b\tau}) \tag{5.33}$$

which has a single peak at $t = \frac{ln2}{b}$ and falls off to zero for large times. For this case, runoff generates as soon as the rainfall starts. Therefore, $tp = 0$ and $\tau = t$.

As presented in chapter 3, the solutions to the kinematic flow equation with $R(\tau)$ in the form of (5.33) are

$$h = \frac{R_0}{b}(\frac{1}{2} - e^{-b\tau} + \frac{1}{2}e^{-2b\tau}),\ \ x \geq mK\int_0^\tau h^{m-1}dt, \tag{5.34}$$

$$h = \frac{R_0}{b}(be^{-t_0} - e^{-b\tau} - \frac{1}{2}e^{-2bt_0} + \frac{1}{2}e^{-2b\tau}),\ \ x = mK\int_{t_0}^\tau h^{m-1}dt. \tag{5.35}$$

Expanding R and h from (5.34) for τ near zero shows that they go like

$$R(\tau) = R_0(b\tau - \frac{3}{2}b^2\tau^2 + \frac{7}{6}b^3\tau^3 - \frac{15}{24}b^4\tau^4 + \cdots), \tag{5.36}$$

$$h(\tau) = \frac{R_0}{2}(b\tau^2 - b^2\tau^3 + \frac{7}{12}b^3\tau^4 - \frac{1}{4}b^4\tau^5 + \cdots), \tag{5.37}$$

for

$$x > mK(\frac{Rob}{2})^{m-1}[\frac{\tau^{2m-1}}{2^{m-1}} - \frac{(m-1)b}{2m}\tau^{2m} + \ldots]. \tag{5.38}$$

If $\triangle x$ is chosen to be greater than the right hand side of (5.38), then on this grid h, c_i and m_i will again be independent of x. Thus, substituting (5.26) to (5.28), (5.36) and (5.37) into (5.24) and (5.25) results in

$$
\begin{aligned}
& \frac{R_0}{2}(b\tau^2 - b^2\tau^3 + \frac{7}{12}b^3\tau^4)(c_i^1 + 2c_i^2\tau + 3c_i^3\tau^2) \qquad (5.39)\\
= \;& p_i a_0 R_0(b\tau - \frac{3}{2}b^2\tau^2 + \frac{7}{6}b^3\tau^3 - \frac{5}{8}b^4\tau^4)(1 - \frac{m_t^0}{m_t^*} - \frac{m_t^1}{m_t^*}\tau - \frac{m_t^2}{m_t^*}\tau^2 - \frac{m_t^3}{m_t^*}\tau^3)\\
& + a_{d0}R_0(b\tau - \frac{3}{2}b^2\tau^2 + \frac{7}{6}b^3\tau^3 - \frac{5}{8}b^4\tau^4)(\frac{m_i^0}{m_t^*} + \frac{m_i^1}{m_t^*}\tau + \frac{m_i^2}{m_t^*}\tau^2 + \frac{m_i^3}{m_t^*}\tau^3)\\
& - (v_i + R_0(b\tau - \frac{3}{2}b^2\tau^2 + \frac{7}{6}b^3\tau^3) - \frac{5}{8}b^4\tau^4)(c_i^0 + c_i^1\tau + c_i^2\tau^2 + c_i^3\tau^3 + c_i^4\tau^4),
\end{aligned}
$$

and

$$
\begin{aligned}
& m_i^1 + 2m_i^2\tau + 3m_i^3\tau^2 + 4m_i^4\tau^3\\
= \;& v_i(c_i^0 + c_i^1\tau + c_i^2\tau^2 + c_i^3\tau^3)\\
& - a_{d0}R_0(b\tau - \frac{3}{2}b^2\tau^2 + \frac{7}{6}b^3\tau^3)(\frac{m_i^0}{m_t^*} + \frac{m_i^1}{m_t^*}\tau + \frac{m_i^2}{m_t^*}\tau^2). \qquad (5.40)
\end{aligned}
$$

Since there is not constant term on the left hand side of (5.39), $v_i c_i^0$ must be zero. Hence c_i^0 is zero which is in agreement with (5.16) for $R = P = 0$ at $t = t_p$. This results in $m_i^1 = 0$ from (5.40).

Balancing the leading order terms of τ, τ^2 and τ^3 in (5.39) and (5.40) leads to

$$
\begin{aligned}
c_i^1 &= \frac{1}{v_i}p_i a_0 R_0 b(1 - \frac{m_t^0}{m_t^*}) + \frac{1}{v_i}a_{d0}R_0 b\frac{m_i^0}{m_t^*}\\
&= \frac{1}{v_i}p_i R_0 b[a_0(1 - H_0) + a_{d0}H_0], \qquad (5.41)
\end{aligned}
$$

and

$$
\begin{aligned}
m_i^2 &= \frac{1}{2}(v_i c_i^1 - a_{d0}R_0 b\frac{m_i^0}{m_t^*})\\
&= \frac{1}{2}(v_i c_i^1 - a_{d0}R_0 b p_i H_0), \qquad (5.42)
\end{aligned}
$$

where $H_0 = H(t = 0) = \frac{m_t^0}{m_t^*}$.

Similarly, we can solve c_i^2, c_i^3, c_i^4, m_i^3 and m_i^4

$$\begin{aligned} c_i^2 &= -\frac{3R_0 b}{2v_i}\{p_i b[a_0(1-H_0)+a_{d0}H_0]+c_i^1)\} \\ &= -\frac{3R_0 b^2 p_i}{2v_i}[a_0(1-H_0)+a_{d0}H_0](\frac{R_0}{v_i}+1), \end{aligned} \tag{5.43}$$

$$\begin{aligned} c_i^3 &= \frac{1}{v_i}\{2b^2R_0c_i^1-2bR_0c_i^2+\frac{7}{6}b^3p_iR_0[a_0(1-H_0)+a_{d0}H_0] \\ &\quad +R_0bp_i(a_0-a_{d0})(\frac{3}{2}b\frac{m_t^1}{m_t^*}-\frac{m_t^2}{m_t^*})\}, \end{aligned} \tag{5.44}$$

$$m_i^3 = \frac{1}{3}(v_ic_i^2+\frac{3}{2}a_{d0}R_0b^2p_iH_0), \tag{5.45}$$

$$\begin{aligned} c_i^4 &= \frac{1}{v_i}\{-\frac{35}{24}R_0b^3c_i^1+\frac{5}{2}R_0b^2c_i^2-\frac{5}{2}R_0bc_i^3 \\ &\quad +p_iR_0b(a_0-a_{d0})(\frac{5}{8}b^3H_0-\frac{7}{6}b^2\frac{m_t^1}{m_t^*}+\frac{3}{2}b\frac{m_t^2}{m_t^*}-\frac{m_t^3}{m_t^*}) \\ &\quad -\frac{5}{8}p_iR_0b^4a_0\}, \end{aligned} \tag{5.46}$$

$$m_i^4 = \frac{1}{4}[v_ic_i^3-a_{d0}R_0bp_i(\frac{7}{6}b^2H_0-\frac{3}{2}b\frac{m_t^1}{m_t^*}+\frac{m_t^2}{m_t^*})], \tag{5.47}$$

Then, for $R(\tau)=P(\tau)=R_0e^{-b\tau}(1-e^{-b\tau})$ the short time expansion for $c_i(x,\tau)$ and $m_i(x,\tau)$ can be expressed as below with the coefficients given above.

$$c_i(x,\tau)=c_i^1\tau+c_i^2\tau^2+c_i^3\tau^3+c_i^4\tau^4+O(\tau^5), \tag{5.48}$$

$$m_i(x,\tau)=m_i(x,0)+m_i^2\tau^2+m_i^3\tau^3+m_i^4\tau^4+O(\tau^5). \tag{5.49}$$

5.4 Numerical Solution after Ponding Time

The MOL is still used here to solve kinematic wave approximation plus the full HR model for $t > t_p$. The matrix system for (5.1) to (5.3) is written as

$$\frac{\partial \mathbf{H}}{\partial t} = \mathbf{R} - K\mathbf{D}\mathbf{H}^m, \tag{5.50}$$

$$\frac{d\mathbf{Q}}{dt} = -\mathbf{D}\mathbf{U} + \mathbf{F_1}, \tag{5.51}$$

$$\frac{d\mathbf{M}}{dt} = \mathbf{F_2} \tag{5.52}$$

where

$$\mathbf{H} = \begin{pmatrix} h(\Delta x) & h(2\Delta x) & h(3\Delta x) & h(4\Delta x) & \cdots & h(J\Delta x) \end{pmatrix}^T \tag{5.53}$$

$$\mathbf{R} = R(t) \begin{pmatrix} 1 & 1 & 1 & 1 & \cdots & 1 \end{pmatrix}^T \tag{5.54}$$

$$\mathbf{Q} = \begin{pmatrix} \widetilde{hc_1} \\ \widetilde{hc_2} \\ \vdots \\ \widetilde{hc_I} \end{pmatrix}^T \tag{5.55}$$

$$\mathbf{U} = \begin{pmatrix} \widetilde{qc_1} \\ \widetilde{qc_2} \\ \vdots \\ \widetilde{qc_I} \end{pmatrix}^T \tag{5.56}$$

$$\mathbf{F_1} = \begin{pmatrix} e_1 + e_{d1} \widetilde{+ r_1} + r_{r1} - d_1 \\ e_2 + e_{d2} \widetilde{+ r_2} + r_{r2} - d_2 \\ \vdots \\ e_I + e_{dI} \widetilde{+ r_I} + r_{rI} - d_I \end{pmatrix}^T \tag{5.57}$$

$$\mathbf{F_2} = \begin{pmatrix} \widetilde{d_1 - e_{d1}} - r_{r1} \\ \widetilde{d_2 - e_{d2}} - r_{r2} \\ \vdots \\ \widetilde{d_I - e_{dI}} - r_{rI} \end{pmatrix}^T \tag{5.58}$$

where each row element of $\mathbf{Q}$, $\mathbf{U}$, $\mathbf{F_1}$ and $\mathbf{F}_2$ are also column vectors of length J with each of their elements evaluated at $x = j\Delta x$, $j = 1, 2, \ldots, J$ and $\mathbf{D}$ is the differentiation matrix as given in section 4.1.2.

5.5 Verification of the Numerical Solution

To verify the implementation and accuracy of the MOL scheme, comparisons are made between the numerical solution and an analytical solution of (5.3) and previously computed solutions to (5.2) and (5.3).

5.5.1 Comparing to the Analytical Solution

Various analytical solutions of the kinematic wave equation have been presented in chapter 3. We now consider a case which has been adopted in Heng *et al.* (2008): rainfall and overland flow on an impervious uniform slope. The parameters used are $R = P = 100 \;\; mm \;\; hr^{-1}$, $K = \sqrt{S_0}/n$, $S_0 = 0.004$, $n = 0.02/60$, $L = 5 \;\; m$ and initial mean water flow depth is $1 \;\; mm$. Fig. (5.1) gives the comparison of numerical and analytical solution which demonstrates excellent agreement.

5.5.2 Comparing to a Previous Solution of the HR model

Section 4.1.2 has presented the numerical scheme for solving the HR model for constant h and q. In this section, we compare the numerical solution of full system which includes kinematic wave approximation to the constant h and

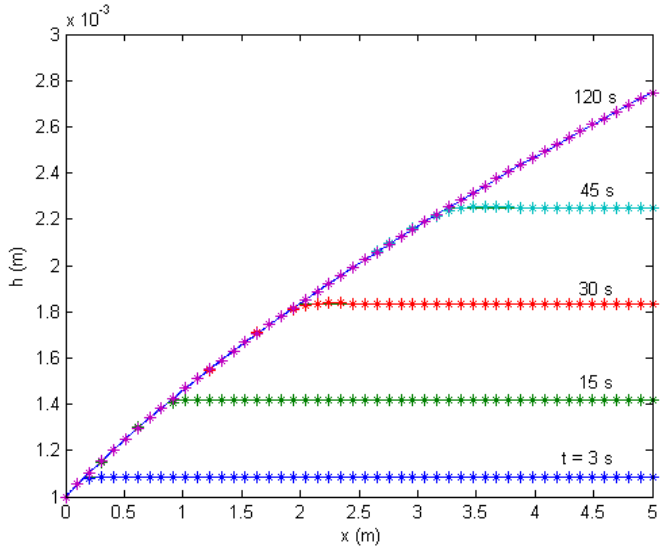

Figure 5.1: Comparing numerical solution (stars) of kinematic wave equation to its analytical solution (line) for rainfall and overland flow on uniform slope

q solution by forcing h and q to be a constant in the full system. The parameters used for this comparison are $R = P = 100\ mm\ h^{-1}$, $K = \sqrt{S}/n$, $S_0 = 0.004$, $n = 0.06/60$, $L = 5.8\ m$, $a = 920\ kg\ m^{-3}$, $a_d = 14190\ kg\ m^{-3}$, $m_t^* = 0.0767\ kg$, initial water depth $h(x, 0) = 5\ mm$. The mass percentage of soil is $p(i) = 0.1, i = 1, \cdots, I, I = 10$ and the settling velocity is $v = (0.21, 0.71, 3.30, 10.9, 19.4, 31.2, 69.1, 139, 210, 300)\ mm\ s^{-1}$. $\Delta x = 0.1\ m$ is used in the code. Fig. (5.2) shows the two solutions are identical.

5.6 Hysteresis in Sediment Transport

In the experiments of Polyakov and Nearing (2003), discussed in detail in chapter 4, it was shown that the transport capacity for a given flow rate, slope and soil type was dependent on whether sediment was being transported under net erosion or net depositional flows. Practically all commonly used erosion mod-

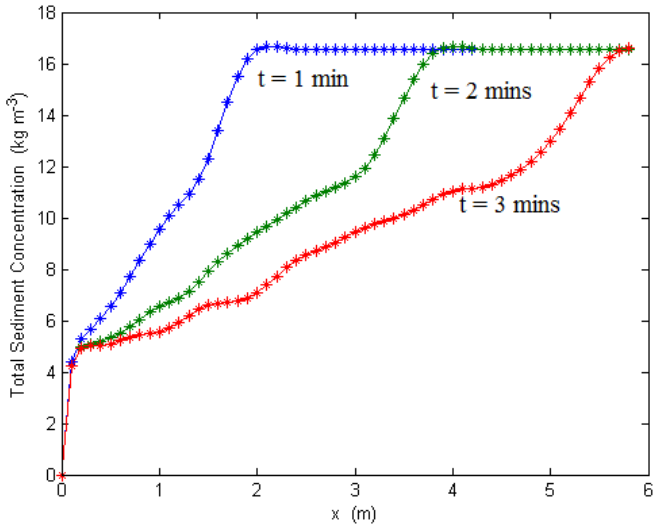

Figure 5.2: Comparison of solution (stars) of full system with solution (line) for simple HR model subject to $c_i(0,t) = m_i(0,t) = 0$ and $c_i(x,0) = m_i(x,0) = 0$.

els use the concept of transport capacity to distinguish between net erosion and net depositional flows. Secondly formulas used for determining transport capacity are single valued functions of the water flux q (Everaert, 1991; Woolhiser *et al.*, 1990), i.e. for a given soil, slope and flow rate it will be unique. Clearly these formulas are at odds with the experimental findings of Polyakov and Nearing (2003) whose results showed that it is dependent on the flow history and is therefore hysteretic. Using the Hairsine-Rose model, Sander *et al.* (2007a) were able to reproduce the measured suspended sediment concentrations for all experiments of Polyakov and Nearing (2003). The HR model does not need to use the concept of transport capacity because it models the rates of erosion and deposition separately, consequently transport capacity under any flow conditions in the HR model arises due to an evolving balance between the continually occurring rates of erosion and gravity deposition. They showed therefore that it is an output of the model and not an input and as such were able to reproduce the hysteretic

behavior of the experimental data. Sander *et al.* (2007a) showed the importance of the size distribution to hysteretic transport and were able to prove that the transport of each particle size class is also hysteretic and that it is only for soils comprised of a single size class that transport capacity is a unique function of the discharge.

Hysteresis in sediment transport has been known for some time especially within the fluvial geomorphology community. Plots of suspended sediment concentration versus river discharge have shown that the concentrations on the rising limb of the river discharge hydrograph were different to those on the falling limb Beschta (1987); Gurnell (1987); Kronvang *et al.* (1997); Seeger *et al.* (2004). Similarly plots of sediment discharge or suspended sediment concentration against water discharge occurring in overland flow have also shown significant hysteresis between the falling and rising limbs (Jansson, 2002; Klein, 1984; Sadeghi *et al.*, 2008; Smith and Dragovich, 2009). From this experimental data it has been found that there are five common shapes of the hysteresis loops (Williams, 1989) encompassing (i) single valued, (ii) clockwise, (iii) counter clockwise, (iv) figure 8 and (v) single valued plus a loop. It has been suggested that the shape of these loops can be used to identify the different processes of runoff, sediment transport (Seeger *et al.*, 2004) and the sediment source area (Jansson, 2002; Klein, 1984).

From the comparison with the data of Polyakov and Nearing (2003), it is known that the Hairsine-Rose model can reproduce hysteresis behavior for a fixed discharge. This section aims to investigate whether the HR model can reproduce any of the common hysteresis shaped loops for varying discharge. Up until now none of the existing erosion models available within the literature have undergone such a demanding test. With a view on the future potential possibility of obtaining experimental data for validation, only simplified flow conditions which are easily established within a laboratory flume are considered for this test. Consequently a flume with an impervious bed filled with saturated soil is considered. Since the flume is saturated and impervious, there is no infiltration, i.e. $R = P$ and runoff begins immediately at $t = 0$, therefore $t_p = 0$. The two

cases will be discussed below are (a) $h_i \neq 0$ and $c_i = 0$ at $t = 0$; (b) $h_i = 0$ and $c_i = 0$ at $t = 0$. The numerical result of case a is easy to obtain based on our time-dependent HR model. Case b needs additional calculations of analytical expansions of h, c_i and m_i at the ponding time t_p as presented in section 5.3.2. A single peak time-dependent excess rainfall rate given in (5.33) is again used in order to compute time and spatially varying water depths for generating a runoff hydrograph with both rising and falling limbs. The boundary conditions are taken as $x = 0$, $h_s = h_i$ and $c_i = 0$ for case a and $x = 0$, $h_s = 0$ and $c_i = \psi(t)$ as given in (5.18) for case b. The remaining initial condition for m_i is determined below with respect to the different hysteretic classes. The parameters used for simulation are obtained from curve fitting to the outflow data by Polyakov and Nearing (2003). The specific parameter values are not that important for the hysteresis simulation. They just need to be the right magnitude for the soil used in the experiments. They are given in Table (5.1) and Table (5.2) except p_i and v_i are given in Table (4.2).

5.6.1 Generation of Hysteresis Loops for $h_i \neq 0$

5.6.1.1 Counter Clock-wise Loop

Counter clock-wise hysteresis loops are known to occur when the peak water discharge occurs before the peak sediment concentration (Williams, 1989). Additional contributing factors are thought to be due to the sediment also having to travel further in the catchment to the outlet (Seeger *et al.*, 2004). In order to simulate these conditions for the flume scenario, it is assumed that at the start of the experiment no deposited layer has developed and only fully cohesive soil is in the flume. This means that there will be no quick release of sediment causing the sediment peak to be delayed compared to the water discharge peak. The remaining initial condition is therefore given by $t = 0$, $m_i = 0$. Fig. (5.3) shows the variation of total suspended sediment concentration c and flow discharge q as a function of time t as well as plotting $q * c$ as a function of the discharge q

Table 5.1: Hydraulic parameters used for simulation for both $h_i \neq 0$ and $h_i = 0$ (assuming that the rill is rectangular).

L	$6\ m$
S_0	0.07
n	$0.03\ s\, m^{-1/3}$
w_b	$0.1\ m$
F	0.062
J	$4.7856\ J\, kg^{-1}$
Ω_{cr}	$0.07\ W\ m^{-2}$
m_t^*	$2.5\ kg\ m^{-2}$
ρ	$1000\ kg\ m^{-3}$
ρ_s	$2000\ kg\ m^{-3}$
a_0	$200\ kg\, m^{-3}$
a_{d0}	$2000\ kg\, m^{-3}$

Table 5.2: Hydraulic parameters used for simulation for $h_i \neq 0$ and $h_i = 0$ respectively.

h_i	q	R_0	b
$2\ \ mm$	$0.006\ \ m^2\ min^{-1}$	$200\ \ mm\ hr^{-1}$	6
0	0	$600\ \ mm\ hr^{-1}$	3

for $h_i = 0.002\ m$. The lower graph clearly shows a counter clock-wise hysteretic loop. The upper graph shows that the discharge does reach its peak much sooner than c and that c has a greater value for the same discharge on the falling limb as opposed to the rising limb of the hydrograph.

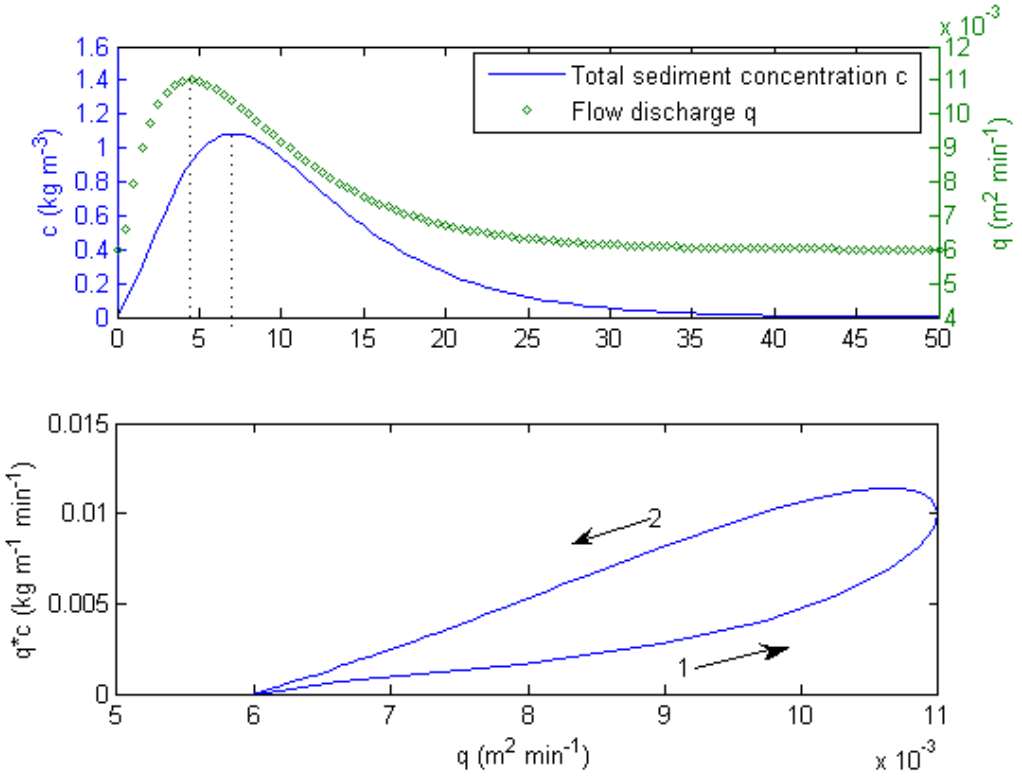

Figure 5.3: Upper: SSC vs t (left) and q vs t (right); Down: $q{*}c$ vs q; $h_i = 0.002m$ and $m_i = 0$ at $t = 0$.

5.6.1.2 Clock-wise Loop

Clockwise loops most commonly occur when the sediment peak occurs before the water discharge peak and when there is a source of rapid sediment depletion Williams (1989). This suggests that our flume simulation should begin with a fully developed deposited layer (i.e. $H = 1$) for the source of easily erodible sediment which can be rapidly depleted. Assuming that this layer is comprised of size classes in proportion to the original soil, then the initial condition for m_i becomes $t = 0$, $m_i = p_i m_t^*$. Fig. (5.4) shows graphs for $c(t)$, $q(t)$ and a clock-wise hysteretic loop for $q * c$ as a function of q. In agreement with Williams (1989) it can be seen from the upper graphs of Fig. (5.4) that the sediment peak does indeed occur before the discharge peak. By starting with a complete non-cohesive deposited layer, it provides a source of sediment which is easily eroded on the rising limb of the hydrograph. As this layer is depleted, more of the original cohesive soil is exposed which is less erodible than the deposited layer. Secondly as the event evolves, the deposited layer becomes more and more dominated by the larger sediment size classes. Consequently during the falling limb of the hydrograph for the same discharge, the flow energy is now being expended on either a greater amount of cohesive soil, or eroding larger deposited particles which have a greater fall velocity and therefore contribute less to the suspended sediment concentration. All this results in c being much higher on the rising limb in comparison to its value on the falling limb for the same discharge.

5.6.1.3 Figure 8 Loops

Since the hysteresis loop in Fig. (5.3) and Fig. (5.4) have swapped from counter clock-wise to clock-wise when the initial conditions change from no deposited layer to a fully developed deposited layer, then this suggests that a figure 8 loop can be obtained from an intermediate initial state for the deposited layer. Consequently the following initial condition is tried, $t = 0$, $m_i = 0.5 p_i m_t^*$ corresponding to $H = 0.5$. The results of this simulation are presented in Fig. (5.5)

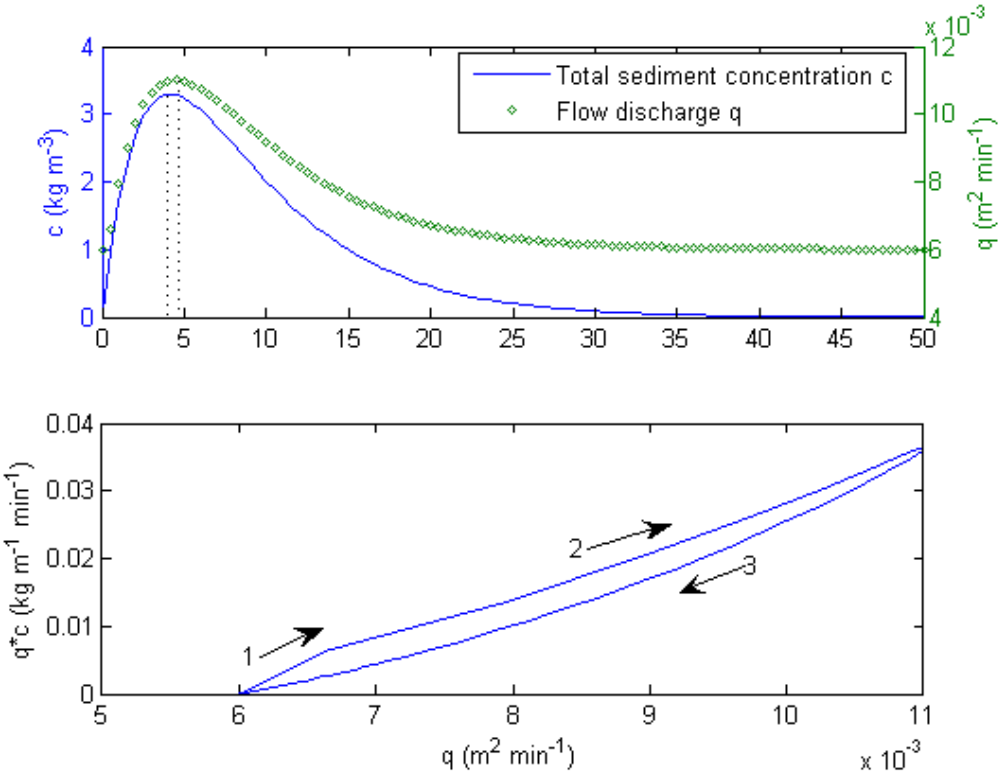

Figure 5.4: Upper: SSC vs t (left) and q vs t (right); Down: $q * c$ vs q; $h_i = 0.002\ m$ and $m_i = p(i)m_i^*$ at $t = 0$.

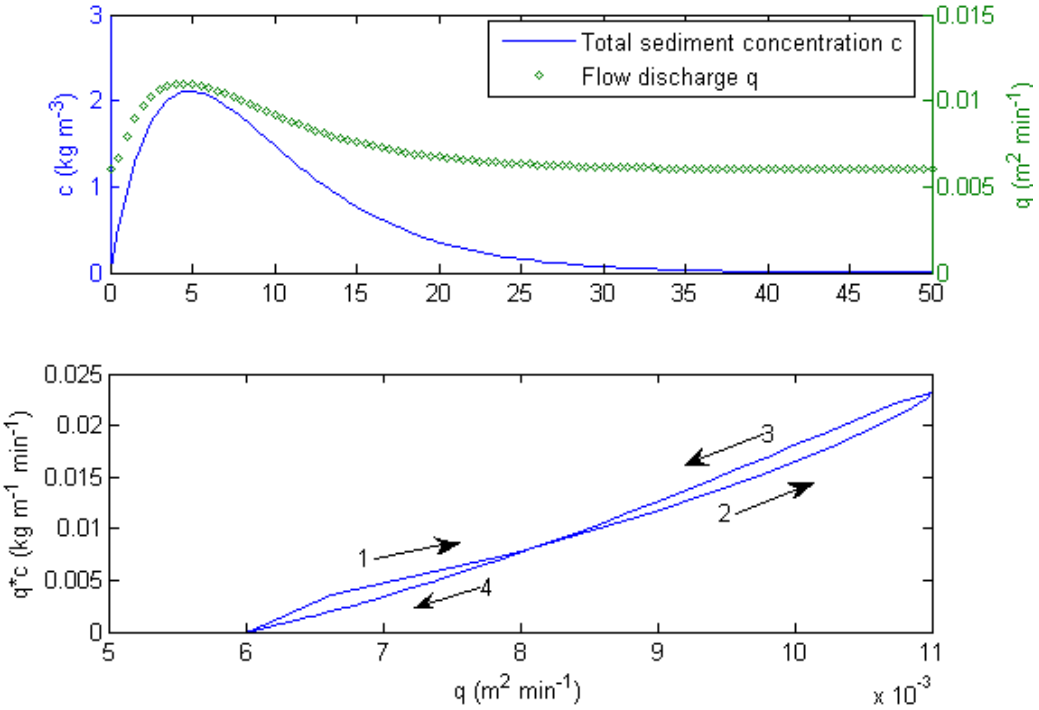

Figure 5.5: Upper: SSC vs t (left) and q vs t (right); Down: $q * c$ vs q; $h_i = 0.002\ m$ and $m_i = 0.5 p_i m_t^*$ at $t = 0$.

and show that a figure eight hysteresis loop is indeed obtained. Due to the presence of the significant deposited layer the sediment concentration rises rapidly and precedes that discharge peak, hence the lower part of the hysteresis loops mimics the clock-wise loop. With H only being half of its value, from Fig. (5.4) this layer is easily eroded sediment source is rapidly depleted as the discharge increases, exposing more of the original cohesive soil. The flow conditions then start to mimic those from Fig. (5.3) and the hysteresis loop swaps to the counter clock-wise shape, resulting then in an overall figure eight pattern. Exactly the same shaped figure eight hysteresis loop is shown in Fig. (5) of Seeger *et al.* (2004).

Finally Fig. (5.6) shows the relationship between the different suspended

sediment concentrations with time for the various hysteresis loops. This figure is in generally agreement with results and discussions in the literature on hysteresis loops for river flow in that: (i) counter clock-wise loops occur when the sediment supply is limited or far from the catchment outlet, (ii) clockwise loops occur where there is a source of easily erodible sediment near the river and (iii) figure eight loops can occur where sediment sources are spatially distributed prior to an erosion event. Catchment studies in the literature have shown that the types of hysteresis loops found depend on initial soil moisture, previous precipitation events, total rainfall rate, maximum rainfall intensity and variability in rainfall intensity (Eder *et al.*, 2010; Seeger *et al.*, 2004). Clearly none of these is surprising as these factors affect the initiation of surface runoff, time to peak discharge, the episodic movement and deposition of sediment throughout the catchment (i.e. deposited layer) and the rate of its depletion. To some extent we have tried to simulate these effects through imposing different initial conditions on m_i, i.e. $m_i = 0$, $0.5p_i m_t^*$ and $p_i m_t^*$ at $t = 0$ for all x to represent surface conditions arising from both long and short periods between erosion events. Episodic rainfall events of short duration or events with multiple peaks will result in non-homogeneous distributions of deposited sediment for the next rainfall event. Such circumstances point to a further advantage of the HR formulation in that the deposited layer allows for varying initial surface states to be prescribed prior to any erosion event (Seeger *et al.*, 2004).

5.6.2 Generation of Hysteresis Loops for $h_i = 0$

As mentioned before, we assume that the bed of experimental flume is impervious and the soil is initially saturated. Therefore, for $h_i = 0$, runoff generates as soon as rainfall commences, i.e. at $t = t_p = 0$. In an equivalent manner to the case of $h_i \neq 0$, we use $m_i = 0$, $m_i = p_i m_t^*$ and $m_i = 0.5p_i m_t^*$ at $t = 0$ in order to generate counter clock-wise, clock-wise and figure 8 shaped loop respectively.

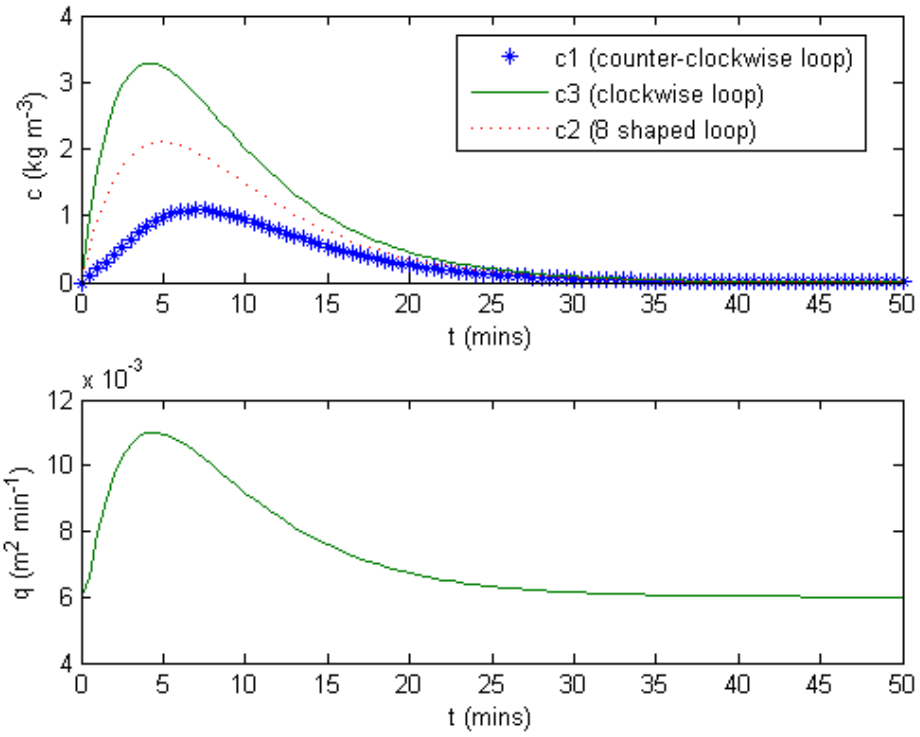

Figure 5.6: Different SSCs for same q

Fig. (5.7) shows c and q varying with t and the plot of $q*c$ as a function of the discharge q. The upper graph clearly shows the again the sediment concentration peak lags behind the flow discharge peak and c has greater value for the same discharge on the falling limb as opposed to the rising limb of the hydrograph which are consistent with a counterclockwise loop as found in Fig. (5.3). However, the lower portion graph near the origin shows a figure 8 shape loop instead of a counter clock-wise loop. To check this, h_i is reduced from 0.002 m to 0.00002 m in the code for Fig. (5.3). We find that the loop transforms from counter clock-wise to a figure 8 shape, in the region close to the origin.

Fig. (5.8) and Fig. (5.9) are for $m_i = p_i m_t^*$ and $m_i = 0.5 p_i m_t^*$ respectively. The variations of c and q with t and the loops generated by plotting $q * c$ vs q

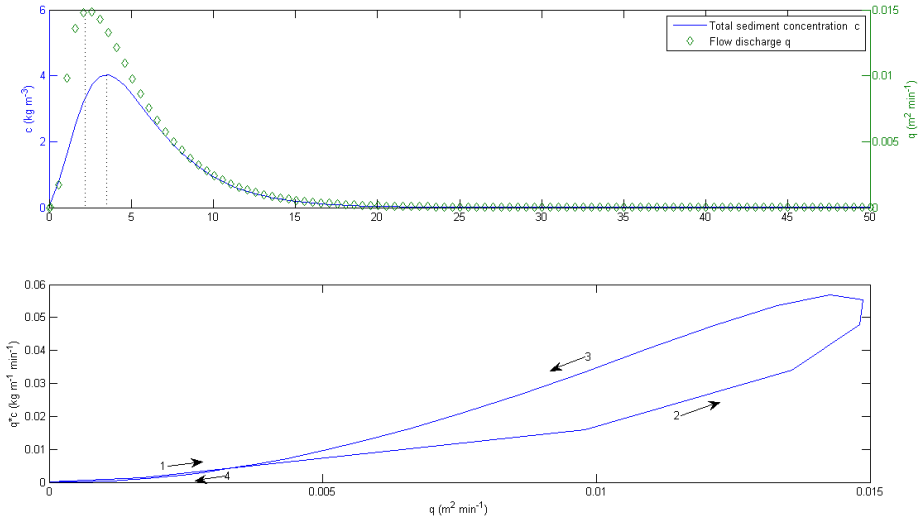

Figure 5.7: Upper: SSC vs t (left) and q vs t (right); Down: $q * c$ vs q; $h_i = 0$ and $m_i = 0$ at $t = 0$.

correspond to the same types of loops given in Fig. (5.4) and Fig. (5.5), i.e. counterclockwise and figure 8 respectively.

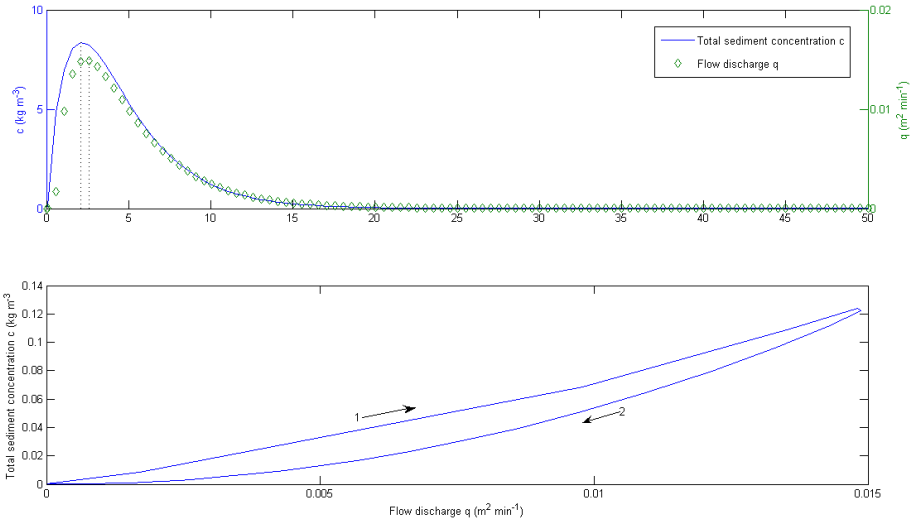

Figure 5.8: Upper: SSC vs t (left) and q vs t (right); Down: $q * c$ vs q; $h_i = 0$ and $m_i = p_i m_t^*$ at $t = 0$.

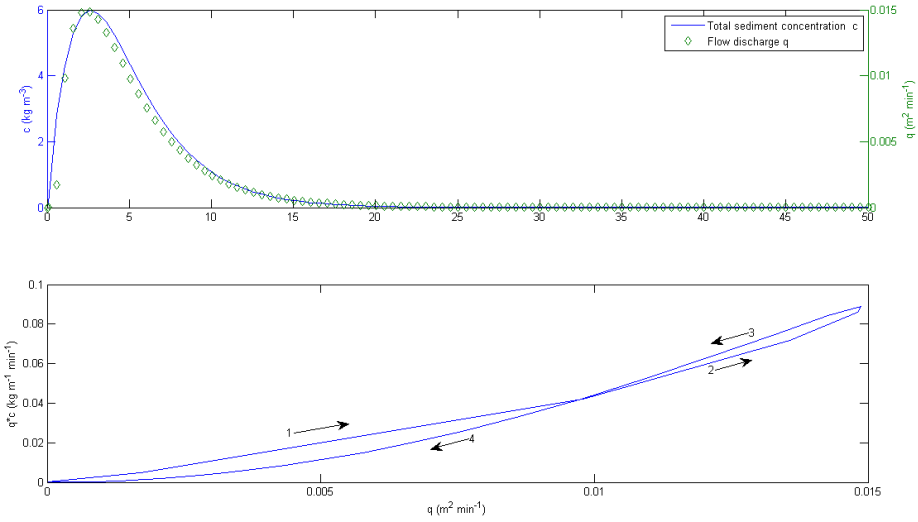

Figure 5.9: Upper: SSC vs t (left) and q vs t (right); Down: $q * c$ vs q; $h_i = 0$ and $m_i = 0.5 p_i m_t^*$ at $t = 0$.

5.7 Conclusion

Typically in a field or hillslope setting, there is a time lag between the start of rainfall and the subsequent commencement of overland flow. This time lag is commonly referred to as the ponding time t_p. During the period $0 < t < t_p$ raindrops are still detaching cohesive soil particles which result in the evolution of the deposited layer such that at the time of runoff, m_i is nonzero. A theoretical framework is provided in this chapter to describe the evolutionary period. Since $h = 0$ at the start of runoff, it is also shown that this prescribes the initial conditions for c_i in order to remove a singularity from the sediment transport equations. Consequently a power series expansion is found for both m_i and c_i to allow numerical solutions to be started away from this singularity. Expansions for both constant and time dependent excess rainfall rates are provided, though to reduce complexity in the solution it is assumed that the time dependent case occurs on an initially saturated surface whereby $t_p = 0$. The numerical method of lines solution developed in Chapter 4 for constant flow hydraulics was then extended in this Chapter to include both space and time dependent overland flow.

Most currently used soil erosion models cannot account for sediment transport hysteresis, i.e. different sediment fluxes for the same discharge on the rising and falling limb of the overland flow hydrograph. Specifically, clockwise, anti-clockwise and figure 8 loops have been found. It is shown for the first time that one soil erosion model (the HR model) is able to simulate the various hysteretic discharge patterns. More importantly, the HR model′s construction permits a straightforward explanation of the various hysteretic behaviors observed experimentally. In brief, hysteresis occurs because of the interactions between variable flow over the soil surface and the differences in cohesion between the original and eroded soil, the latter being more erodible than the former. With commonly used formulations, as presented in Chapter 2, being based solely on suspended sediment it is therefore unlikely that they can produce the various known hysteresis

loops.

CHAPTER 6

Conclusion and Research Prospects

The main aim of this research was to develop new analytical and numerical solutions to both the kinematic approximation to the St Venant equations and the Hairsine-Rose (HR) soil erosion model in order to gain a better physical understanding of soil erosion and sediment transport in shallow overland flow. The HR model was chosen not only because it was a physical process based erosion model, there are many of these to be found in the literature, but because this model has unique advantages: 1. it considers the entire distribution of sediment size classes and does not use a physically unrealistic single representative particle; 2. it considers the development of a layer of deposited sediment having different characteristics to the original underlying soil and 3. it separately considers the erosion processes of rainfall detachment, runoff entrainment and gravitational deposition which results in transport capacity to be a non-unique function of the flow rate. The second main aim was to develop new numerical solutions to the HR model while the third was to apply these solutions to experimental data obtained from the literature.

How the aims of this research was achieved is discussed and summarized below.

6.1 Research Outcomes

1. Development of new analytical solutions for the kinematic wave approximation equation.

Nearly all existing analytical solutions for the kinematic equation are subject to the initial h_i and boundary conditions h_s both zero. In Chapter 3, new analytical solutions are developed for the three following combinations of boundary and initial conditions, $h_s = h_i = h_b$, $h_s < h_i$ and $h_s > h_i$. While these do not necessarily occur very often in the field, they do reflect various conditions used in experimental laboratory scale flumes. In addition both constant and time dependent excess rainfall rates are considered. As the kinematic wave equation is hyperbolic, the method of characteristics was used to derive the new analytical solutions. In the case of the time dependent excess rainfall rate a further two sub-cases were considered, these being $R(t) > 0$ for all time t and $R(t) > 0$, $0 < t < t^*$ and $R(t) < 0$, $t > t^*$. Solutions for $h_s < h_i$ resulted in expansion fans while those for $h_s > h_i$ contained travelling shocks. When R was allowed to become negative for $t > t^*$ then at a later time, denoted t_2 the single continuous solution profile for $h(x,t)$ actually split into two profiles with one moving up slope and the other moving down slope. As a result the drying free boundary of both solutions needed to be found. These new solutions are a comprehensive extension of the solution given by Sander *et al.* (1990).

2. Development of solutions for time-dependent HR model

In Chapter 4 numerical solutions to the HR model were obtained for conditions where runoff entrainment and gravity deposition were the only erosive processes operating. It was not possible to find an analytical solution for all x and t. However by using the method of characteristics is was possible to reduce the coupled partial differential equations to a set of coupled ordinary differential equations for the sub-domain of $x > qt$, provided only uniform constant initial conditions were considered. A full numerical solution of the partial differential equations was developed by applying the method of lines and was verified in two

ways by: 1. comparing with the solution of the ordinary differential equations for $x > qt$; and 2. comparing with analytical steady state solution given by Sander *et al.* (2007a). Excellent agreement was found from both comparisons and gave confidence in the accuracy and reliability of the numerical solution method.

The numerical solution was then applied to the laboratory flume experiments of Polyakov and Nearing (2003). Comparisons to both the steady state and time varying data were done. This demonstrated that the HR model could reproduce their detailed suspended sediment data taken across a range of net erosion and net deposition conditions. However, it was found that the model significantly over-predicted the amount of sediment deposited at the inlet of flume. This then indicated that an additional transport mechanism was missing from the HR model which would allow for this additional deposited sediment to be moved down the flume. Rouse number calculations provided some support for believing that the missing transport mechanism was bed-load and this lead to developing an extended HR model which included bedload.

3. Extension of the HR model to include bed-load

With the bed-load transport mechanism included in the HR model both analytic steady state and unsteady numerical solutions were developed. The comparison between the steady state solution and data of Polyakov and Nearing (2003) still showed excellent agreement for all size classes. The comparison between the unsteady solution with the time varying data showed that the inclusion of bed-load transport has significantly improved the physical plausibility of calculated total mass of sediment in the deposited layer, however it came at the expense of poorer match to the sediment outflow data. This lead to the conclusion that the addition of bed-load transport was not sufficient for the HR model to explain the Polyakov and Nearing (2003) data and that changes in bed morphology may be a more important influence on the transport processes. An asymptotic analysis was carried out which confirmed that for the Polyakov and Nearing data, bed evolution was more important than bed-load transport in moving deposited sediment down the flume.

A very interesting finding from this work showed that the traditional criterion of validating a sediment transport model based solely on suspended sediment data was not sufficient. It was shown that reliable predictions could be obtained even when important transport mechanisms were neglected.

4. Development of fully coupled unsteady solutions of the HR model and the kinematic flow equation

In Chapter 5 the method of lines was used to develop a numerical solution for the combined system of equations which included the HR model and the kinematic wave equation. With non zero initial and boundary conditions for h the numerical solution is straightforward. However for zero depth initial and boundary conditions there is a singularity in the sediment transport equation at ponding time, i.e. at the time of runoff commencing. Consequently an analytic expansion was developed in order to obtain starting conditions for the solution of the suspended sediment equations. While laboratory flumes can be loaded with pre-wet soil so the runoff begins immediately following the start of rainfall, this usually does not occur in the field and there is a considerable time delay between the two. During this period raindrop impact disturbs the soil surface by detaching cohesive soil and thereby begins to develop the deposited layer. This Chapter also provides an analytical solution for describing this layer's evolution from the start of rainfall, which then allows the initial conditions for m_i to be established at ponding time.

5. Using the coupled HR - kinematic numerical solution to simulate hysteresis phenomena in sediment transport

Plots of sediment discharge or suspended sediment concentration against water discharge occurring in overland flow have been shown to contain significant hysteresis between the falling and rising limbs. Experimental data has shown that the most common shapes of the hysteresis loops (Williams, 1989) are (i) clockwise, (ii) counter clockwise, (iii) figure 8 and (iv) single valued plus a loop. It has been suggested that the shape of these loops can be used to identify the

different processes of runoff, sediment transport (Seeger *et al.*, 2004) and the sediment source area and availability (Jansson, 2002; Klein, 1984).

With the numerical solution developed for full system of soil erosion and kinematic flow it was shown that it was possible for the HR model to simulate three of four hysteresis loops identified by Williams (1989). Counter clock-wise loops, clock-wise loops and figure 8 loops could be produced as a result of different initial conditions, being $m_i(x,0) = 0$, $m_i(x,0) = p_i m_t$ and $m_i(x,0) = 0.5 p_i m_t$ respectively. As far as the author is aware, this is the first time that these types of hysteresis loops have been produced by any erosion model. The generation of these hysteresis loops are physically explainable in terms of sediment availability and is consistent with data obtained on the field scale.

6.2 Research Significance and Future Research Directions

Govers (2011) recently noted that the modeling of size-selectivity in both net erosion and net deposition events is "poorly represented in most erosion models". Even though quite a few of the commonly used erosion models have developed the capacity to consider limited distributions of sediment size classless (i.e. LISEM, KINEROS2, WEPP), their predictive ability is still limited by their use of a transport capacity (T_c) approach. There are several concerns with basing sediment transport models on the concept of transport capacity. First, erosion is dependent on the soils particle size distribution, with each size having its own separate contribution. Second, it is hysteretic in that different values of T_c occur for the same flow rate q on either side of the rising and falling limb of a runoff hydrograph. That T_c (for both the total sediment transported as well as that for the individual size classes) is hysteretic was shown in a set of well-controlled flume experiments by Polyakov and Nearing (2003). Thus, particle size class distribution and hysteresis dependence makes it difficult to develop reliable formulas

for determining T_c. While the multi-size class models have developed approximate equations, these are unsatisfactory from a physical point of view as they are effectively a model input. Transport capacity at any given time and spatial location, for any particular flow condition, evolves from the flow itself and is due to the balance between three separate erosion mechanisms, viz., gravity deposition, rainfall and runoff detachment. It is, therefore, an outcome of, and not an input to, the erosion process. In the case of WEPP, different rate equations are even used to describe different aspects of the same physical process and is therefore physically inconsistent.

The HR (Hairsine-Rose) approach adopted for this thesis is unique amongst erosion models in that it includes separate rate equations for all three erosion mechanisms, and so does not require the transport capacity concept. This model is also distinctive from those previously presented in other aspects. First, the HR model describes the soil by its particle size probability density function, and is therefore not limited in the number of size classes it considers. When soil particles are in suspension, both the suspension time and transport distance, depend on the particle's settling velocity. With particle size settling velocities varying over many orders of magnitude ($10^{-6} - 0.1\ m\ \ s^{-1}$), a single effective size class is not representative of the behaviour of eroded soil. As both agricultural chemical (fertilizers, pesticides) and biological (bacteria, viruses) pathogens bind preferentially to the clay and silt sized particles (Morgan and Quinton, 2001; Schijven and Hassanizadeh, 2000), estimating contaminant fluxes to surface water bodies requires knowledge of the size distribution of transported sediment. Second, the HR model also recognizes that eroded soil depositing on the soil surface forms a covering layer that does not possess the same cohesive strength of the original soil. Due to the size-selective nature of the deposition process, the distribution of sediment in the covering layer is different to the original soil material.

The significance of the HR approach was demonstrated in Section 5.6 where straightforward explanations could be provided of the various hysteretic sediment transport behaviors observed experimentally. This is the first time that any soil

erosion model has been able to simulate the various hysteretic discharge patterns and is therefore a major contribution to the erosion literature. In brief, hysteresis occurs because of the interactions between variable flow over the soil surface and the differences in cohesion between the original and eroded soil, the latter being more erodible than the former. In particular it was shown that the state of the soil surface prior to an erosion event is especially important in determining the resulting shape of the hysteretic discharge curves. With commonly used formulations, as presented in Chapter 2, being based solely on suspended sediment and T_c, it is therefore very unlikely that they can produce the various known hysteresis loops.

The second and third main areas of research significance center on (i) the stringency of model validation and (ii) identifying when interactions between the overland flow and the evolution of the soil bed are importance in determining sediment transport fluxes and size distributions. Most models are usually validated by comparing total sediment fluxes at a catchment or flume outlet. Good temporal agreement is always taken as justification of model reliability and performance. Rarely is agreement with exported size class distributions looked at. In Chapter 4 it was shown that by using the HR model excellent agreement between measured and predicted c_i and c with time, at the flume exit, could be obtained for the dynamic and complex experiment of Polyakov and Nearing (2003). This was a level of match not achieved by any other model or any data published in the literature. Since predicting suspended sediment size class distributions is far more difficult than predicting total suspended sediment, this appeared to provide very strong validation of the HR modelling approach. However by examining the mass of deposited sediment along the flume it was found that non-physical estimates were being obtained. Consequently by focussing solely on suspended sediment, erosion models can seem to be reliably validated when in reality they are missing key transport mechanisms. A formal asymptotic analysis showed that the coupling of bed morphology with the overland flow was an important transport process in the Polyakov and Nearing experiments. The data in Table

2 of Polyakov and Nearing (2003) give a Froude number (F_r) at $x = 2\ \ m$ of 1.1, indicating supercritical flow down the rill. Linear stability analysis of flow and bedform evolution in rivers (Fowler, 1997) shows that for $F_r > 1$, there is a very strong coupling between the flow velocity, flow depth and the bed morphology resulting in the formation of both dunes and anti-dunes. Previously published rill results from both experimental data (Nearing *et al.* (1997), Gimén*ez* and Govers (2001)) and numerical modeling (Lei and Nearing, 1998) have shown the importance of bed evolution on transport processes for Froude numbers near unity. Thus the asymptotic analysis not only supports recent findings in the literature but also clearly shows the need to have erosion models incorporate interactions between the bed and the flow. For intense storms that result in near critical and supercritical flow in rills, neglecting bed morphology is likely to result in the very poor performance of any erosion model when it comes to predicting transported sediment loads.

In terms of future research they are many directions that can be taken and many different problems to work on. The following comments will focus on areas which would be of benefit to the HR approach.

1. There is a real need for research to be undertaken on how to upscale the HR model to regional or catchment scale such that computation demands are not prohibitive. In its current form this is a serious drawback.

2. Greater laboratory and hillslope scale testing is required to verify and validate the predictions of the HR model. For example there does not appear to be available experimental method for collecting data on the evolution of the deposited layer through either space or time. The use of nano-particles to label soil particles is a possibility provided a convenient method can be developed.

3. Collecting real time spatial and temporal data on suspended sediment distributions would also be extremely valuable. Matching data at one spatial location, usually the flume outlet is no longer a satisfactory approach.

4. Recent work on local variations in bed topography have shown how important this can be on transported sediment distributions (Heng *et al.*, 2011) and the HR model has had some success in reproducing such data. More complicated bed geometry which would result in zones of both net erosion and net deposition from which detailed data on deposited size distributions would provide a very demanding test of the HR modeling methodology.

5. Lastly there is the area of predicting contaminant fluxes (both chemical and biological pathogens) during an erosion event. Enrichment ratios which are commonly used have proved to be very unreliably in estimating these fluxes. The HR model provides the framework for incorporating size class dependent adsorption of contaminants that has the potential to predict or estimate contaminant fluxes both during and from sequential erosion events. Currently concerns about the level and transport of bacteria and viruses through the environment, and the possibility of some of these crossing into humans (zoonotic viruses), is topical. With agriculture being a major source of such pathogens, either through direct fecal deposition or through the spread of infected slurries on farmland, further research is required on the rate and quantity of pathogens transported from farmlands. The size class dependent HR model which has been studied in this thesis and shown to be able to reproduce data and hysteretic flows from a range of erosion conditions, is uniquely placed to provide a significant contribution and greater understanding of pathogenic transport in the environment.

APPENDIX A

A journal paper

APPENDIX B

A conference paper

APPENDIX C

Two conference posters presentation

References

Aksoy, H. and Kavvas, M. (2005). A review of hillslope and watershed scale erosion and sediment transport models. *Catena*, **64**, 247–271.

Alberts, E., Moldenhauer, W. and Foster, G. (1980). Soil aggregates and primary particles transported in rill and interrill flow. *Soil Science Society of America Journal*, **44**, 590–595.

Alberts, E., Wendt, R. and Priest, R. (1983). Physical and chemical properties of eroded soil aggregates. *Transactions of the ASAE*, **26**, 465–471.

Asadi, H., Ghadiri, H., Rose, C., Yu, B. and Hussein, J. (2007). An investigation of flow-driven erosion processes at low streampowers. *Journal of Hydrology*, **342**, 134–142.

Ayres, Q. (1936). *Soil erosion and its control*. McGraw-Hill, New York, USA.

Bagnold, R. (1966). An approach to the sediment transport problem for general physics. *U.S.Geological Survey Professional Paper*, 1–37.

Bagnold, R. (1977). Bed laod transport by natural rivers. *Water Resources Research*, **13**, 303–311.

Barry, D., Sander, G., Jomaa, S., Heng, B., Parlange, J., Lisle, I. and Hogarth, W. (2010). Exact solutions of the hairsine-rose precipitation-driven erosion model for a uniform grain size soil. *Journal of Hydrology*, in press. Doi: 10.1016/j.jhydrol.2010.06.016.

Barton, A., Fullen, M., Mitchell, D., Hcking, T. and Liu, L. (2004). Effects of soil conservation measures on erosion rates and crop productivity on subtropical ultisols in yunnan province,china. *Agriculture,ecosystems & Enviroment*, **104**, 343–357.

Beasley, D., Huggins, L. and Monke, E. (1980). Answers: a model for watershed planning. *Transactions of the ASAE*, 938–944.

Beschta, R. (1987). *Sediment Transport in Gravel-Bed Rivers*, Comceptual Models of Sediment Transport in Streams, 387–419. Wiley.

Beuselinck, L. (1999). *Sediment deposition by overland flow: An experimental and modelling approach*. Ph.d. thesis, Katholieke Univ.Leuven, Leuven, Belgium.

Beuselinck, L., Govers, G., Steegen, A. and Quine, T. (1999). Sediment transport by overland flow over an area of net deposition. *Hydrological Processes*, **13**, 2769–2782.

Beuselinck, L., Govers, G., Hairsine, P., Sander, G. and Breynaert, M. (2002). The infulence of rainfall on sediment transport by overland flow over areas of net deposition. *Journal of Hydrology*, **257**, 145–163.

Brazier, R. (2004). Quantifying soil erosion by water in the uk: a review of monitoring and modelling approaches. *Progress in Physical Geography*, **28**, 340–365.

Campbell, S., Parlange, J. and Rose, C. (1984). Overland flow on converging and diverging surfaces - kinematic model and similarity solutions. *Journal of Hydrology*, **67**, 367–374.

Cao, Z., Day, R. and Egashira, S. (2002). Coupled and decoupled numerical modelling of flow and morphological evolution in alluvial rivers. *Journal of Hydraulic Engineering, ASCE*, **128**, 306–321.

Croley, T. (1982). II. unsteady overland flow sedimentation. *Journal of Hydrology*, **56**, 325–346.

Cundy, T. and Tento, S. (1985). Solution to the kinematic wave approach to overland flow routing with rainfall excess given by philip's equation. *Water Resources Research*, **21**, 1132–1140.

De Roo, A., Wesseling, C. and Ritsema, C. (1996). Lisem: a single-event physically based hydrological and soil erosion for drainage basins: 1. theory, input and output. *Hydrological Processes*, **10**, 1107–1117.

Eder, A., Strauss, P., Krueger, T. and Quinton, J. (2010). Comparative calculation of suspended sediment loads with respect to hysteresis effects (in the petzenkirchen catchment, austria). *Journal of Hydrology*, **389**, 168–176.

Ekern, W. (1951). Raindrop impact as a force initiating soil erosion. *Soil Science Society of America Proceedings*, **15**.

Ellison, W. (1947). Soil erosion studies. *Agriculture Engineering*, **28**, 145–146.

Everaert, W. (1991). Empirical relations for the sediment transport capacity of interrill flows. *Earth Surface Processes and Landforms*, **16**, 513–532.

Ferro, P.P., V. (2000). Sediment delivery distributed (sedd) model. *Journal of Hydraulic Engineering*, **5**, 411–422.

Foster, G. (1982). Modeling the erosion process. C. Haan, H. Johnson and B. D.C., eds., *Hydrologic Modeling of Small Watersheds*, vol. 5, 259–380, Am. Soc. Agric. Engrs Monograph.

Foster, G. and Meyer, L. (1972). A closed-form soil erosion equation for upland areas. H. Shen, ed., *Sedimentation Symposium*, 12.1–12.9, Colorado State University, Fort Collins, CO, in Honor Prof. H.A. Eubstein.

Foster, G., Young, R. and Neibling, W. (1985). Sediment composition for nonpoint source pollution analysis. *Transactions of the ASAE*, **28**, 133–139.

Fowler, A. (1997). *Mathematical Models in the Applied Sciences*. Cambridge Univ Press, England.

GLASOD (1990). *Global assessment of soil degradation*. ISRIC, Wageningen.

Govers, G. (1990). Empirical relationships on the transporting capacity of overland flow. *International Association of Hydrological Sciences*, **189**, 45–63.

Govers, G. (2011). *Handbook of Erosion Modelling*, Misapplications and Misconceptions of Erosion Models, 117–134. Wiley-blackwell.

Govers, G., Lobb, D. and Quine, T. (1999). Tillage erosion and translocation: emergence of a new paradigm in soil erosion research. *Soil Tillage Research*, **51**, 167–174.

Govindaraju, R. and Kavvs, M. (1991). Modelling the erosion process over steep slopes: approximate analytical solutions. *Journal of Hydrology*, **127**, 279–305.

Gurnell, A. (1987). *Glacio-Fluvial Sediment Transfer*, Suspended Sediment, 305–354. Wiley:Chichester.

Haberman, R. (1997). *Elementary applied partial differential equations with fourier series and boundary value problems*. Prentice Hall.

Hairsine, P. (1988). *A Physically-based Model of the Erosion of Cohesive Soils*. Ph.d. thesis, Griffith University, Brisbane, Queensland,Australia.

Hairsine, P. and Rose, C. (1991). Rainfall detachment and deposition: Sediment transport in the absence of flow-driven processes. *Soil Science Society of America Journal*, **55**, 320–324.

Hairsine, P. and Rose, C. (1992a). Modeling water erosion due to overland flow using physical principles, 1, sheet flow. *Water Resources Research*, **28**, 237–243.

Hairsine, P. and Rose, C. (1992b). Modeling water erosion due to overland flow using physical principles, 2, rill flow. *Water Resources Research*, **28**, 245–250.

Hairsine, P., Sander, G., Rose, C., Parlange, J., Hogarth, W., Lisle, I. and Rouhipour, H. (1999). Unsteady soil erosion due to rainfall impact: a model of sediment sorting on the hillslope. *Journal of Hydrology*, **220**, 115–128.

Hairsine, P., Beuaelinck, L. and Sander, G. (2002). Sediment transport through an area of net deposition. *Water Resources Research*, **38**, 1086, doi: 10.1029/2001 WR000265.

Heilig, A., DeBruyn, D., Walter, M., Rose, C., Parlange, J., Steenhuis, T., Sander, G., Hairsine, P., Hogarth, W. and Walker, L. (2001). Testing a mechanistic soil erosion model with a simple experiment. *Journal of Hydrology*, **244**, 9–16.

Henderson, F. and Wooding, R. (1964). Overland flow and groundwater flow from a steady rainfall of finite duration. *Journal of Geophysical Research*, **69**, 1531–1540.

Heng, B., Sander, G., Armstrong, A., Quiton, J., Chandler, J. and Scott, C. (2011). Modelling the dynamics of soil erosion and size-selective sediment transport over nonuniform topography in flume-scale experiments. *Water Resources Research*, **47**.

Heng, P., Sander, G. and Scott, C. (2008). Modeling overland flow and soil erosion on non-uniform hillslopes: A finite volume scheme. *Water Resources Research*, **45**, 1–20.

Hogarth, W., Rose, C., Parlange, J., Sander, G. and Carey, G. (2004). Soil erosion due to rainfall impact with no inflow: a numerical solution with spatial and temporal effects of sediment settling velocity characteristics. *Journal of Hydrology*, **294**, 229–240.

Hu, W., Zhai, S., Zhu, Z. and Han, H. (2008). Impacts of the yangtze river water transfer on the restoration of lake taihu. *Ecological Engineering*, **34**, 30–49.

Hudson, N. (1957). Erosion control research. *Rhodesia Agriculture Journal*, **54**, 297–323.

Hudson, N. (1981). *Soil Conservation*. Cornell University Press, Ithaca, N.Y., USA., 2nd edn.

Jansson, M. (2002). Determining sediment source areas in a tropical river basion, costa rica. *Catena*, **47**, 63–84.

Jiang, H., Cui, Y. and Chen, B. (2005). The variation trend of nutrient salts in the bohai sea. *Marine Fisheries Research*, **26**, 61–67, in Chinese.

Jin-Jun, Z., Xiu-Ben, H., D., W., Xin-Bao, Z., Flanagan, D. and Yong-Qing, Q. (2007). Assessing soil erosion rates on manually-tilled hillslopes in the sichuan hilly basin using ^{137}cs and ^{210}pb$_{ex}$ measurements. *Pedosphere*, **17**, 273–283.

Kee Kwong, K., Bholah, A., Volcy.L and Pynee, K. (2002). Nitrogen and phosphorus transport by surface runoff froma silty clay loam soil under sugarcane in the humind tropical environment of mauritius. *Agriculture, Ecosystems & Environment*, **91**, 147–157.

Klein, M. (1984). Anti clockwise hysteresis in suspended sediment concentration during individual storms: Holbeck catchment; yorkshire, england. *CATENA*, **11**, 251–257.

Kronvang, B., Laubel, A. and Grant, R. (1997). Suspended sediment and pariculate phosphorus transport and delivery pathways in an arable catchment, gelbaek steam, denmark. *Hydrological Processes*, **11**, 627–642.

Krysanova, V., Becker, A. and Klocking, B. (1998). *Modelling Soil Erosion, Sediment Transport and Closely Related Hydrological Processes*, The linkage between hydrological processes and sediment transport at river basin scale. 249, IAHS Publ.

Laflen, J., Elliot, W., Flanagan, D., Meyer, C. and Nearing, M. (1997). Wepp-predicting water erosion using a process-based model. *Journal of Soil and Water Conservation*, 96–102.

Lal, R. (2001). Soil degradation by eroion. *Land Degradation & Development*, **12**, 519–539.

Lal, R. (2003). Soil erosion and the global carbon budget. *Environment International*, **29**, 437–450.

Lamb, H. (1932). *Hydrodynamics*. Cambridge University Press.

Lane, L. and Shirley, E. (1985). Erosion and sediment yield equations: Solutions for overland flow. *Workshop on USLE Replacement*, Nat.Soil Erosion Lab., West Lafayette, Indiana.

Laws, J. (1940). Recent studies in raindrops and erosion. *Agriculture Engineering*, **21**, 431–433.

Lei, T. and Nearing, M. (1998). Rill erosion and morphological evolution: A simulation model. *Water Resources Research*, **34**, 3157–3168.

Lighthill, M. and Whitham, G. (1955). Kinematic waves,1. *Pro.Roy.London*, **229**, 281–316.

Lopes, V. (1987). *A Numerical Model of Watershed Erosion and Sediment Yield*. Ph.D. thesis, The University of Arizona.

Lopes, V. and Lane, L., eds. (1988). *Modelling Sedimentation Processes in Small Watershed*, no. 174 Sediment Budgets, Porto Alegre Symposium, IAHS Publications.

MacArthur, R. and J.Devries, J. (1993). Introduction and application of kinematic wave routing techniques using hec-1. Tech. rep., US Army Corps of Enigneers, Hydrologic Engineering Center.

Mehta, A. (1983). Characterization tests for cohesive sediments. H. Shen, ed., *Proc. of Conf. on Frontiers in Hydraul. Engineering*, 79–84, ASCE/MIT, Cambridge, Massachusetts.

Meyer, L., Foster, G. and Romkens, M. (1975). Source of soil eroded by water from upland slopes. *Present and prospective technology for predicting sediment yields and sources*, ARS-S-40, 177–189, USDA-ARS, Oxford,Mississipi.

Moreno-de las Heras, M. (2009). Development of soil physical structure and biological functionality in mining spoil affected by soil erosion in a mediterranean-continental enviornment. *Geoderma*, **149**, 249–256.

Morgan, R. and Quinton, J. (2001). *Landscape Erosion and Evolution Modelling*, Erosion Modeling. Kluwer Academic/Plenum Publishers, New York.

Morgan, R., Quinton, J., Smith, R., Govers, G., Poesen, J., Auerswald, K. and CHISCI, G. (1998). The european soil erosion model (eurosem): A dynamic approach for predicting sediment transport from fields and small catchments. *Earth Surface Processes and Landforms*, **23**, 527–544.

Morris, E. and Woolhiser, D. (1980). Unsteady one-dimensional flow over a plane: Partial equilibrium and recession hydrographs. *Water Resources Research*, **16**, 355–360.

Nearing, M., Foster, G., Lande, L. and Finkner, S. (1989). A process-based soil erosion model for usda-water erosion prediction project technology. *Transactions of the ASAE*, **32**, 1587–1593.

Nearing, M., Norton, L., Bulgakov, D., Larionov, G., West, L. and Dontsova, K. (1997). Hydraulics and erosion in eroding rills. *Water Resources Research*, **33**, 865–876.

Oldeman, L., Hakkeling, R. and Sombroek, W. (1991). World map of the status o fhuman-induced soil degradation. An explanatory note, ISRIC, Wageningen.

Parlange, J., Rose, C. and Sander, G. (1981). Kinematic flow approximation of runoff on a plane: an exact analytical solution. *Journal of Hydrology*, **52**, 171–176.

Philip, J. (1969). Theory of infiltration. *Advances in Hydroscience*, **5**.

Pierson, F. (2000). *Rangeland Desertification*, Erosion models: use and misuse on rangelands, 67–76. Kluwer Academic Publisher, Dordrecht.

Pimentel, D., Harvey, C., Resosudarmo, P., Sinclair, K., Kurz, D., McNair, M., Crist, S., Shpritz, L., Fitton, R., L.Saffouri and Blair, R. (1995). Environmental and economic costs of soil erosion and conservation benefits. *Science*, **267**, 1117–1123.

Polyakov, V. and Nearing, M. (2003). Sediment transport in rill flow under deposition and detachment conditions. *Catena*, **51**, 33–43.

Ponce, V., Li, R. and Simons, D.B. (1978). Applicability of kinematic and diffusion models. *J.Hydraul.Div.Amer.Soc.Civil Eng*, **104**, 353–360.

Proffitt, A., Rose, C. and Hairsine, P. (1991). Rainfall detachment and deposition: Experiments with low slopes and significant water depths. *Soil Science Society of America Journal*, **55**, 325–332.

Proffitt, A., Hairsine, P. and Rose, C. (1993). Modeling soil erosion by overland flow: Application over a range of hydraulic conditions. *American Society of Agricultural and Biological Engineers*, **36**, 1743–1753.

Rabalais, N., Turner, R., Sen Gupta, B., Boesch, D., Chapman, P. and Murrell, M. (2007). Characterization and long-term trends of hypoxia in the northern gulf of mexico: does the science support the action plan? *Estuaries and Coasts*, **30**, 753–772.

Renard, K., Laflen, J., Foster, G. and McCool, D. (1994). *The revised universal soil loss equation*, Soil Erosion Research Methods, 105–124. Soil and Water Conservation Society, Ankeny, Iowa, USA.

Rose, C. and Ghadiri, H. (1991). *Modelling the Fate of Chemicals in the Enviornment*, Transport and Enrichment of Soil-sorbed Chemicals, 90–101. Centre for Resource and Environmental Studies, Australian National University, Canberra.

Rose, C., Parlange, J., Sander, G., Campbell, S. and Barry, D. (1983). Kinematic flow approximation to runoff on a plane : An approximate analytic solution. *Journal of Hydrology*, **62**, 363–369.

Rose, C., Williams, J., Sander, G. and Barry, D. (1983a). A mathematical model of soil erosion and deposition processes: I. theory for a plane land element. *Soil Science Society of America Journal*, **47**, 991–995.

Rose, C., Williams, J., Sander, G. and Barry, D. (1983b). A mathematical model of soil erosion and deposition processes: Ii. application to data from an arid-zone catchment. *Soil Science Society of America Journal*, **47**, 996–1000.

Sadeghi, S., Mizuyama, T., Miyata, S., Gomi, T., Kosugi, K., Fukushima, T., Mizugaki, S. and Onda, Y. (2008). Determinant fac-

tors of sediment graphs and rating loops in a reforested watershed. *Journal of Hydrology*, **356**, 271–282.

Sander, G., Parlange, J., Hogarth, W., Rose, C. and Haverkamp, R. (1990). Kinematic flow approximation to runoff on a plane: Solution for infiltration rate exceeding rainfalll rate. *Journal of Hydrology*, **113**, 193–206.

Sander, G., Hairsine, P., Rose, C., Cassidy, D. and Parlange, J. (1996). Unsteady soil erosion model analytical solutions and comparison with experimental results. *Journal of Hydrology*, **178**, 351–367.

Sander, G., Hairsine, P., Beuselinck, L. and Govers, G. (2002). Steady state sediment transport through an area of net deposition multisize class solutions. *Water Resources Research*, **38**, 1–23.

Sander, G., Parlange, J., Barry, D. and Hogarth, W. (2007a). Limitation of the transport capacity approach in sediment transport modeling. *Water Resources Research*, **43**, 1–9.

Sander, G., Rose, C., Hogarth, W., Parlange, J. and Lisle, I. (2007b). *Encyclopedia of Life Support Systems*, Mathematical Soil Erosion Modelling. Oxford: EOLSS publisher (www.eolss.net).

Sander, G., Zheng, T. and Rose, C. (2007c). Update to "modeling water erosion due to overland flow using physical principles: 1. sheet flow ". *Water Resources Research*, **43**, 1–4.

Schijven, J. and Hassanizadeh, S. (2000). Removal of viruses by soil passage: overview of modeling, processes and parameters. *Critical Reviews in Environmental Science and Technology*, **30**, 49–127.

Seeger, M., Errea, M.P., Beguería, S., Arnáez, J., Martí, C. and García-Ruiz, J. (2004). Catchment soil moisture and rainfall characteristics as determinant factors for discharge/suspended sediment hysteretic loops in

a small headwater catchment in the spainish pyrenees. *Journal of Hydrology*, **288**, 299–311.

Sherman, B. (1976). Kinematic wave models for overland flow. *Quarterly of Applied Mathematics*, **36**.

Sherman, B. and Singh, V.P. (1976a). A distributed converging overland flow model 1. mathematical solutions. *Water Resources Research*, **12**, 889–896.

Sherman, B. and Singh, V.P. (1976b). A distributed converging overland flow model 2. effect of infiltration. *Water Resources Research*, **12**, 897–901.

Smith, H. and Dragovich, D. (2009). Interpretation of sediment delivery processes using suspended sediment-discharge hysteresis patterns from nested upland catchments, south-estern australia. *Hydrological Processes*, **23**, 2415–2426.

Smith, R. (1981). A kinematic model for surface mine sediment yield. *Transactions of the ASAE*, 1508–1514.

Smith, R., Goodrich, D. and Quinton, J. (1995a). Dynamic, disttibuted simulation of watershed erison the kineros2 and eurosem models. *Journal of Soil and Water COnservation*, **50**, 517–520.

Smith, R., Goodrich, D., Woolhiser, D. and Unkrich, C. (1995b). *Computer Models of Watershed Hyddrology*, KINEROS-a Kinematic Runoff and Erosion Model, 697–732. Water Resources Publications, Littleton,CO.

Toro, E. (2001). *Shock-Capturing Methods for Free-Surface Shallow Flows*. John Wiley & Sons, Ltd.

Viera, J. (1983). Conditions governing the use of approximations for the st venant equations for shallow surface water flow. *Journal of Hydrology*, **60**, 43–58.

White, S. (1970). Plane bed thresholds of fine grained sediments. *Nature*, **14**, 152–153.

Wilcock, P.R. (1993). Critical shear stress of natural sediments. *Journal of Hydraulic Engineering*, **119**, 491–505.

Wilcock, P.R. and Crowe, J.C. (2003). Surface-based transport model for mixed-size sediment. *Journal of Hydraulic Engineering*, **129**, 120–128.

Williams, G. (1989). Sediment concentration versus water discharge during single hydrologic events in rivers. *Journal of Hydrology*, **111**, 89–106.

Wishchmeier, W. (1976). Use and misuse of the university soil loss equation. *Journal of Soil and Water Conservation*, **31**, 5–9.

Wishmeier, W. and Smith, D. (1960). A universal soil-loss equation to guide conservation farm planning. *Trans. Int. Congr. Soil Sci.*, **7**, 418–425.

Woolhiser, D. and Liggett, J.A. (1967). Unsteady one-dimensional flow over a plane-the rising hydrograph. *Water Resources Research*, **3**.

Woolhiser, D., Smith, R. and Goodrich, D. (1990). *KINEROS, a Kinematic Runoff and Erosion Model. Documentation and User Manual*. USDA, Agricultural Research Service, ARS-77.

Young, R., Onstad, C., Bosch, D. and Anderson, W. (1989). A nonpoint-source pollution model for evaluating agriculture watersheds. *Journal of Soil and Water Conservation*, 168–173.

Yu, T., Meng, W., Ongley, E., Li, Z. and Chen, J. (2010). Long-term variations and causal factors in nitrogen and phosphorus transport in the yellow river, china. *Estuarine, Coastal and Shelf Science*, **86**, 345–351.

Zhao, L., Wei, H. and Feng, S. (2002). Annual cycle and budgets of nutrients in the bohai sea. *Environment Science*, **23**, 78–81, in Chinese.